The Thesis Committee for Kathryn Rose Loeffler
Certifies that this is the approved version of the following thesis:

Development of an Implantable System to Measure the Pressure-Volume Relationship in Ambulatory Rodent Hearts

APPROVED BY
SUPERVISING COMMITTEE:

Supervisor: _____
Jonathan W. Valvano

Co-Supervisor: _____
John A. Pearce

Development of an Implantable System to Measure the Pressure-Volume Relationship in Ambulatory Rodent Hearts

by

Kathryn Rose Loeffler, B.S.Biomed.E.

Thesis

Presented to the Faculty of the Graduate School of

The University of Texas at Austin

in Partial Fulfillment

of the Requirements

for the Degree of

Master of Science in Engineering

The University of Texas at Austin

December 2012

Acknowledgements

Entering college at 18 I would never have thought I'd leave with a degree in electrical engineering. Circuits and programming seemed inaccessible, but getting an LED to blink from scratch for EE319K gave me an empowering glimpse into new possibilities. Thanks go to *Dr. Jon Valvano* for his attentive and sincere teaching style. He has reached many with his enthusiasm for cool gadgets, and I'm proud to be an engineer well versed in his unique style of "cowboy electronics".

Dr. John Pearce encouraged me to pursue biomedical electronics, and was a role model for good engineering practices.

Dr. Marc Feldman brought lots of positive energy to the group, he helped to move this and other projects forward with his organizational skills and professional connections. I would like to thank Dr. Feldman's team in San Antonio, animal surgeon *Danny Escobedo* and veterinarian *Patricia Escobar*, for their time and expertise during animal experiments.

I would also like to thank my colleagues:

Lev Shuhatovitch for letting me follow him around the lab as a new graduate student. Lev helped me learn to design and build PCBs and debug hardware. Whenever I'm particularly satisfied to be using the right tool for the job, I think of Lev.

Erik Larson for being a constant source of knowledge. Erik is a patient and persistent problem solver. When I ran up against frustrating problems, Erik always had new alternatives to try. And thanks to Erik and *Natalia Corona* for being good friends, encouraging Austin adventures, and feeding me weeknight dinners.

Bryan Brumm for taking over experiments during the summer months. Bryan is one of the most responsible undergraduate students I have worked with in the lab.

Robin Tsang for his enthusiasm and positive attitude. As an intern at Cirrus Logic, Robin taught me about real-world integrated circuits. Robin has a sharp mind for business and inspires me to think about the big picture.

Lastly, I would like to thank my support system:

Jean Liew for being a good listener and a great storyteller.

To *Michael Holland*, my best friend. Thanks for keeping me grounded with your earnestness and humor.

And finally, my parents *John* and *Jennifer Loeffler*.

Mom, thanks for always being only a phone call away. Mom taught me to be a lighthearted perfectionist, the kind of person who likes their peanut butter spread evenly, corner to corner. Always organized, she saved and planned so that I could go to college without debt. She is endlessly loving and always supportive. Thanks for letting me make "Katy bombs" in the middle of the living room floor.

One of Dad's favorite sayings is "if you aren't messing up, you aren't doing anything". Sometimes he measures twice to cut once, sometimes he just lops it off. Dad, because of you I was destined to be an engineer. Your greenhouses, your disk drive parts, the "junk pile" full of scrap wood and PVC pipe and whatnot, growing up our house was ripe with raw material for creation. Thanks for encouraging me to try things and helping to make my projects successful.

And thanks to both my parents for always having my best interest in mind.

Abstract

Development of an Implantable System to Measure the Pressure-Volume Relationship in Ambulatory Rodent Hearts

Kathryn Rose Loeffler, M.S.E.

The University of Texas at Austin, 2012

Supervisor: Jonathan W. Valvano

Co-Supervisor: John A. Pearce

The design, fabrication, and *in-vivo* testing of an implantable device to measure the pressure-volume (PV) relationship in the hearts of conscious, untethered rats is presented. Volume is measured using a tetrapolar catheter positioned in the left-ventricle which emits a 20kHz current field across the LV blood pool and parallel heart tissue and measures the resulting voltage. The admittance method is used to instantaneously remove the contribution of the parallel heart muscle and Wei's non-linear blood conductance-to-volume equation is used to calculate volume. Pressure is measured with a strain gauge sensor at the tip of the catheter. The implant was designed to be small, light, and low-power. An average implant occupies 5 cm^3, weighs 8g, and on a single charge collects data for 2 months taking 43 samples per day. Collected data is transmitted wirelessly via RF to a base station where it is recorded. The functionality of the implant and measurement system was verified in six rat experiments. In all experiments, ambulatory PV loops were measured on implantation day. Viable pressure data was recorded for 11 days in one rat; in another rat viable admittance data was collected for 10 days. Changing catheter position and non-constant blood resistivity are considered as sources of error in the volume measurement. Pressure drift due to changing atmospheric pressure is considered as a source of error in the pressure measurement. Lastly, alternative uses for the implant and directions for future improvement are considered.

Table of Contents

List of Tables x

List of Figures xi

Chapter 1: Introduction 1

1.1 Motivation 1

1.2 Similar Devices 2

1.3 Design Objectives 3

1.4 Admittance Method 5

Chapter 2. Implementation 9

2.1 System 9

2.2 Implant Hardware 9

2.2.1 Admittance Block 11

2.2.2 Pressure Block 13

2.2.3 RF Block 16

2.2.4 Power Management Block 18

2.3 Implant Software 18

2.3.1 Main Functions 18

2.3.2 Data Packet Format 20

2.4 Power Consumption and Implant Lifetime 21

2.5 User Interface 25

2.5.1. User interface hardware: Access Point 25

2.5.2. User interface software: LabVIEW 25

Chapter 3: Implant Manufacturing 29

3.1 Attaching the Catheter 29

3.2 Battery Considerations 31

3.3 Sealing the Circuit 32

3.4 Bench Testing and Calibration 33

3.4.1 Test Loads Before Catheter Attachment 33

3.4.2 Test Loads After Catheter Attachment 33
3.5 Evolution of the Implant 35
3.5.1 Implant Version 1 35
3.5.2 Implant Version 2 35
3.5.3 Implant Version 3 36
Chapter 4: Volume Calibration 38
4.1. Overview 38
4.2 Instrument Calibration 39
4.3 Probe Calibration 42
4.3.1 Limitations of the Saline Calibration Method 45
4.4 Sigma-Epsilon Ratio Optimization 48
Chapter 5: In-vivo Experiments 53
5.1 Implantation Procedure Summary 53
5.2 Implant Timelines 54
5.2.1 Rat 3, Implant 0 55
5.2.2 Rat 4, Implant S2 56
5.2.3 Rat 5, Implant S4 56
5.2.4 Rat 6, Implant S5 57
5.2.5 Rat 7, Implant S1 57
5.2.6 Rat 8, Implant S8 58
5.2.7 Failure Analysis Summary 58
5.2.8 Animal Health 58
5.3 Volume Over Time 59
5.3.1 Changes in Blood Resistivity Over Time 62
5.3.2 Catheter Positioning Error 62
5.3.3 Admittance Drift Due to Biological Wear 66
5.4 Pressure Over Time 66
Chapter 6: Conclusion 69
6.1 Implant Performance 69

6.2 Future Directions 70

Appendix A: Implant Assembly Procedure 71

Appendix B: Rat 3 Data Set Summary 79

Appendix C: Rat 4 Data Set Summary 80

Appendix D: Rat 5 Data Set Summary 83

Appendix E. Rat 6 Data Set Summary 87

Appendix F. Rat 7 Data Set Summary 90

References 93

List of Tables

Table 1: Market Analysis of Competitive Devices 3

Table 2: Design Goals 4

Table 3: LabVIEW Interface Variables 28

Table 4: Numerically Determined Best-fit Sigma-Epsilon Ratios 51

Table 5: Heart Volume Over Time From 2D Echo 59

Table 6: Calibration Constants, Rat 3 79

Table 7: Calibration Constants, Rat 4 80

Table 8: Calibration Constants, Rat 5 83

Table 9: Calibration Constants, Rat 6 87

Table 10: Calibration Constants, Rat 7 90

List of Figures

Figure 1. System Concept 4
Figure 2: Scisense PV Catheter (right), and Catheter Positioning (left). 5
Figure 3: System Block Diagram 9
Figure 4. Implant Hardware Block Diagram 10
Figure 5: Implant Circuit 10
Figure 6: Admittance Block Linearity 12
Figure 7: Admittance Block Noise 12
Figure 8: Pressure Transducer 13
Figure 9: Pressure Measurement Circuitry 14
Figure 10: Pressure Channel Output for 0mmHg Relative Pressure Input 16
Figure 11: RSSI Tests Under Different Conditions 17
Figure 12: Implant Software Flow Chart 19
Figure 13: Data Packet Formats 20
Figure 14: Current Consumption Profile 22
Figure 15: Lifetime Estimation 24
Figure 16: Fullscreen LabVIEW Interface 26
Figure 17: LabVIEW Runtime Controls (left) and Calibration (right) Tabs. 27
Figure 18: Displacement of Catheter Along Long Axis 30
Figure 19: Supply Current Measurement Circuit 34
Figure 20: Version 1 Implant 35
Figure 21: Version 2 Implant 36
Figure 22: Version 3 Implant 37
Figure 23: Error Sources Requiring Calibration 38

Figure 24: Implant Calibration Flowchart 39
Figure 25: Uncorrected Resistor Sweep 40
Figure 26: Resistor Sweep After Constant Phase Angle Subtraction 41
Figure 27: Capacitor Sweep 42
Figure 28: Non-Ideal Catheter Model 43
Figure 29: Electrode Impedance Model 44
Figure 30: Saline Sweeps 45
Figure 31: Output of Peak Finding Algorithm. 49
Figure 32: Calibrated Volume After Sigma-Epsilon Ratio Search 50
Figure 33: PV Loops After Sigma-Epsilon Ratio Search Algorithm 51
Figure 34: Implant Timelines 54
Figure 35: PV Loops on Implantation Day 55
Figure 36: Blood (blue) and Muscle (red) Conductance Traces Over 10 Days 60
Figure 37: Volume Measured by Ultrasound and Experimental Implant 61
Figure 38: Catheter Position and PV Loops During Implantation for Rat 4 61
Figure 39: Squash Cuvette Catheter Position Experiment 63
Figure 40: Volume vs. Catheter Position 64
Figure 41: Volume on Days 9 and 10, Rat 4 65
Figure 42: Catheter After 5 Months in the Heart 66
Figure 43: Location of End Diastolic Pressure Points (blue) 68
Figure 44: End Diastolic Pressure Drift 68
Figure 45: Catheter on Bending Mold 73
Figure 46: Exposing Catheter Wires 74
Figure 47: Formed Catheter With 7 Wires Exposed 75
Figure 48: Mounting the Catheter to the Board 75

Figure 49: Catheter Wires Soldered to the Circuit....76
Figure 50: Potting Compound Applied and Battery Attached....76
Figure 51: Battery Mounted Against the Circuit Using Potting Compound....77
Figure 52: Circuit Covered in Electrical Tape....77
Figure 53: Completed Implant....78
Figure 54: Volume Calibration, Rat 3....79
Figure 55: Volume Calibration, Rat 4....80
Figure 56: Pressure Data, Rat 4....81
Figure 57: Admittance Data, Rat 3....82
Figure 58: Volume Calibration, Rat 5....83
Figure 59: Pressure Data, Rat 5....84
Figure 60: Volume Data, Rat 5....85
Figure 61: PV Data, Rat 5....86
Figure 62: Volume Calibration, Rat 6....87
Figure 63: Pressure Data, Rat 6....88
Figure 64: Volume Data, Rat 6....89
Figure 65: Volume Calibration, Rat 7....90
Figure 66: Pressure Data, Rat 7....91
Figure 67: Volume Data, Rat 7....92
Figure 68: PV Data, Rat 7....92

Chapter 1: Introduction

1.1 MOTIVATION

With advances in the development of transgenic rodents, murine models of cardiac pathology have become available for pharmaceutical studies [1]. To accurately assess the efficacy of medical interventions on these animals, a device is needed that can report measures of cardiac health in ambulatory rodents long term. The goal of this work is to develop such a device.

The pressure-volume relationship is an important indicator of cardiac health. Pressure is relatively easy to measure with cannulation, or more recently, solid state pressure sensors. Obtaining an accurate measure of volume, however, can be challenging. The gold standard in volume measurement is MRI [2], though ultrasound can be used as well. These techniques are expensive and require the animal to be anesthetized. An alternative method is to derive the volume of the left ventricle (LV) from the varying electrical properties of the heart. In 1981, the first cardiac catheter was developed to measure the impedance of the blood pool in the LV [3]. This, and subsequent cardiac catheters carry electrodes that emit an electric field and measure the response of the blood pool. Sagawa et al. were the first to show that the conductance measured from an LV catheter was proportional to LV volume in 1985 [4]. With new, smaller catheter technology, the first PV loops in mice were measured in 1998 [5]. Since then, research has focused on finding the most accurate calibration scheme for converting blood conductance to volume [6, 7, 8].

But there is still work to be done if PV data is to be measured from ambulatory rats in chronic studies. Calibration methods must consider how variables such as catheter position, blood conductivity, and electrode impedance change over time and measurement devices should be small, low-power, and physically robust. In the literature, two studies (Uemura, 2004 and Raghavan, 2011) have shown the feasibility of telemetric PV rat systems for chronic studies. The Uemura device was fully implantable, consisted of a 14g/11cm^3 processor transmitter, a 12g/10 cm^3 battery, lasted 8 days, and produced consistent data in rats over a 6-day span [9]. The Raghavan device was a 27g backpack system interfaced to an implanted catheter that lasted 24 hours and produced telemetric PV data every 2 minutes for 6 rats [10]. This work is an extension of Raghavan's work and the second iteration of the Shuhatovitch device [11], a fully implantable PV measurement system that improves implant size to 8g/5 cm^3 and lifetime to over 2 months.

1.2 SIMILAR DEVICES

There are several companies that produce implants to measure biological signals in animals. Implant manufacturers and the biological parameters they are capable of measuring are listed in Table 1. Note that the experimental UT Austin implant is the only implant capable of measuring volume.

Table 1: Market Analysis of Competitive Devices

Parameter	Millar	Transonic	Data Sciences	UT Austin
				
Size	5-6 cm^3 est.	25 cm^3	1.4 cm^3	5 cm^3
Battery Life	Inductive Power	2-6 weeks continuous, 6mo. Low pwr.	1 month	2 month at 43 collections/day
Measurements Available	Pressure, SNA, ECG, EMG, EEG, temperature	Flow, blood pressure, ECG, temperature	Pressure, ECG, EEG, EOG, EMG, temperature, "activity"	Pressure, Volume, Cardiac Output
Pressure Range	-20 to 300 mmHg	-50 to 300 mmHg	-20 to 300 mmHg	-40 to 400 mmHg
Pressure Resolution				0.4 mmHg
Pressure Accuracy			+/- 3 mmHg	
Pressure Drift			<2 mmHg/mo.	± 3 mmHg
Sampling Frequency	2 kHz, or 8kHz	120 Hz, or 60 Hz	Biopotential bandwidth: 200 Hz	1 kHz
Communication Protocol	Inductive	RF	RF	RF

1.3 Design Objectives

The goal for this project is to develop an implant capable of measuring PV relationships in ambulatory rats. Objectives for the design are listed in Table 2. In this application, size and weight are of utmost concern. The target weight of the design was set to 25 g, which is 10% the weight of an adult rat. The target volume was set at less

than 5 cm^3, to be reasonably competitive with similar commercial devices and improve upon previous experimental devices.

Table 2: Design Goals

1	< 5 cm^3 total volume
2	< 25 g weight
3	< 1 mmHg pressure resolution
4	> 350 mmHg pressure range
5	200-2000 Ω impedance range
6	Reasonably robust interface to the delicate catheter
7	Waterproof and biocompatible
8	Transmit data wirelessly
9	2 month battery life sampling at least once per day

Consulting with veterinarians and animal surgeons, a system concept was developed in which the implant would be placed under the skin between the rat's shoulder blades. The catheter would then wrap around the rats shoulder, beneath the skin, and be inserted into the LV through the carotid artery. The rat would be placed near a base station where PV data would be periodically collected and displayed. This system concept is shown in Figure 1.

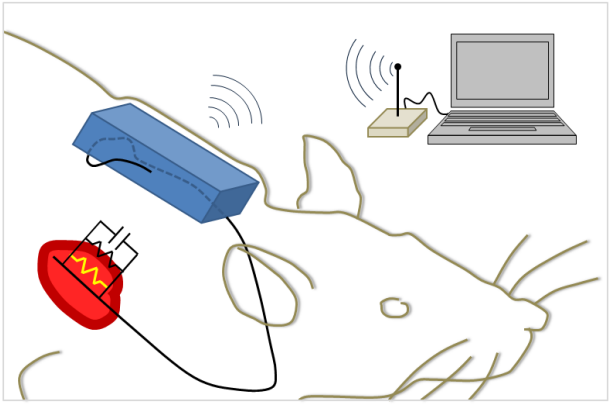

Figure 1. System Concept

1.4 Admittance Method

The implant interfaces to a 1.9F Scisense Pebax catheter (Figure 2) that contains four electrodes and a pressure sensor. A 4-electrode configuration is generally considered to be superior to a 2-electrode configuration for plethysmographic measurements because separation of the current production and voltage measurement electrodes leads to a more uniform electric field in the voltage sensing region. In a 2-electrode system, the current density is higher near the electrodes, causing the tissue impedance near the electrodes to be weighted more heavily [12].

In this application, a 20kHz current field is emitted from the outer 2 electrodes, and a potential difference is measured at the inner electrodes. The voltage measured from the inner electrodes differs in magnitude and phase from the excitation signal, and thus provides a value for complex admittance.

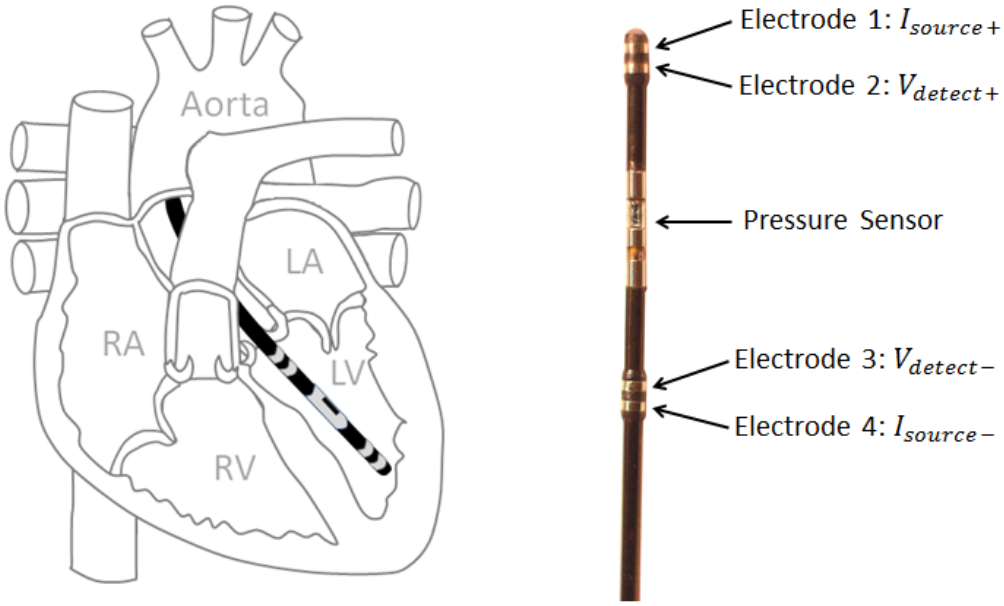

Figure 2: Scisense PV Catheter (right), and Catheter Positioning (left).

This complex admittance value represents a measurement of the bulk properties of the catheter and the tissue surrounding the catheter, namely, the blood in the left ventricle (LV) and the surrounding heart muscle. Since the volume of the LV is proportional to the conductance of the blood alone, the admittance of the muscle is unwanted signal and must be removed. The bulk admittance signal measured by the circuit can be represented as the sum of the blood conductance (G_b), muscle conductance (G_m), muscle susceptance ($B_m = j\omega C_m$), and catheter susceptance ($B_{probe} = j\omega C_{probe}$) as given in (1 **)**.

$$Y_{meas} = G_b + G_m + j\omega C_m + j\omega C_{probe} \quad (1)$$

C_{probe} is the parasitic capacitance of the catheter due to the length of the catheter and the close proximity of the four electrode wires within the catheter lumen. This value is dependent on load conductance and is estimated from a one-time saline calibration. After calibrating the bulk data for C_{probe}, the remaining imaginary component in Y_{meas} should be solely related to C_m. Note, however, that representing the lumped ImY error of the probe as a single capacitor is based on an assumed equivalent circuit for the catheter that may not include all important effects of the physical probe. Calibration for probe effects is explained in more detail in Chapter 4.

From general principles, conductance, G with units [S] and capacitance, C, with units [F] in a homogeneous medium can be written as in (2 **)** and (3 **)**, respectively.

$$G = \frac{I}{V} = \sigma \frac{\iint E \cdot dA}{-\int E \cdot dl} = \sigma F \quad (2)$$

$$C = \frac{Q}{V} = \varepsilon \frac{\iint E \cdot dA}{-\int E \cdot dl} = \varepsilon F \quad (3)$$

Here, F represents the geometric form factor common to both equations. With this, it is clear that conductance and capacitance in the same geometry are related as in (4 **)**, where σ is conductivity [S/m] and ε is permittivity [F/m]. From this, the conductance of the muscle can be written as (5 **)**.

$$\frac{G}{\sigma} = \frac{C}{\varepsilon} \quad (4)$$

$$G_m = \frac{\sigma}{\varepsilon} C_m \quad (5)$$

It follows that:

$$G_b = Re\{Y_{meas}\} - \frac{\sigma}{\varepsilon} C_m \quad (6)$$

where the sigma-epsilon ratio *(σ/ε)* represents the ratio of the conductance of the muscle to the permittivity of the muscle and allows the removal of the muscle conductance from the bulk measured conductance to derive blood conductance.

In the 1980's, Baan *et al.* developed a linear equation to convert blood conductance, G_b [S] to volume, V [cm^3], according to equation (7 **)**.

$$V = \frac{1}{\alpha} \rho L^2 G_b \quad (7)$$

where ρ is blood resistivity [Ω-cm], L [cm] is the distance between the measuring electrodes, and α is an empirically-derived field geometry correction factor. This equation assumes a uniform electric field in the measurement volume, an unrealistic assumption given the non-uniform geometry of the heart. In 2005, Wei *et al.* extended

this equation to include a non-linear correction factor, γ, that forces the calculated stroke volume (SV) to equal the stroke volume measured during calibration [6] (8 **)**.

$$V = \frac{1}{1 - G_b/\gamma}\rho L^2 G_b \qquad (8)$$

Gamma is specified as the larger positive solution to the quadratic equation dependent on stroke volume, SV [cm^3] and blood conductance at end systole ($G_{b\text{-}ES}$ [S]) and end diastole ($G_{b\text{-}ED}$ [S]) as described in (9 **)**.

$$\gamma = \frac{-b \pm \sqrt{b^2 - 4ac}}{2a} \qquad \begin{aligned} a &= SV - \rho L^2 (G_{b-ED} - G_{b-ES}) \\ b &= -SV(G_{b-ED} - G_{b-ES}) \\ c &= SV(G_{b-ED})(G_{b-ES}) \end{aligned} \qquad (9)$$

Chapter 2. Implementation

2.1 System

Figure 3 is a diagram of the measurement system. The implant periodically collects PV data and transmits it wirelessly to a base station, which consists of the access point, computer, and display. Once PV data is received at the access point, it is relayed to the computer where it is recorded and displayed via a LabVIEW interface. Communication can occur in the reverse direction as well. Commands and settings indicated by the user are sent over USB to the access point where they are subsequently transmitted to the implant by RF during a communication period.

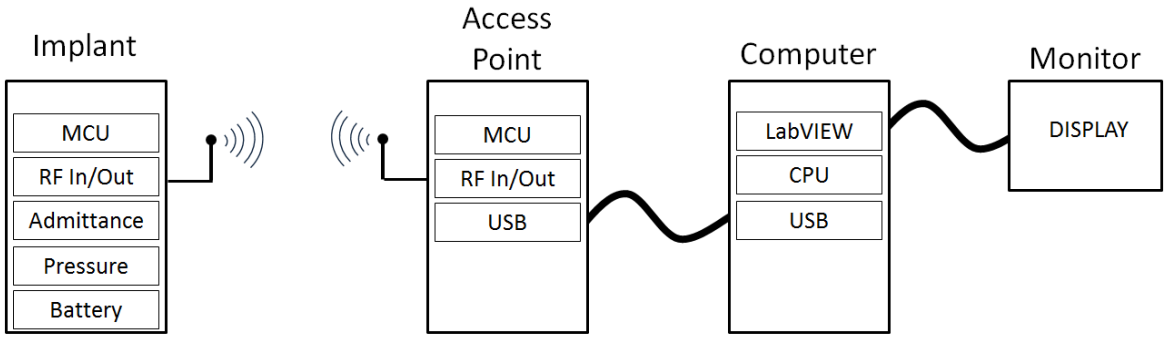

Figure 3: System Block Diagram

2.2 Implant Hardware

The implant contains four main hardware blocks: admittance measurement, pressure measurement, RF communication, and power management as shown in Figure 4. A photograph of the implant circuit is provided in Figure 5.

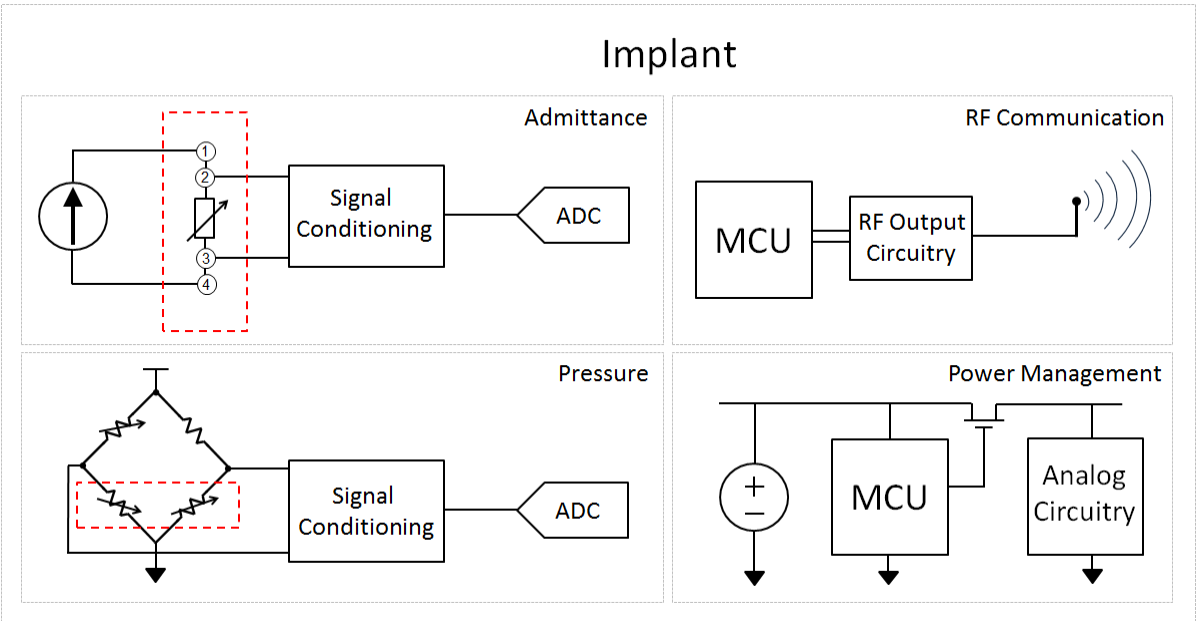

Figure 4. Implant Hardware Block Diagram

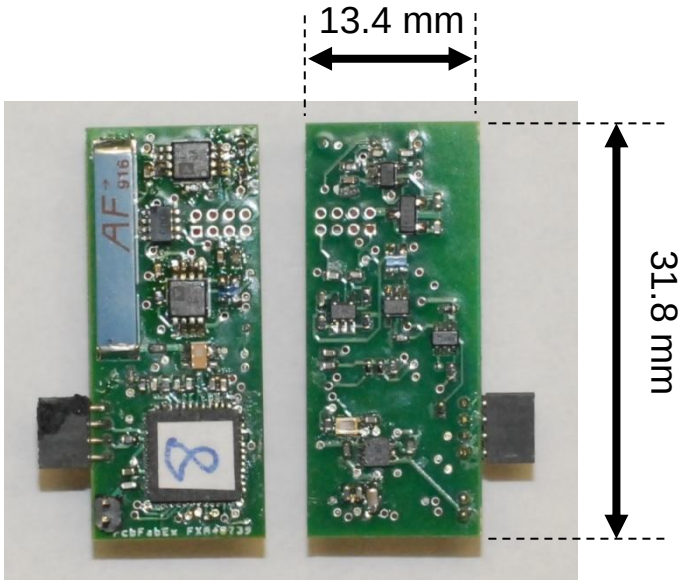

Figure 5: Implant Circuit

2.2.1 Admittance Block

The admittance and pressure measurement blocks make up the bulk of the analog circuitry. To measure admittance, a load-independent, active current source is used to supply 30 μA, 20 kHz sinusoidal excitation across electrodes 1 and 4 of the catheter. With a constant current source, the voltage across the bulk admittance of the heart around the catheter varies according to Ohm's law (Y = I/V). This differential voltage is measured across electrodes 2 and 3, amplified and filtered, and sampled by at 10-bit resolution by the microcontroller for processing. Experimentation has shown that the typical resistance of the blood pool in a rat LV is around 800 to1200 Ω. Figure 6 describes the linearity and Figure 7 the noise characteristics of the admittance channel. Notice that the largest real Z residual for a linear fit is 3.2 Ω, and the largest imaginary Z residual is 0.4 Ω. Considering the measurement range of 200 to 2000Ω, the admittance channel is linear within 0.2%.

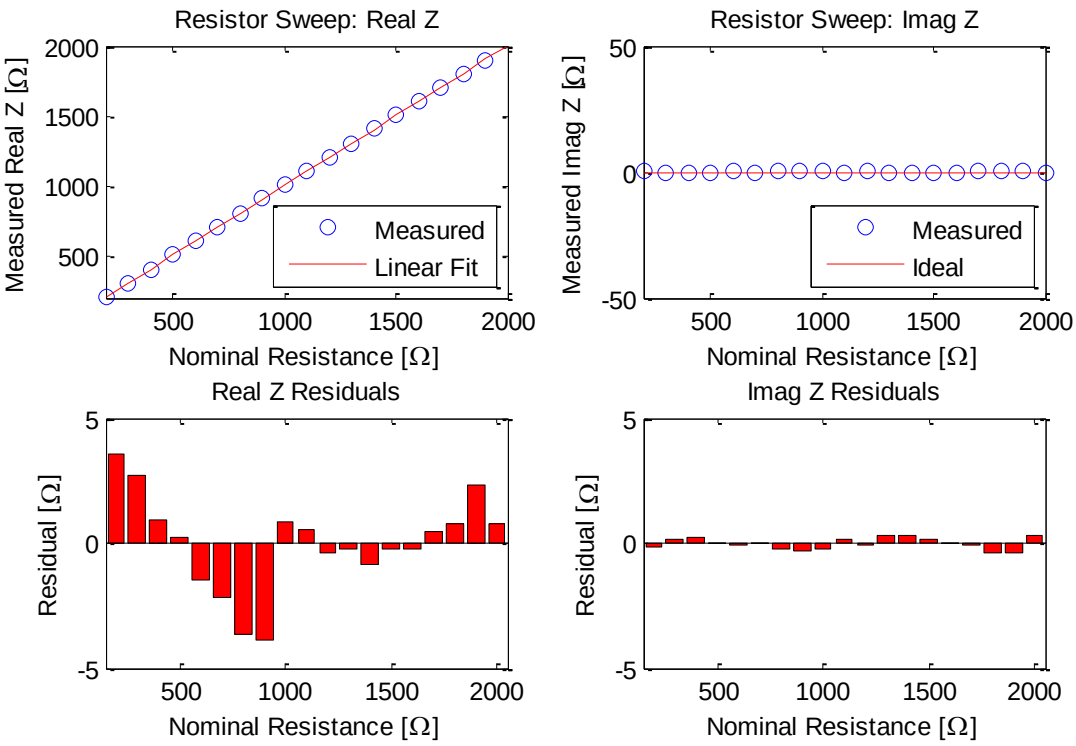

Figure 6: Admittance Block Linearity

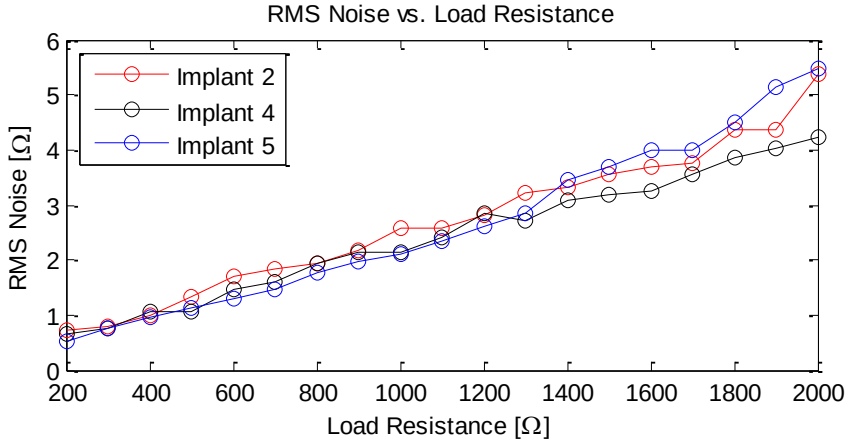

Figure 7: Admittance Block Noise

2.2.2 Pressure Block

A schematic of the Scisense pressure transducer is given in Figure 8. Two solid state resistors are positioned orthogonally to one another on a cantilever beam that is placed beneath an opening in the catheter referred to as the pressure window. A flexible seal isolates the lumen of the catheter from the blood pool such that the deflection of the cantilever beam is relative to the pressure difference between the blood pool and the catheter lumen.

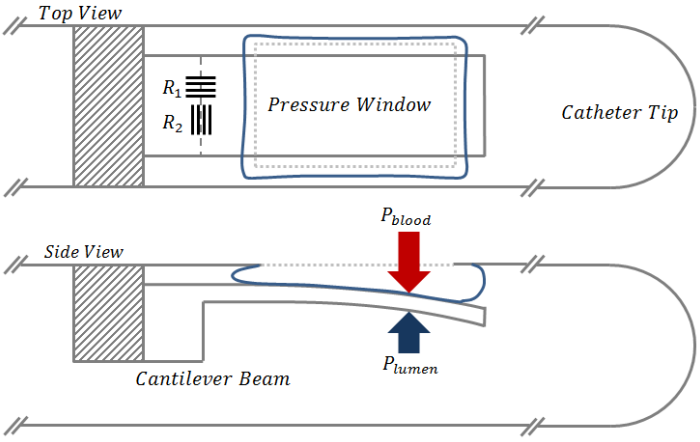

Figure 8: Pressure Transducer

As the catheter deflects downward, the stripes of R_1 become longer and the stripes of R_2 become wider, thereby increasing R_1 and decreasing R_2 according to (10 **)**.

$$R = \frac{\rho L}{A} \qquad (10)$$

Where ρ is the resistivity of the stripe [Ω-m], L the length [m], and A the cross-sectional area [m^2]. To measure pressure, R_1 and R_2 from the catheter are used as the bottom elements in a Wheatstone bridge circuit. The bridge contains a digital balancing

potentiometer controllable through the LabVIEW interface. The differential output of the Wheatstone bridge is amplified and filtered, then sampled by a 10-bit ADC on the microcontroller.

Let us derive the sensitivity of the pressure transducer and measurement circuitry. Figure 9 below shows the Wheatstone bridge circuit.

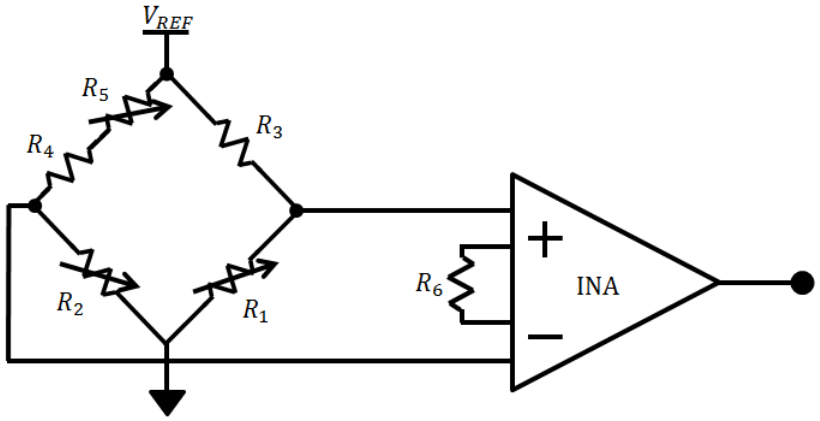

Figure 9: Pressure Measurement Circuitry

The output voltage of the INA is,

$$V_{out} = V_{REF} Gain \left(\frac{R_2}{R_2 + R_4 + R_5} - \frac{R_1}{R_1 + R_3} \right) \quad (11)$$

Here R_5 is the digital balancing potentiometer. Assuming $R_1 = R_2 = R_B$ and $R_4 + R_5 = R_3 = R_T$, we can represent a small and equal but opposite change in each R_B as ΔR and equation (11 **)** reduces to equation (12 **)**.

$$V_{out} = V_{REF} Gain \left(\frac{2R_T \Delta R}{(R_B + R_T)^2 - \Delta R^2} \right) \quad (12)$$

The denominator is simplified by assuming that $(R_B + R_T)^2 >> \Delta R^2$.

$$V_{out} \approx V_{REF} Gain \left(\frac{2R_T \Delta R}{(R_B + R_T)^2} \right) \quad since \quad (R_B + R_T)^2 \gg \Delta R^2 \tag{13}$$

Sensitivity is then defined by the derivative of V_{out} with respect to ΔR.

$$\frac{dV_{out}}{d\Delta R} \approx V_{REF} Gain \left(\frac{2R_T}{(R_B + R_T)^2} \right) \tag{14}$$

With this transfer function and calibration results, the sensitivity of the Scisense pressure transducer is calculated. Using a Scisense pressure measurement box as a standard, the output of the pressure circuit on the implant was observed to traverse 232 ADC codes per 100 mmHg. The 10-bit ADC uses a reference of 2.5 V, and thus has a resolution of 2.5V/1024 codes. As calculated above, the sensitivity of the pressure circuit to ΔR is 0.198 V/Ω. Thus, the sensitivity of the pressure transducer, in terms of Ω/mmHg, is:

$$\left(\frac{232\ codes}{100\ mmHg} \right) \left(\frac{2.5\ V}{1024\ codes} \right) \left(\frac{1\ \Omega}{0.198\ V} \right) = \frac{28.6\ m\Omega}{1\ mmHg} \tag{15}$$

The same data indicates that the ADC-limited resolution of the pressure channel is 100mmHg/232codes = 0.43mmHg/code. Given that this is a 10-bit ADC, this resolution translates to a total measurement range of 440 mmHg. Figure 10 shows the output of the pressure channel for a 0 mmHg atmosphere-relative pressure. The RMS value of the noise is 0.306 mmHg, which is less than the ADC-limited resolution. This indicates that > 68% (±1σ) of the pressure measurements fall within 1 ADC code of the mean, a conclusion that is clearly visible in the figure.

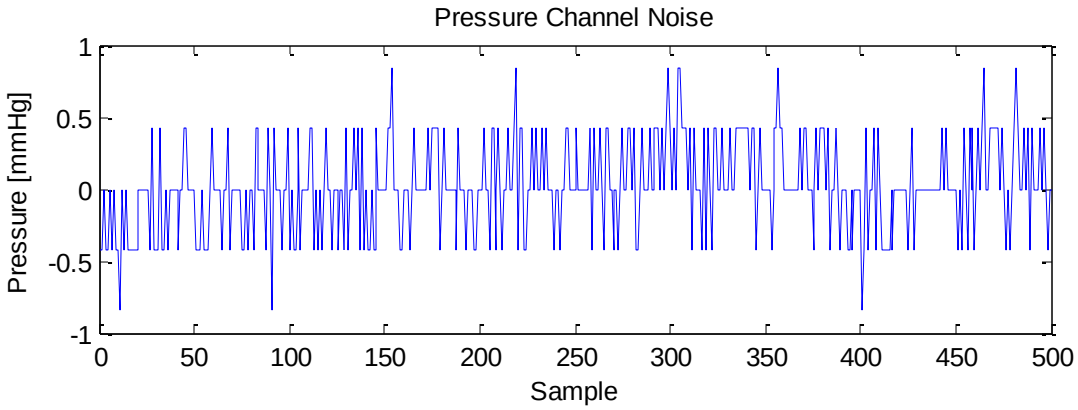

Figure 10: Pressure Channel Output for 0mmHg Relative Pressure Input

2.2.3 RF Block

The RF communication functionality of the implant is implemented mainly by the microcontroller. With the correct arrangement of accessory components, the MCU outputs a 915 MHz, differential RF signal. A balun is used to convert this differential signal to a single-ended signal that is capacitively coupled to an antenna.

The MCU has a software-tunable output power level and variable output data rate. Fast data rates reduce transmission time, which reduces the communication range and the total power of each transmission. For this implementation, it was found that setting the RF output level to 0dbm (maximum) and the baud rate to a moderate 174 kBaud provided a typical communication range of 15 feet. During implantation and data collection the circuit is within ~10 feet of the base station, so the output power level is sufficient without being wasteful.

The communication range is affected by the orientation of the transmitter antenna in relation to the receiver, the material surrounding the transmitter, and the presence of barriers or conductive bodies in the communication channel. The received signal

strength indicator, or RSSI, is measured in decibels by the access point. Figure 11 shows the RSSI from the implant to the access point under different conditions.

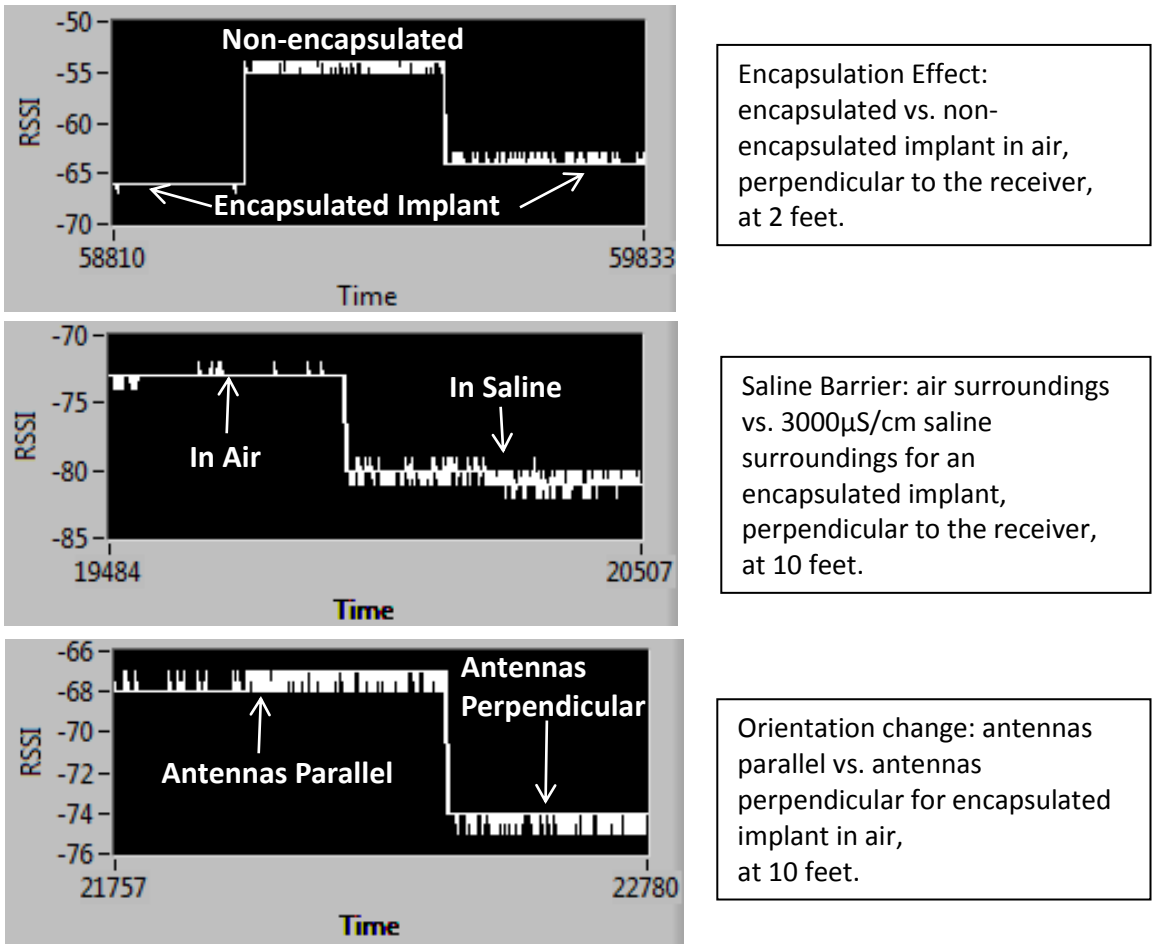

Figure 11: RSSI Tests Under Different Conditions

Encapsulating the circuit for implantation involves positioning a battery close to the antenna and applying layers of waterproofing. In the first panel of Figure 11, a ~10 dB drop in RSSI is observed for these modifications. To model the effects of implanting the circuit in a conductive body (the rat), an encapsulated implant was submerged by 2 mm in 200 mL of 3000µS/cm saline solution. The second plot in Figure 11 shows a 7 dB

drop in RSSI for this effect. In the standard system setup, the access point antenna is oriented perpendicular to the earth and the implant antenna parallel to the earth (flat on the rat's back). Changes in the implant position with movement of the rat may only improve the RSSI from the standard position as parallel antennas give the best RSSI as shown in the third plot in Figure 11.

2.2.4 Power Management Block

Low power consumption is implemented by two means: sleep functionality in the MCU and power gating of the analog circuitry. The MCU used in this design has several sleep modes with differing power consumption. For this application, the lowest power mode for which timing functionality was still available was chosen. This LPM is specified to reach ~2μA, quiescent current consumption, a number verified on the bench. To ensure low power consumption for the implant as a whole, a MCU-controlled MOSFET is used to disable power to the analog circuitry during sleep. Thus, only the essential sleep counter function in the MCU is enabled during sleep mode.

2.3 IMPLANT SOFTWARE

2.3.1 Main Functions

The implant software is responsible for timing data collection events, packetizing and transmitting PV data, receiving and interpreting access point (AP) commands, and managing sleep/wake cycles. The basic series of events executed by the implant is illustrated in Figure 12. The colored middle segment represents the chain of events that

constitute one data collection. That is, the circuit wakes up, enables the analog circuitry, collects a user-specified number of PV samples, packetizes and transmits the PV data via RF, then listens for new commands sent from the access point.

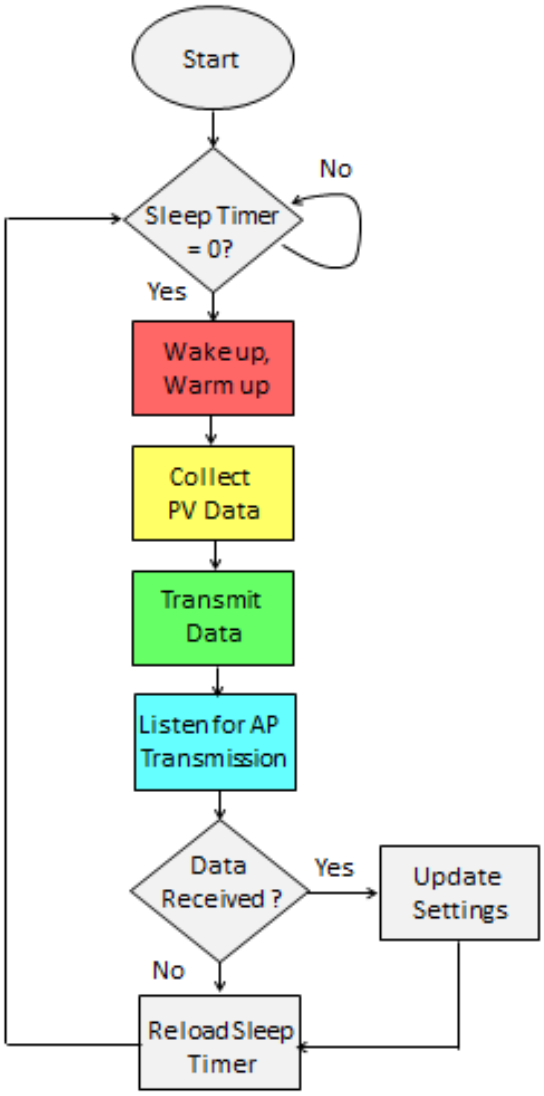

Figure 12: Implant Software Flow Chart

2.3.2 Data Packet Format

There are four main types of data packets that are used to communicate between LabVIEW and the implant. The first two packet types, the control frame and data frame, are sent from the implant to the access point. The second two packet types communicate settings and calibration constants from LabVIEW to the implant.

Each packet type has an ID as the first element. This ID dictates how the remainder of the packet should be interpreted (first nibble). The ID field also encodes the implant number (second nibble) so that LabVIEW can parse incoming data from multiple implants into the appropriate files.

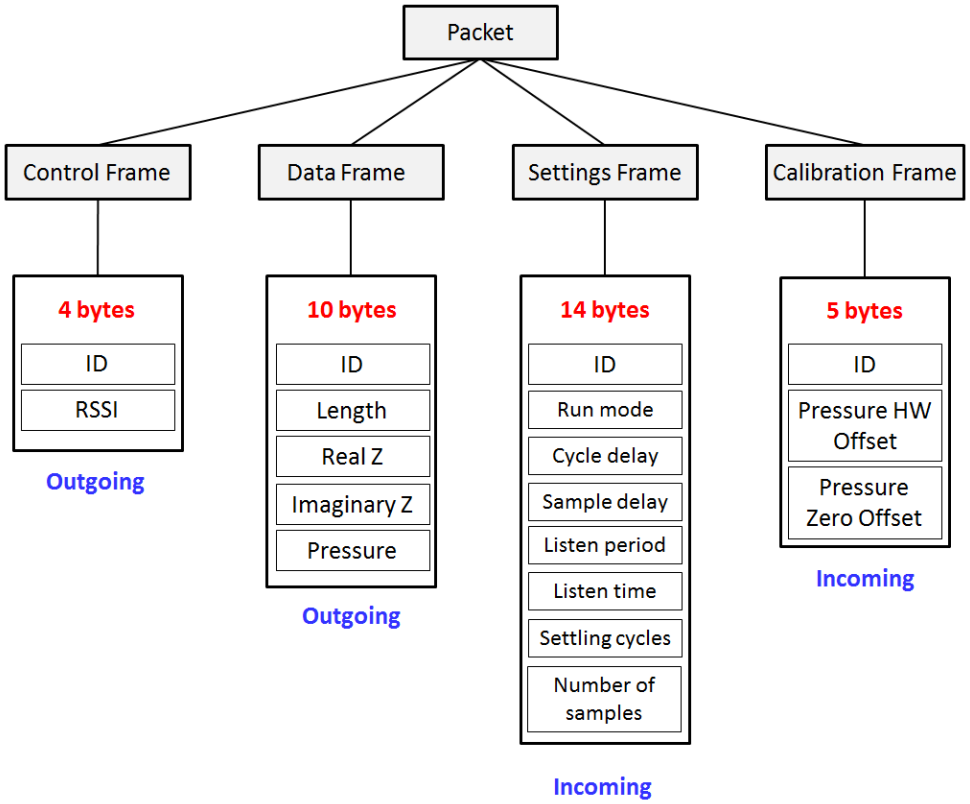

Figure 13: Data Packet Formats

2.4 Power Consumption and Implant Lifetime

Plotting the instantaneous current draw versus time for the implant during a collection period allows us to estimate the energy "cost" of each data epoch (Figure 14). In a typical data epoch, 384 samples are collected at a 1 kHz sampling rate to give 384 ms of data, about 1.5 – 2 cardiac cycles in the rat heart. From Figure 14 we can see that the listening period is the most costly segment. In bench testing it was observed that 4 seconds of listening were necessary to ensure proper data transmission, but this figure could possibly be improved if a more robust handshake protocol were implemented such that only the time required to establish whether or not the AP needed to send data would be required.

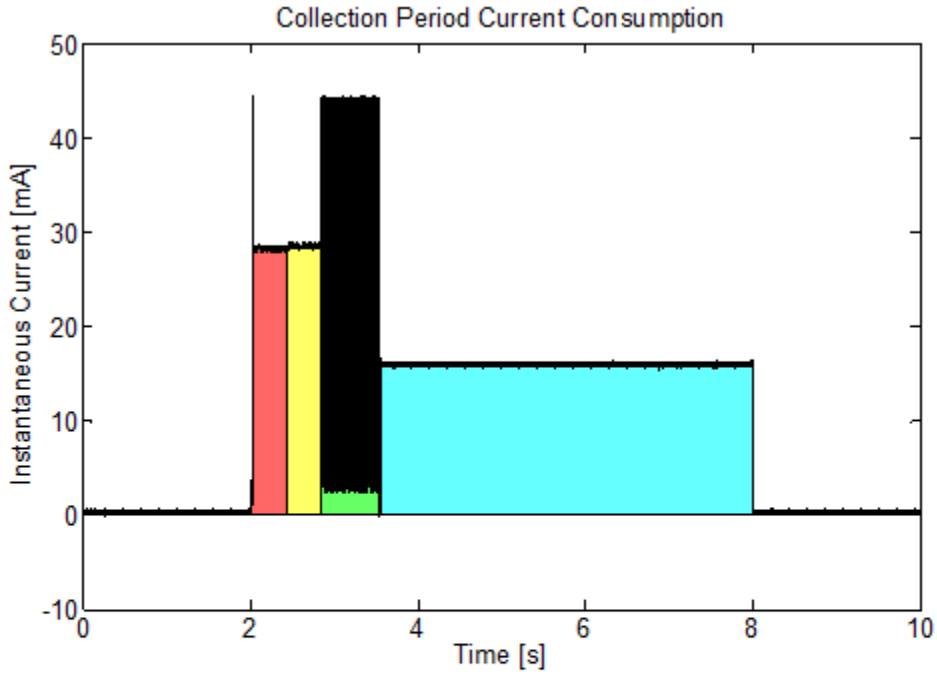

Segment		Mean Instantaneous Current	Energy Consumed
Wakeup / Warm-up		28 mA	3.3 µA-H
PV Measurement		28 mA	3.2 µA-H
RF Transmission		24 mA	4.7 µA-H
RF Listen		16 mA	19.6 µA-H
Total Collection Energy			30.8 µA-H

Figure 14: Current Consumption Profile

By measuring the sleep current of the implant and the energy used per epoch, one can estimate the lifetime of the implant according to the following formula (16 **)**.

$$E_{remaining} = E_{battery} - N \cdot t \cdot E_{collect} - 24 \cdot t \cdot I_{sleep} \qquad (16)$$

Here t is the time in days, N the number of collection periods per day, I_{sleep} the sleep current of the implant in mA, $E_{collect}$ the energy required for one measurement epoch, $E_{battery}$ the total energy in the charged battery, and $E_{remaining}$ is the energy left in

the battery after time *t*. All energy figures have units of mA-h. To calculate the lifetime, $E_{remaining}$ is set to zero and find (17 **)**.

$$t_{lifetime} = \frac{E_{battery}}{N \cdot E_{collect} + 24 \cdot I_{sleep}} \quad (17)$$

This formula assumes that I_{sleep} amount of current is drawn constantly (even during collection). This simplifies the formula and is a fair assumption given that $I_{collect} >> I_{sleep}$ and I_{sleep} is within the uncertainty of the $I_{collect}$ measurement method (explained in Section 3.4.2.

The sleep current of a typical implant is in the range 1-5 μA. Using a worst-case sleep current figure of 5 μA, a battery life of 150 mA-h, and a collection energy value of 30.8 μA-h as calculated above, the estimated lifetime of the implant as a function of sampling epoch frequency is shown in Figure 15 (green line).

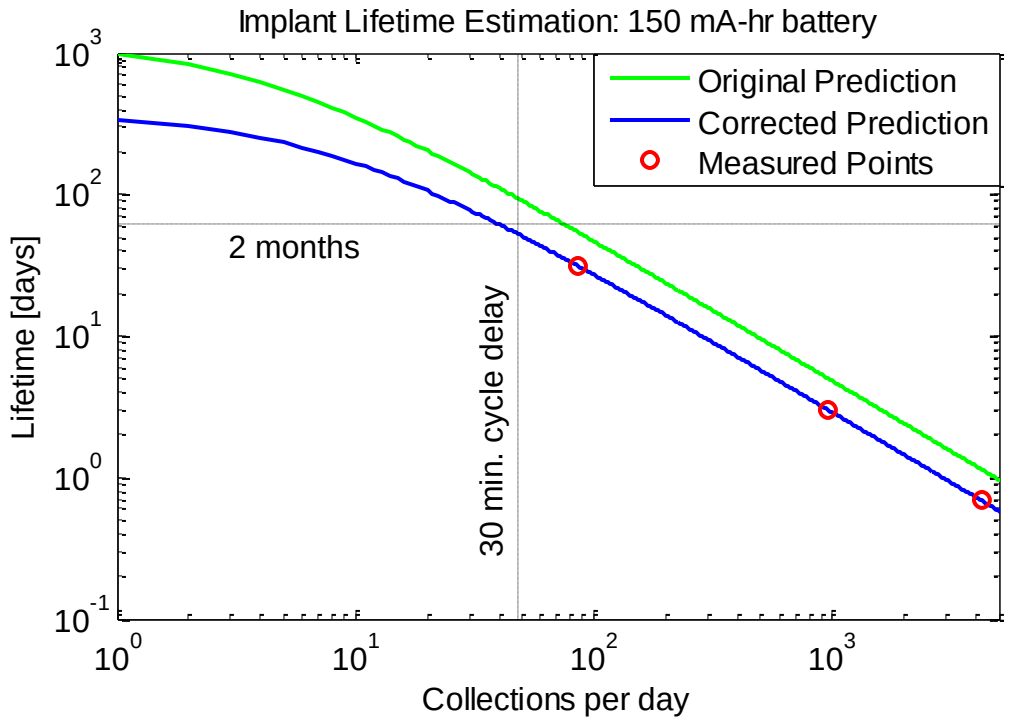

Figure 15: Lifetime Estimation

When real lifetime points were measured, actual implant lifetime was found to be less than originally predicted. This is a result of inefficiency in the battery, and underestimation of the sleep and measurement current. The three red points in Figure 15 indicate the results from bench testing trials. Using MATLAB, I_{sleep} and $E_{collect}$ from (16 **)** were adjusted to minimize the error between the predicted curve (blue) and the measured points. This process increased $E_{collect}$ by a factor of 1.5 from 30.8 µA-h to 46.0 µA-h. I_{sleep} was increased by 2.9 from 5 µA to 14.7 µA. Based on separate testing of the LiPo batteries, E_{bat} was decreased by 10% to 135 µA-h. Figure 15 is annotated with markers to indicate 2 months and 30 minute cycle delay. The evidence-based lifetime prediction suggests that the implant will last for 2 months collecting 43 samples/day. If data is collected once per day, the implant is projected to last 338 days on a single charge.

2.5 USER INTERFACE

2.5.1. User interface hardware: Access Point

The access point was implemented from a commercially available RF development board modified to communicate with LabVIEW through USB. The access point performs minimal processing on the data sent from the implant. Its purpose is mainly to intercept RF data and shuttle it to the computer via USB.

2.5.2. User interface software: LabVIEW

The LabVIEW interface serves two main functions, to store raw data in text files and to display incoming data in real time. This interface is organized as three sets of tabular objects. The largest tab set (left side of the screen) is used to display incoming data in different formats. The two smaller tab sets are used to send commands and calibration constants to the implant (top tab set) and to monitor messages and RSSI from the implant (bottom tab set).

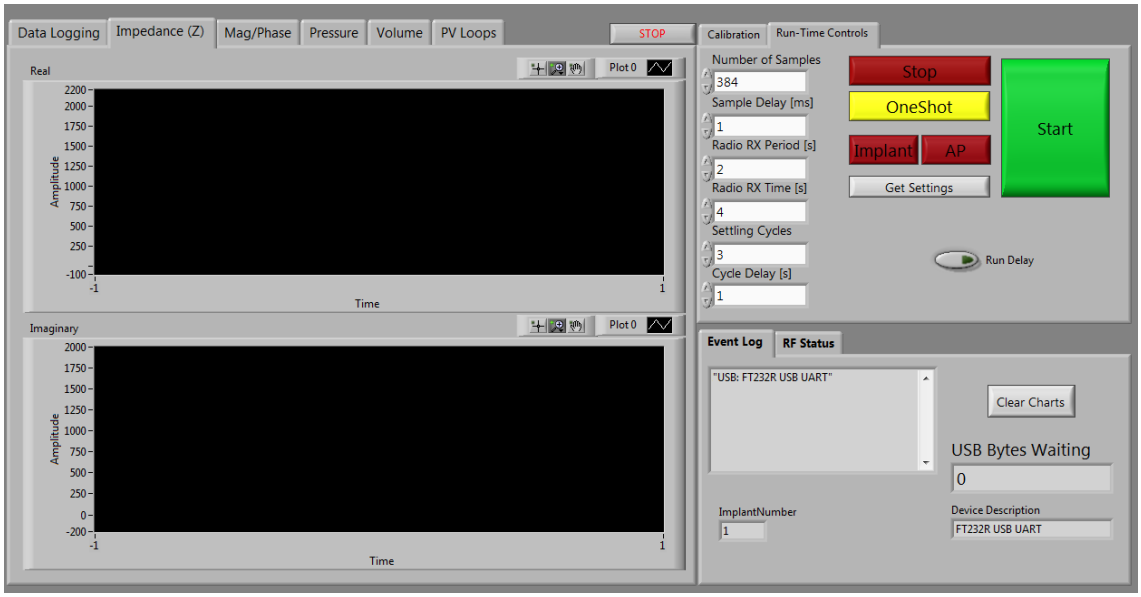

Figure 16: Fullscreen LabVIEW Interface

Figure 17 shows the "Calibration" and "Run-Time Controls" tabs in more detail. To change epoch collection settings from the "Run-Time Controls" tab, variables are adjusted at the right-most side of the tab. Pressing the large green "Start" button puts the specified settings in the access point queue to be sent the next time the implant awakens and issues a "CTS" ("Clear To Send") message, which is displayed on the "Event Log" tab. The implant or the access point can also be reset from LabVIEW by pressing the red "Implant" or "AP" buttons. However, one must wait for the implant to issue a "CTS" before the circuit can be reset by software. The "Run Delay" button activates a delay module in the main LabVIEW processing loop to conserve CPU processing cycles. During implantation, this run delay is inactivated so that data buffers don't overflow.

The calibration tab has two main segments for pressure and volume. In the pressure segment, the "Pressure HW Offset" variable controls the digital potentiometer

on the implant. Changing this value puts the new potentiometer wiper position in the access point queue (8 bit wiper register gives 255 positions). This hardware offset must be correctly adjusted to bring the pressure into rage at the beginning of any experiment. The remaining variables on this tab apply a nominal gain, offset, and phase (for admittance data) for data representation in LabVIEW only. Raw, uncalibrated data is recorded in the output text files. This scheme allows the user to determine if the incoming data is reasonable based on previous calibrations, but still provides flexibility for precise calibration from raw files. A list of each LabVIEW control and its corresponding nominal value and range is presented in Table 3.

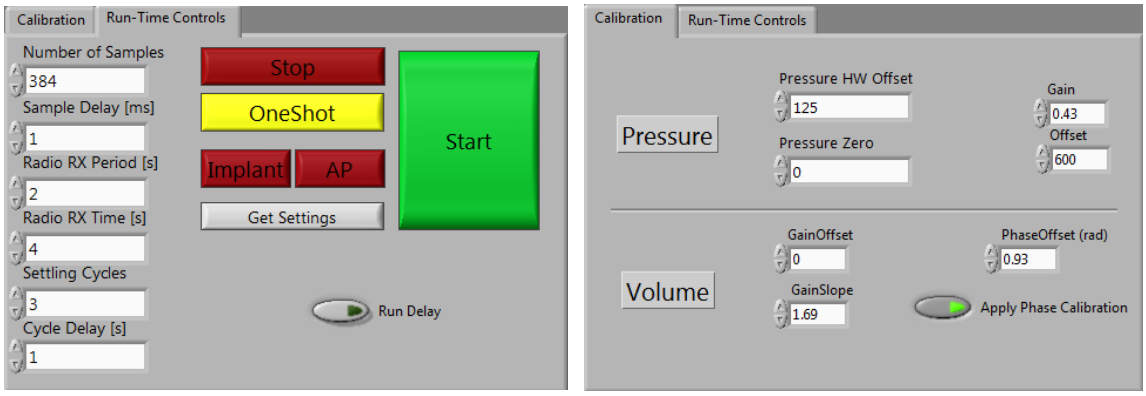

Figure 17: LabVIEW Runtime Controls (left) and Calibration (right) Tabs.

Table 3: LabVIEW Interface Variables

GUI Segment	Parameter	Typical Value	Range
Run-Time Controls	Number of samples	384	1 to 384
	Sampling period [ms]	1	≥ 1
	Radio RX period [s]	2	≥ 1
	Radio RX time [s]	4	≥ 1
	Settling Cycles	3	≥ 0
	Cycle Delay [s]	600	0 to 65535
Calibration Tab	Pressure Gain	0.43	Double value
	Pressure Offset	300	0 to 1024
	Pressure HW Offset	130	0 to 255
	Volume Gain Offset	0	Double value
	Volume Gain Slope	1.7	Double value
	Volume Phase Offset [rad]	0.9	Double value

Chapter 3: Implant Manufacturing

The physical assembly of the implant is one of the most challenging aspects of this project. The catheter is very delicate and a series of heating, gluing, and sealing procedures introduce the potential for damage.

There are several design requirements that are addressed in the assembly of the implant. The cavity where the implant is placed between the rat's shoulder blades is dynamic, so the implant assembly should allow for motion of the catheter. If the catheter is bent at too sharp of an angle, it can kink and break the wires inside. The rat is flexible and can nearly reach the implantation site, so the battery charging interface should be as small as possible. To prevent adverse tissue reaction, the implant should be biocompatible. Finally, the circuit must be sealed against moisture.

3.1 Attaching the Catheter

The shape of the ambulatory rat can be seen as a continuum between two positional extremes: hunched and elongated. Since the catheter is positioned along the long axis of the rat, lateral motion of the catheter along the long axis of the implant should be accounted for. To do this, the catheter is formed with a 180° bend as shown in

Figure 18. Figure 18 shows the shape of the catheter over a 2.5 cm lateral displacement.

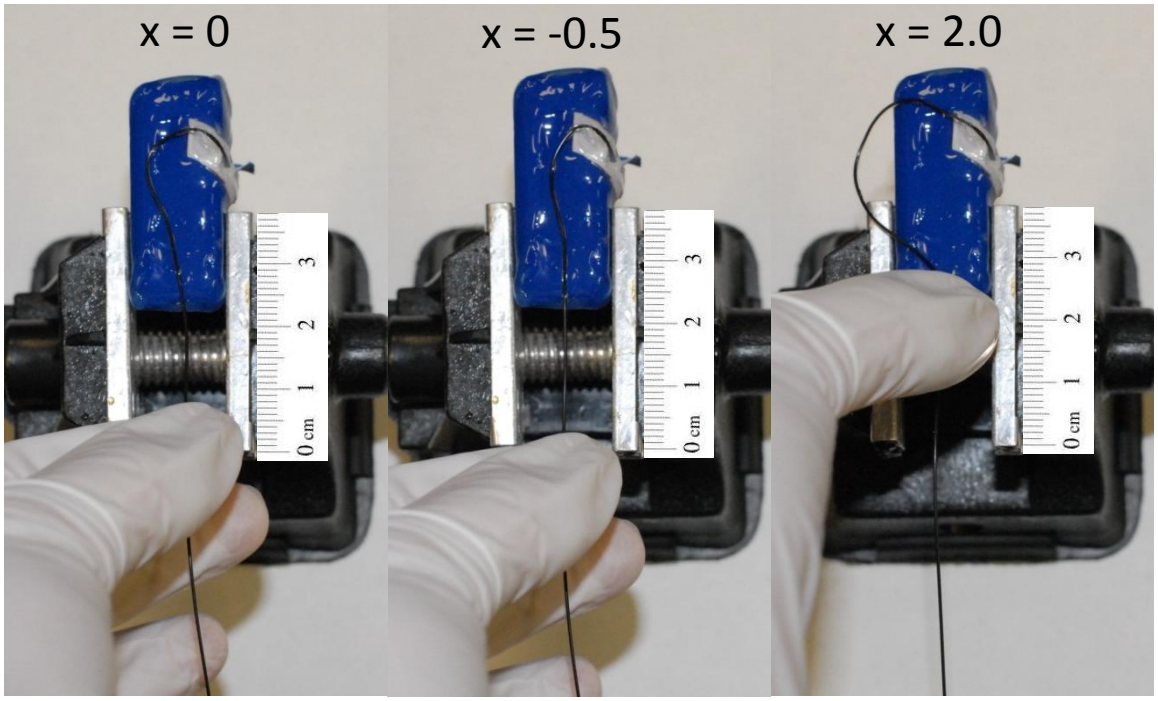

Figure 18: Displacement of Catheter Along Long Axis

The catheter is formed by gentle heating with a hot air gun. A ceramic mold was created to hold the catheter in place during heating to reliably produce the desired bend. In the final implant assembly the battery is placed directly over the circuit, and the catheter is attached to the inward-facing side of the circuit, so the bending mold includes one sloped side near the attachment point of the catheter to account for the width of the battery. This allows the formed catheter to lie just on top of the battery in the finished implant.

The catheter is electrically connected to the circuit by direct soldering. The footprint of the catheter connection point in the circuit is that of a 2x4 8-pin, 50mil

connector, so test loads may be applied to for calibration. An illustrated procedure for attaching the catheter to the implant circuit can be found in Appendix A.

3.2 BATTERY CONSIDERATIONS

The implant uses a lithium polymer battery from www.powerstream.com. LiPo batteries are available in a variety of form factors, with batteries approximating the size of the implant circuit having capacities in the range 40-150 mA-hr. The battery used in most of the implants is a 130 mA-hr battery with a volume of 4x12x35 mm or 1.68 cm^3, and a weight of 2.3g.

These batteries are relatively inexpensive and capable of failure. For this reason, each battery was tested through a charging/discharging procedure to ensure functionality and verify the energy capacity. Each battery was charged using a LiPo battery charger delivering a maximum current of 0.1 A (minimum setting). Average charging times for viable batteries were about 75 minutes. Some dysfunctional batteries were identified due to shorter charging times. With full charge, a test discharge was performed across a resistor such that the battery delivered 100 mA on average. A trace for discharge current over time was recorded and the area under this curve was calculated to get a measure of total energy delivered on one charge. Ten viable 130 mA-hr batteries were tested and found to achieve 91.2±3.2% efficiency (n=10). Three 150 mA-hr batteries were tested and found to achieve 88.5±3.2% efficiency (n=3).

During implantation of the circuit, PV data must be transmitted nearly continuously as the pressure signal is used to determine when the catheter passes from the

aorta into the LV. A typical implantation can take about an hour, draining the battery at this fast collection rate. To improve the lifetime of the battery after implantation, power and ground leads are externalized so that the battery can be recharged. Several iterations of a battery charging connector were attempted as described in Section 3.5.

3.3 SEALING THE CIRCUIT

The implant must be sufficiently sealed for biocompatibility and reliability of the circuit. There are three basic layers of encapsulation over the circuit. 3M DP-270 epoxy potting compound is applied directly to the circuit to provide basic waterproofing. This ensures that any moisture trapped inside the implant during manufacture, or introduced after surgery does not create parallel conductive paths on the circuit. The potting compound is also used to glue the battery to the circuit.

Electrical tape is used to create a smooth surface over which silicone can be applied. This improves uniformity of the hand-applied silicone layer. The electrical tape also allows for the implants to be different colors, a feature that provides a quick identification method.

Dow Corning 734 flowable sealant is used as the final sealant layer. This silicone is biologically inert and provides the outer layer of protection against moisture.

3.4 Bench Testing and Calibration

3.4.1 Test Loads Before Catheter Attachment

Test loads are applied before attaching the catheter to the implant circuit to ensure that the circuitry is functional. A resistor switchbox is used to sweep a resistive load to the circuit from 200 to 2000Ω in 100Ω steps. Next, a capacitor switchbox in parallel with a 1000Ω resistor is used to sweep the load through the impedances 1000Ω || (4nF, 10nF, 20nF, 30nF, 40nF). The parallel resistance is necessary for the capacitor sweep because the current source has difficulty driving a purely capacitive load. The resistor and capacitor sweep are used to determine the phase offset of the admittance measurement circuitry. During calibration, phase offset is adjusted until the imaginary component of the resistor sweep is minimized. Gain may also be applied to the signal such that the real component of the resistor sweep matches the nominal value set.

A test catheter fitted with an 8-pin connector is used to verify that the pressure measurement circuitry is functional. The sensor end of the test catheter is placed in a closed, saline-filled pressure chamber with an attached syringe. The digital balancing potentiometer in the pressure circuit is controlled through the "Pressure HW Offset" variable in LabVIEW. This value is adjusted until the pressure signal comes into range. Slight force applied to the syringe plunger ensures that the analog circuitry is functional.

3.4.2 Test Loads After Catheter Attachment

After the permanent measurement catheter is attached to the circuit, saline calibration data is collected so that probe capacitance may be removed. The catheter is

introduced to a series of large saline containers approximating infinite conducting mediums with conductivity values of 1000, 2000, 3000, 6000, 8000, 11000 µS/cm.

The pressure hardware offset for the measurement catheter is determined as before, by varying the digital potentiometer value through LabVIEW until the signal comes into range. Pressure gain is determined using a Scisense pressure measurement system as truth. A test catheter interfaced to the Scisense box is placed in the same pressure chamber as the measurement catheter (attached to the circuit). ADC output values from the implant pressure circuit at 0 and 100 mmHg are recorded and used to calculate pressure gain.

Current consumption during sleep and data collection is measured for each implant as well. A Fluke multimeter with a µA range setting is used to measure the sleep current, which is typically in the 1-5µA range. The circuit shown in Figure 19 is used to provide a trace of current consumption versus time during a data epoch. This data is used to estimate implant battery life as described in Section 2.4.

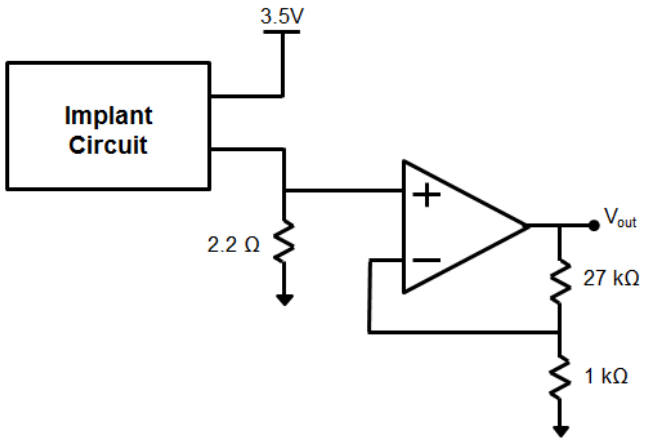

Figure 19: Supply Current Measurement Circuit

3.5 Evolution of the Implant

3.5.1 Implant Version 1

In the first fully implanted system, the catheter was made to be detachable so that the circuit could be reused. Eight 30-guage wires left the implant and connected to the 2x4 8-pin 50-mil connector. The catheter was attached to the complementary connector and the interface was sealed with silicone. Power and ground were on two of the connector pins and the procedure for recharging included opening the rat's dorsal incision to expose the circuit, disconnecting the catheter, connecting the battery charger and charging the circuit, then reconnecting the catheter. It was found that the connectors were too small and slippery (after implantation) for this to be a feasible option. What's more, the 8-wires exiting the implant proved hard to seal appropriately, and liquid seeped into the circuit at the catheter interface between the wires.

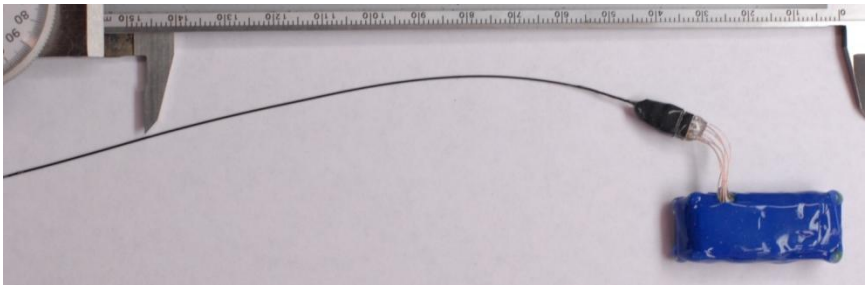

Figure 20: Version 1 Implant

3.5.2 Implant Version 2

In the next iteration of the implant, the catheter was attached directly to the circuit and two wires for charging were soldered to the same 8-pin connector as before (4-pins per wire for stability). Two implants were constructed in this manner, and in both

experiments the rats removed the battery connector by scratching. Post-mortem evaluation of the implant showed that the circuit was mostly moisture-free, though some of the pins of the microcontroller were slightly corroded.

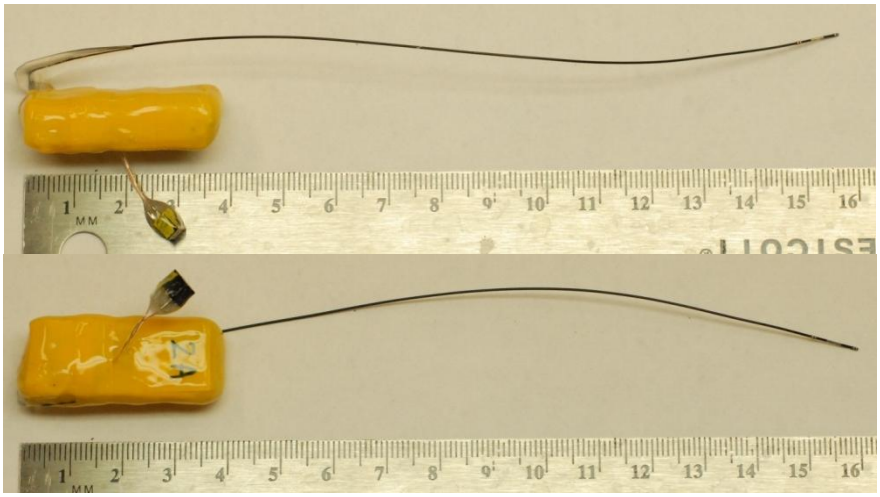

Figure 21: Version 2 Implant

3.5.3 Implant Version 3

In the latest implant revision to date, the catheter is directly attached to the circuit as in version 2, but the battery connector simply consists of two wires sealed together with silicone. The power wire is longer than the ground wire to prevent the battery from shorting. During implantation, the exposed wires are taped such that they do not short if they are touching a metal surface. The waterproofing procedure has also been improved in this version of the circuit to include potting compound that ensures that no moisture causes degradation of the signals or the battery life. The method for permanently attaching the catheter from version 2 and potting the circuit in this version have made the implant more robust, but have limited it to single use.

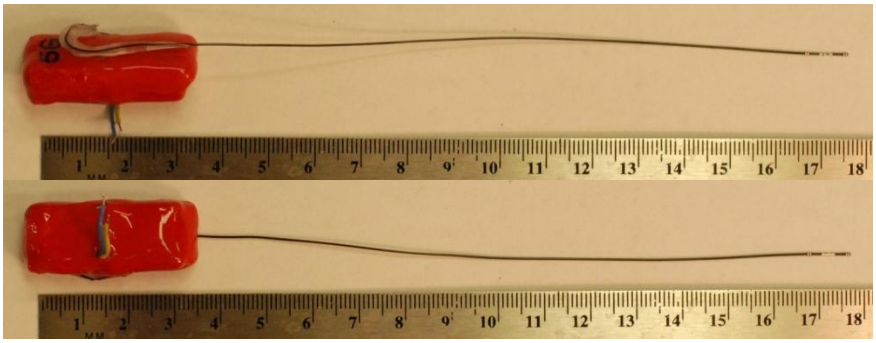

Figure 22: Version 3 Implant

Chapter 4: Volume Calibration

4.1. Overview

Accurate calibration of the admittance channel is both important and non-trivial. Figure 23 illustrates the physical error sources for the volume channel and Figure 24 provides a flowchart for removing these errors. Briefly, the first calibration step is to determine the phase offset and gain of the analog circuitry in the implant using resistive and capacitive test loads. The next step is to determine the permittivity error for the catheter with saline test loads. The final step is to determine an appropriate sigma-epsilon ratio such that the absolute volumes calculated with Wei's equation correspond to ultrasound measurements. Each of these steps is explained in detail in the following sections.

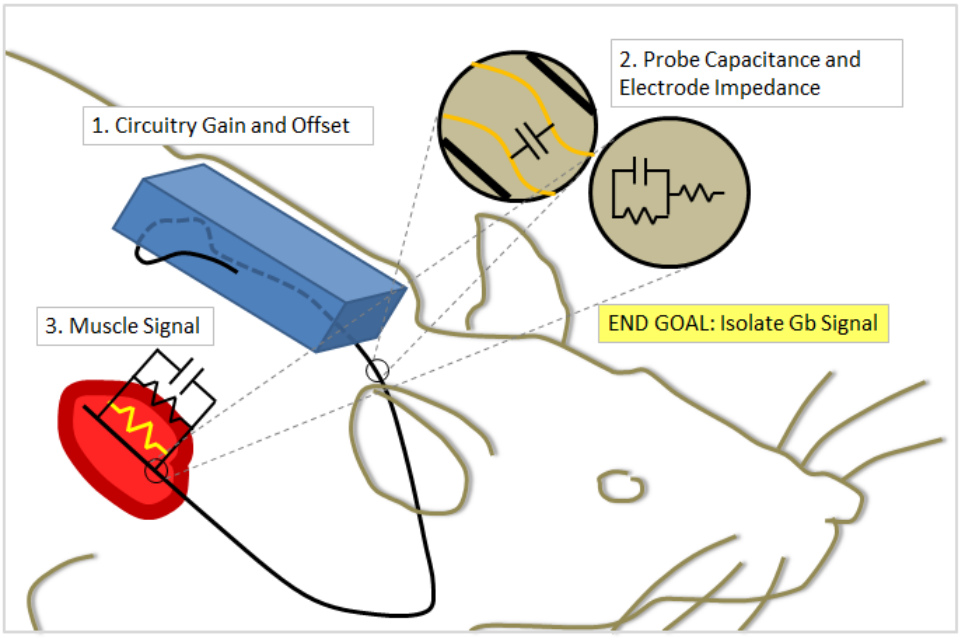

Figure 23: Error Sources Requiring Calibration

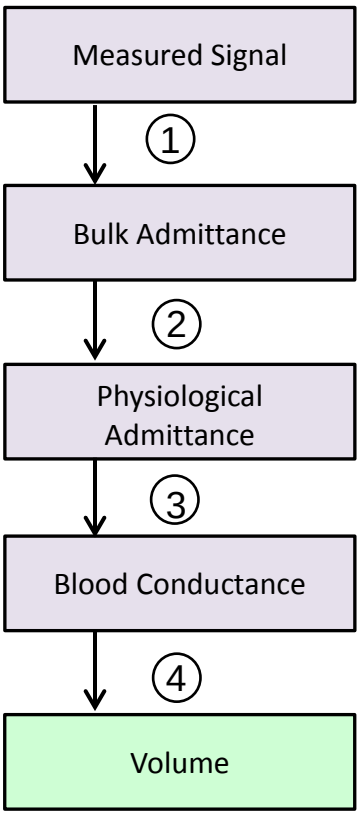

1. Circuit Calibration:
   - Performed on circuit only, using test connector.
   - Data needed: Resistor Sweep, Capacitor Sweep (bench)
   - $Y_{bulk} = k_{gain} Y_{meas} \exp(\frac{jk_{phase}}{180\pi})$
2. Remove Probe Capacitance:
   - Performed with real catheter (ready to implant)
   - Data needed: Saline Sweep (bench)
   - Imaginary probe error estimated by linear fit to imaginary signal vs. real signal in saline.
   - $Im_{phys} = Im_{bulk} - (aRe_{meas} - b)$
3. Remove Muscle Signal:
   - Data needed: sigma-epsilon ratio (numerical search)
   - $G_b = Re_{phys} - Im_{phys} \frac{\sigma_{blood}}{2\pi f \varepsilon_0 \varepsilon_{r,blood}}$
4. Convert to Volume:
   - Data needed: Stroke Volume , EDV -- ESV (ultrasound).
   - $V = \frac{\gamma(SV)}{\gamma(SV) - G_b} \rho L^2 G_b$

Figure 24: Implant Calibration Flowchart

4.2 Instrument Calibration

The goal for calibration of the circuitry is to determine the phase delay and gain of the admittance measurement block. This phase delay is a result of analog filtering and current source output to ADC input delay in the MCU, and is partially affected by the variable load. The load affects the location of a system pole located roughly one decade above 20kHz. This pole is high enough in frequency that the effects on the magnitude response are negligible, but phase response is dynamic within ±1 decade of the 3dB corner frequency. The phase shift at 20kHz is only a few degrees, but ratios of real to imaginary admittance measured in the rat heart are large, roughly 10:1 to 50:1. So small

phase errors translate to large errors in the imaginary component, and subsequent uncertainty the removal of the muscle signal.

A virtual testbench for the admittance measurement circuitry was created in National Instruments' Multisim. This testbench included spice models for the active circuit elements (amplifiers) and ideal models for the passive components. To investigate the effects of load-dependent pole movement in the circuitry, an ideal resistor representing the test load was swept from 200 to 2000Ω. The modeled response is compared to the response measured from a physical circuit in Figure 25. A constant phase angle was subtracted from the measured data to account for the MCU current source output to ADC input delay which is not present in the model. The model matches the measured data well.

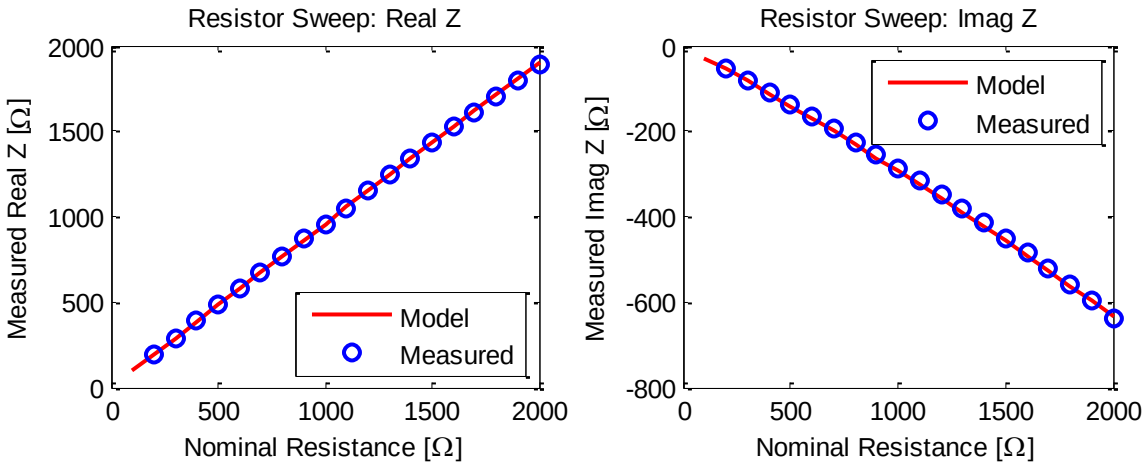

Figure 25: Uncorrected Resistor Sweep

To better illustrate the effects of load-dependent pole movement, a secondary constant phase angle was subtracted from the model and measurement (same angle

subtracted from both data sets) to account for filtering not associated with the load. The non-zero imaginary impedance shown in Figure 26 indicates that a constant phase angle subtraction is not sufficient to correct for the phase error in the system. This result is not ideal and could be identified as an area for improvement for future iterations of the circuit.

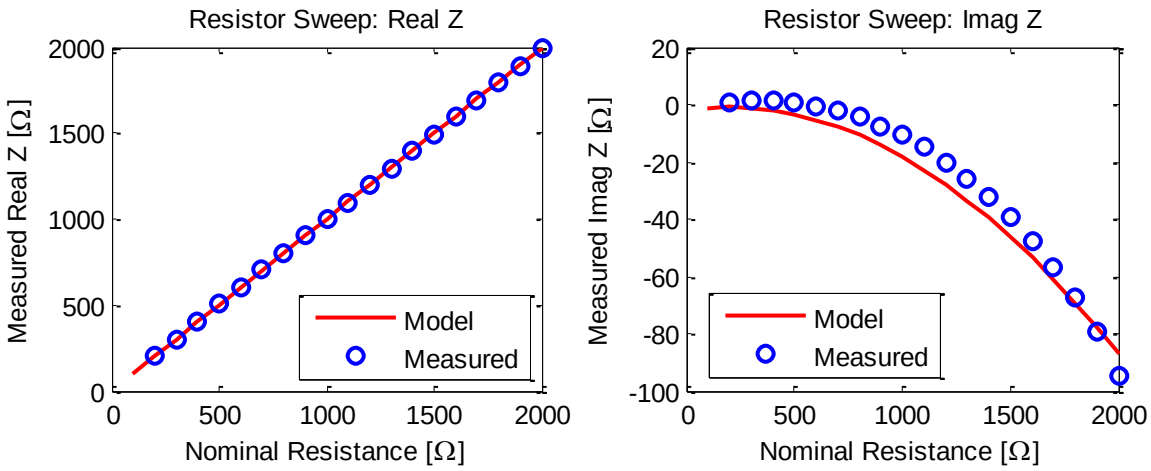

Figure 26: Resistor Sweep After Constant Phase Angle Subtraction

To correct for load-dependent phase error, an interpolation method was used. Using the real impedance (resistance) to phase error relation measured in the resistor sweep as a lookup table, interpolated values for phase offset were subtracted on a point by point basis for all data sets associated with a given implant circuit. To test this calibration method with a load containing an imaginary impedance component, a purely capacitive load was swept from 4nF to 30nF in the Multisim testbench and the dynamic phase correction was applied. The real part of impedance for a capacitive load should be zero; Figure 27 shows that the phase angle interpolation does leave some real impedance

error but the error is much smaller than that remaining from the constant phase error subtraction (same constant phase used to generate Figure 26) which doesn't give the correct result.

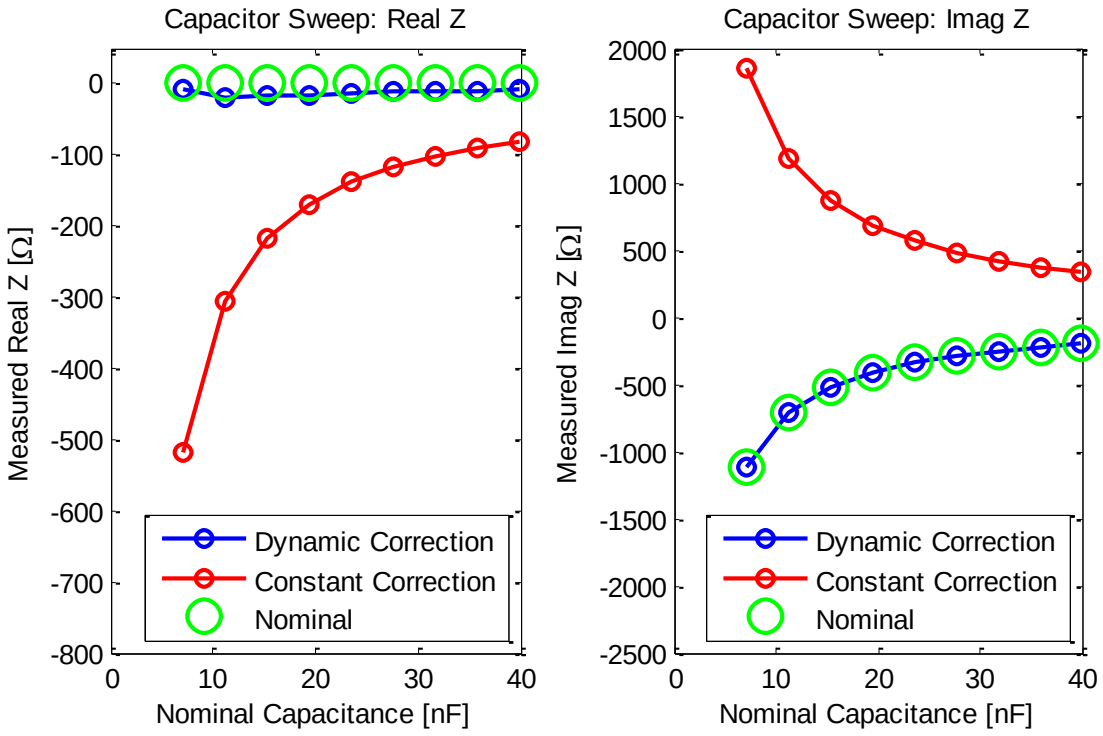

Figure 27: Capacitor Sweep

4.3 Probe Calibration

A saline calibration is used to determine the permittivity error contributed by the catheter. This error is a result of the parallel capacitance between electrode wires in the catheter lumen, and the series impedance of the electrode/electrolyte interface. The relative permittivity of water is approximately 80 below 100 kHz, so the imaginary component that it introduces into the admittivity, $j\omega\varepsilon = j2\pi$ (20,000 Hz)(80)(8.85e-12) = j*0.89 μS/cm at 20 kHz is negligible compared to the real part for the saline solutions

used: σ = 1000 to 11000 μS/cm. Correction for parasitic elements in the catheter was accomplished by introducing the catheter to a set of saline solutions with variable conductance to characterize permittivity error.

The Multisim model for the catheter is shown in Figure 28. Each *CpXY* capacitor models parallel capacitance between electrode wires *X* and *Y*. Each of the 4 electrodes has an impedance composed of the three elements shown in Figure 29. The nominal values for the electrode impedance elements are generalized from measurements on Scisense surface probes with platinum electrodes [13]. In general, the extended model for a long wire would include a series inductance. Previous work has shown that the measurement is insensitive to physically reasonable wire inductance values, so these elements were neglected [14].

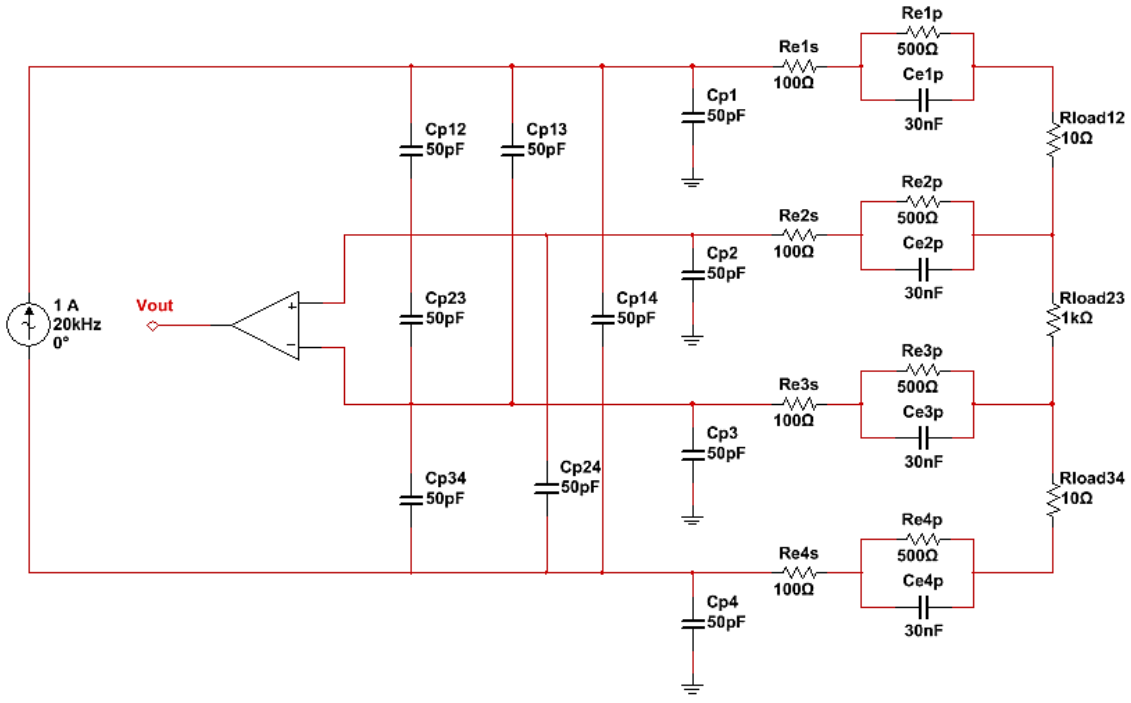

Figure 28: Non-Ideal Catheter Model

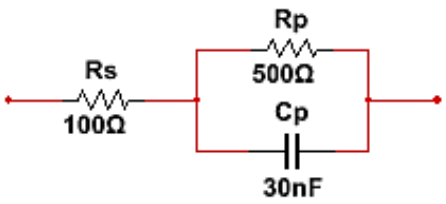

Figure 29: Electrode Impedance Model

Assuming equal electrode impedances and equal parallel capacitance between any two wires, the Multisim model for the catheter was inserted into the same testbench used to perform the resistor calibration. The dominant load resistor (*Rload23*) was swept through the values (1/1000µS, 1/2000µS, 1/3000µS, 1/6000µS, 1/8000µS, and 1/11000µS). Phase correction from the resistor sweep was applied to these data. The *ImY* to *ReY* relation from the model is compared to the same sweep of saline conductances for three separate implants in Figure 30. In this figure, each implant sweep is represented by a blue line. This data is bounded by two red lines representing the modeled saline sweep output with a 10pF (top) and 70pF (bottom) probe capacitance values. Previous work determined that interwire capacitances for similar probes is about 50 pF, so the saline sweep data measured from the implant is reasonable [13]. The saline sweep points from each implant are used in a lookup table to interpolate load dependent probe error in the imaginary component of admittance. This error is subtracted from the measured susceptance as described in Section 1.4.

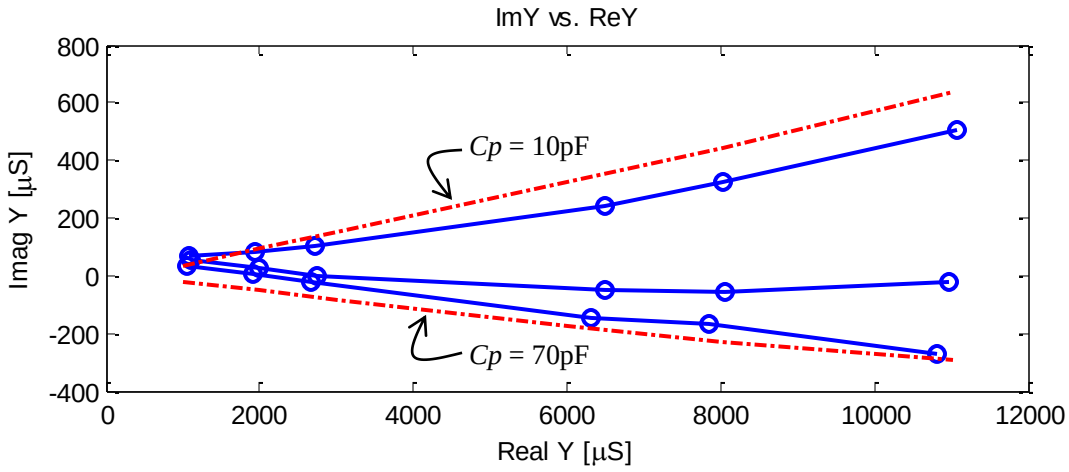

Figure 30: Saline Sweeps

4.3.1 Limitations of the Saline Calibration Method

The modeled results for the saline calibration presented above assume that electrode impedance is constant for varying saline concentrations. This may not be a valid assumption. Consider the physical basis for R_S, R_P, and C_P in the electrode model. C_P represents the electrode/electrolyte interface capacitance, R_P represents the charge transfer resistance, and R_s represents the solution resistance. A modeling study presented in [15] provides insight into how these circuit elements change with saline conductance. In general, the model suggests that each element decreases in magnitude with increasing solution conductivity.

4.3.1.1 Interface Capacitance, C_P

C_P [F] in this model is a simplification of a constant phase angle impedance Z_{CPA} that is dependent on the degree of inhomogeneity at the electrode/electrolyte surface according to (18). In (18) Q describes the magnitude of the impedivity of Z_{CPA}, and n

characterizes inhomogeneity where $0 \leq n \leq 1$ and $n = 1$ for a pure capacitor. Frequency sweeps of the electrode response are required to determine n.

$$Z_{CPA}(\omega) = \frac{1}{(j\omega Q)^n} \quad (18)$$

A theoretical value for the area-dependent interface capacitance, C_I [F/m^2], can be derived from the Gouy-Chapman-Stern model, where the total interface capacitance is given as the series combination of the double layer capacitance C_H [F/m^2] (also called Helmholz capacitance) and the diffuse layer capacitance C_G [F/m^2] (also called Gouy-Chapman capacitance). The formulas for the Helmholz and Gouy-Chapman capacitances are given in (19 **)**.

$$\frac{1}{C_I} = \frac{1}{C_H} + \frac{1}{C_G} = \frac{d_{OHP}}{\varepsilon_0 \varepsilon_r} + \frac{L_D}{\varepsilon_0 \varepsilon_r \cosh(\frac{z\phi_0}{2U_t})} \quad (19)$$

Here, d_{OHP} is the thickness of the double layer [m], ε_0 the permittivity of free space [F/m], ε_r the relative permittivity of the double layer, z the charge of the ionic species, ϕ_0 the applied electrode potential [V], U_t the thermal voltage [V], and L_D the Debye length [m] specified as,

$$L_D = \sqrt{\frac{\varepsilon_0 \varepsilon_r U_t}{2n^0 z^2 q}} \quad (20)$$

where n^0 is the ionic concentration of the solution [m^{-3}] and q is the elementary charge [15]. From these formulas we see that at the very least the Gouy-Chapman component of the interface capacitance is proportional to $1/\sqrt{n^0}$, and so would change with the saline conductivity.

4.3.1.2 Charge Transfer Resistance, $\mathbf{R_P}$

The area-dependent charge transfer resistance, R_P [Ω-m^2], is dependent on the equilibrium exchange current density, J_0 [A/m^2], which is a measure of the equal but opposite reduction/oxidation currents flowing across the electrode/electrolyte interface according to (21 **)**.

$$R_P = \frac{RT}{J_0 zF} \qquad (21)$$

Here, R is the universal gas constant [J/mol-K], T is temperature [K], z is the number of electrons in the redox reaction, F is Faraday's constant [C/mol], and J_0 is the equilibrium exchange current density which is dependent on the concentration of electron-acceptor ions at the interface, c_A [mol/m^2], the reduction reaction rate constant, k_c [s^{-1}], the symmetry factor β, and the equilibrium potential, $\Delta\phi_0$ [V] as described by (22 **)**.

$$J_0 = Fk_c c_A e^{\frac{(-\beta F \Delta\phi_0)}{RT}} \qquad (22)$$

Assuming that the concentration of ions near the electrode/electrolyte is proportional to saline conductivity, R_P would be inversely proportional to saline conductivity.

4.3.1.3 Solution Resistance, $\mathbf{R_S}$

Considering that the R_S [Ω] component in the electrode model is intended to characterize the solution resistance, it is clear that this value will change with saline conductivity. In general,

$$R_s = \frac{F_G}{\alpha} \qquad (23)$$

where α is the solution conductivity [S/m] and F_G is the geometrical form factor [m^{-1}] for the electrode (ln4/πl for square electrodes and 1/4r for round electrodes).

Complex characterization of the electrode impedances for the Scisense tetrapolar rat catheter is beyond the scope of this design project. But the equations above provide a framework for re-considering the saline calibration in future studies. Equations for R_S, R_P, and C_P from [15] suggests that the impedance of each element decreases with increasing solution conductivity.

4.4 SIGMA-EPSILON RATIO OPTIMIZATION

These rat experiments were performed closed-chest, making a direct measurement of the sigma/epsilon ratio of the heart muscle impossible. However, this ratio is an important parameter in the admittance to volume conversion as it determines what portion of the real part of admittance is subtracted as muscle conductance (see equation (6 **)**). Wei's equation uses stroke volume determined from ultrasound (EDV-ESV = SV) to derive calibrated volume from blood conductance, G_b, such that the calculated SV matches the measured SV. However, absolute volume is a function of the sigma-epsilon ratio. A closed form solution of Wei's equation as a function of sigma-epsilon ratio is difficult to derive because the non-linear correction factor, γ, is the larger solution to a quadratic equation that depends on G_{b_es} and G_{b_ed}, numbers that are dependent on the sigma-epsilon ratio as shown in equations (24 **)** and (25 **)**. Therefore, numerical methods were used to find a value for the sigma-epsilon ratio that minimized the error between measured (ultrasound) and calculated EDV and ESV.

$$G_{b\_es} = G_{es} - B_{es}(\frac{\sigma}{\varepsilon})(\frac{1}{2\pi f}) \quad (24)$$

$$G_{b\_ed} = G_{ed} - B_{ed}(\frac{\sigma}{\varepsilon})(\frac{1}{2\pi f}) \quad (25)$$

G_{es} and G_{ed} are the real components of physiological admittance [S] (lumped blood and heart muscle) at end systole and end diastole, respectively. B_{es} and B_{ed} are the imaginary components of physiological admittance [S].

To get an average value for G_{es}, G_{ed}, B_{es}, and B_{ed} for the admittance calibration trace (recorded during ultrasound volume measurement), a peak-finding algorithm was implemented in MATLAB. Figure 31 below shows a typical output for this algorithm.

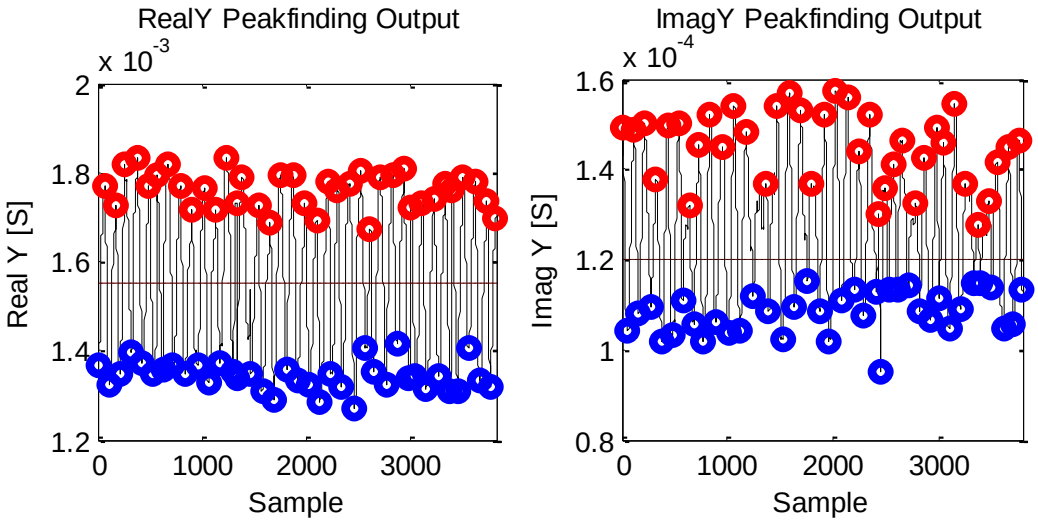

Figure 31: Output of Peak Finding Algorithm.

In general, the real part of admittance is maximized at end diastole when the blood volume in the LV is largest, and the imaginary part is maximized at end systole when the muscle is closest to the catheter. So, the positive real Y peaks were averaged to find G_{ed}, the positive imaginary Y peaks were averaged to find B_{es}, and vice versa for the

negative peaks. These four parameters are passed as constants to the sigma-epsilon search algorithm and used to determine sigma-epsilon dependent values for G_{b_ed} and G_{b_es}. For each sigma-epsilon number, Wei's equation is used to calculate volume, the peak-finding algorithm is used to determine the average calculated EDV (positive peaks) and ESV (negative peaks), and an error measure is calculated by,

$$e = (EDV_{meas} - EDV_{calc})^2 + (ESV_{meas} - ESV_{calc})^2 \quad (26)$$

The sigma-epsilon ratio for which this error term is minimized is recorded and used for all further processing of the data for this implant. An example output of this algorithm showing calibrated volume is given in Figure 32. The dotted lines represent EDV (red) and ESV (blue) measured by ultrasound, and the black trace is calculated volume. The PV loops resulting from this calibration method are shown in Figure 33. Again, the dotted lines represent EDV and ESV from ultrasound.

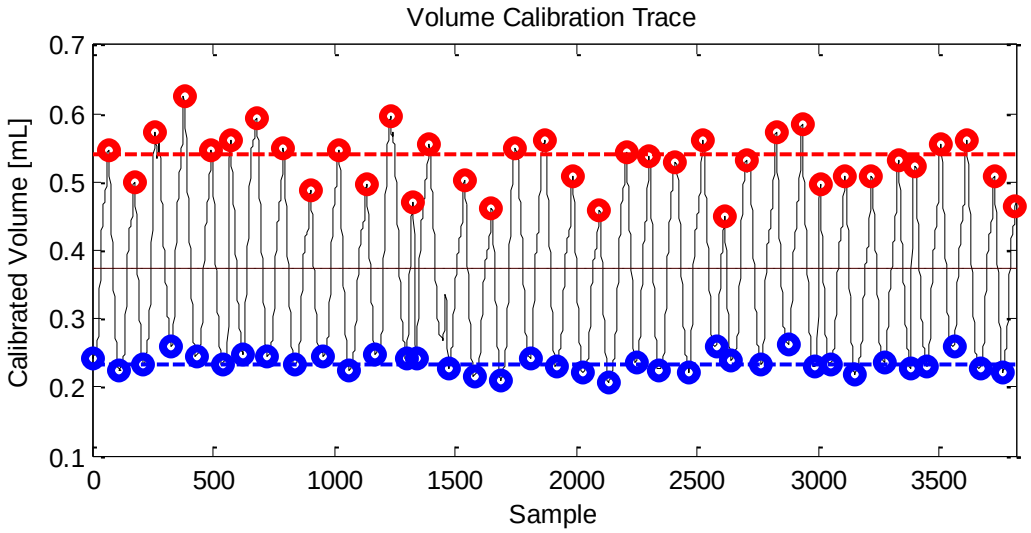

Figure 32: Calibrated Volume After Sigma-Epsilon Ratio Search

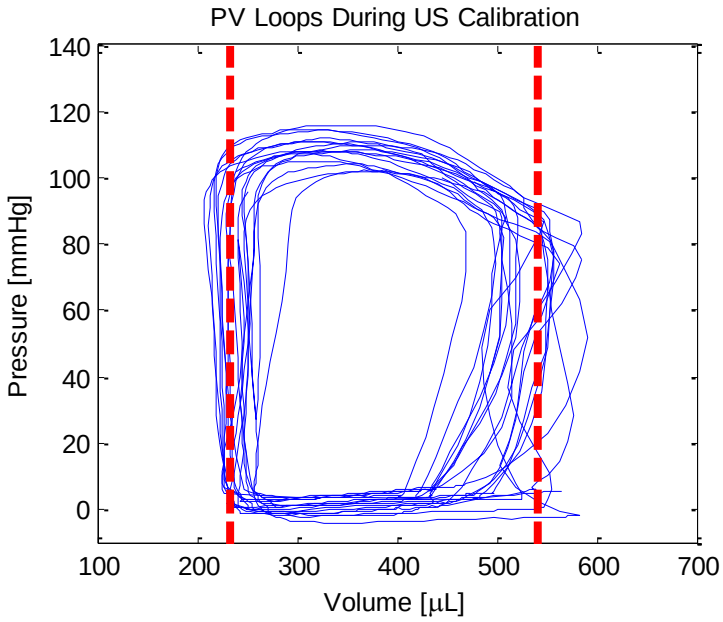

Figure 33: PV Loops After Sigma-Epsilon Ratio Search Algorithm

Table 4: Numerically Determined Best-fit Sigma-Epsilon Ratios

Experiment	**Best-fit σ/ε**
Rat 3	0.54×10^6
Rat 4	1.04×10^6
Rat 5	1.34×10^6
Rat 6	0.21×10^6
Rat 7	0.63×10^6
Rat 8	NA
Average	$(0.75 \pm 0.44) \times 10^6$

Table 4 reports the best-fit sigma-epsilon ratio for each of the 6 experiments. As a reference point, surface probe measurements from Raghavan's 2004 rat experiments specify an average sigma-epsilon ratio of 1.40×10^6 [10]. The Scisense Advantage system uses sigma-epsilon value of 0.88×10^6, which is consistent with the data Table 4

and is derived by a similar empirical optimization method. Discrepancy in sigma-epsilon values from these sources, and the relatively large standard deviation in the optimized sigma-epsilon ratios from this work, suggests that there is room for improvement in determination of sigma-epsilon ratio.

In the G_b to volume calculation, blood resistivity, ρ_{blood}, is assumed to be a constant, literature-derived value. If this value is incorrect, the optimized value for sigma-epsilon ratio will represent overcompensation. Blood conductivity variation is considered more carefully in Section 5.3.1.

Chapter 5: In-vivo Experiments

5.1 Implantation Procedure Summary

All implantation procedures were conducted at the University of Texas Health Science Center San Antonio (UTHSCSA) by a veterinary technician. To begin, a rat is anesthetized with 1-2% isoflourane and the area between the shoulder blades is shaved. The rat is placed on a heated surgery stage which records body temperature and EKG signals during ultrasound. A pre-surgery ultrasound is conducted to determine the original volume of the heart. This step also allows the veterinarian to determine if the heart has any inherent defects. A vertical midline cervical incision in made to expose the right common carotid artery. The rat is positioned dorsal side up and another vertical incision is made between the shoulder blades. A metal tube is used to guide the catheter under the skin on the right shoulder from the dorsal to the ventral incision. The rat is again turned ventral side up. The carotid artery is opened and the catheter is inserted. The veterinarian guides the catheter down the carotid artery and into the left ventricle of the heart. The pressure signal from the implant is used to determine when the catheter reaches the heart, as this event causes the pressure trace to change from a distinct aortic, to ventricular pattern. Ultrasound and PV loop shape are used to verify correct positioning of the catheter in the ventricle. The admittance data collected during this ultrasound measurement is used to correlate minimum and maximum blood conductance values to end systolic and end diastolic volume (ESV and EDV), respectively. The catheter position is then stabilized with sutures near the entry site of the carotid artery.

The ventral incision is closed and the rat is turned ventral side down. The circuit is then positioned underneath the skin between the shoulder blades and the dorsal incision is closed. During surgery, the circuit transmits with minimal cycle delay (cycle delay set to zero gives one epoch every 10 seconds) and so consumes battery power. The battery is recharged while the rat is still under anesthesia to improve implant lifetime. The implantation procedure lasts about 2-3 hours.

5.2 Implant Timelines

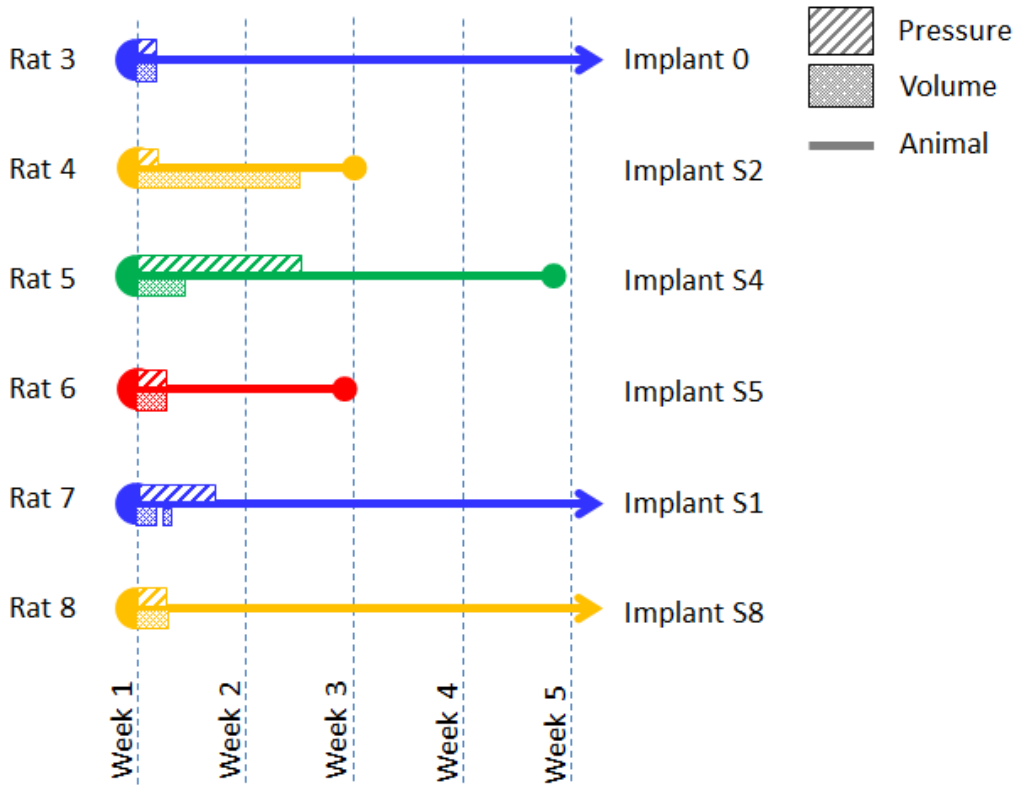

Figure 34: Implant Timelines

There were 6 full implant procedures. Figure 34 represents schematically the timeline of each implant, indicating the time for which valid pressure and volume data was collected. Experiment numbers are given on the left and implant ID numbers on the right. Note that the longest period for which valid data was collected was about ten days. Implantation day loops for each implant are shown in Figure 35 Let us examine the performance of each implant.

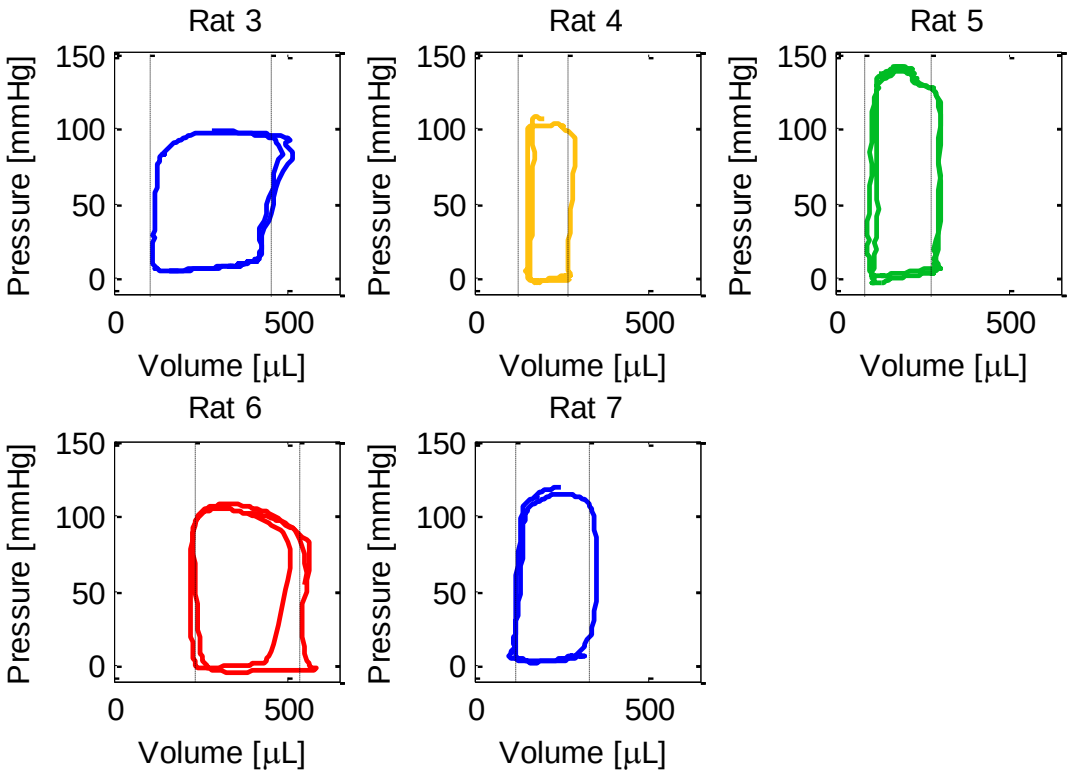

Figure 35: PV Loops on Implantation Day

5.2.1 Rat 3, Implant 0

Rat 3 was the first full-implant experiment, and utilized the version 1 device with an externalized catheter connector (Figure 20). Valid pressure and volume data was

collected on day 1, the implantation day, but the battery was drained by day 2. A recharge procedure which included disconnecting the catheter, connecting a battery charger, and reconnecting the catheter in-vivo failed due to the small size of the catheter and the slippery silicone coating. The circuit was removed during this attempted recharge procedure, but the catheter was left in place to investigate tissue interaction effects on catheters implanted long term.

5.2.2 Rat 4, Implant S2

Implant S2 and S4 were the last implants used in experiments that included a code bug that allowed excess current consumption in sleep mode. The sleep current of implant S2 was measured at ~30μA before implantation and ~250μA during failure analysis after retrieval. Thus, implant S2 had a very short (about 1 day) battery life. Fortunately, the version 2 device used for Rat 4 was more easily rechargeable. This allowed us to collect admittance data over a 10-day time span. The pressure signal stopped giving valid data after day 1. Dissection of the circuit after implantation suggests that a pressure wire was broken near the tip of the catheter. The experiment was stopped when the rat chewed or scratched off the battery connector, making recharging impossible.

5.2.3 Rat 5, Implant S4

Despite the code bug present in version 2 of the circuit, Implant S4 lasted 23 days on a single charge. This implant provided the most complete data set, as the catheter was intact for 11 days. Valid pressure data was measured over these 11 days, but on day 4 the catheter became lodged in the papillary muscles (verified through ultrasound), causing

the volume signal to become non-physiological. From days 6-14 the pressure and admittance signals seem to indicate that wires within the catheter are breaking, causing "noisy" random outputs.

5.2.4 Rat 6, Implant S5

The experiment for implant S5 lasted 20 days. Pressure and volume signals were valid out to day 3, at which point the signals indicate connections to the catheter were compromised. The subject was sacrificed at the three week ultrasound measurement when it was discovered that the catheter had perforated the septum of the heart and moved from the left ventricle to the right ventricle. The battery on this implant lasted only 8 days on its initial charge (possibly due to contacting charging leads), and was recharged on day 17. This accounts for the lapse in data collection.

5.2.5 Rat 7, Implant S1

The Rat 7 experiment had a similar outcome to the Rat 5 experiment, though on a shorter time scale. Pressure signals were continuously valid out to day 3, and intermittent after that point until day 5. The admittance signals suggest that late in day 1 the catheter became ill-positioned (possibly lodged in the papillary muscles as in Rat 5), causing the muscle signal to dominate the measured bulk admittance of the heart. Interestingly, after this event, there is one more valid epoch in day 1 and one in day 2, suggesting that the catheter became dislodged for short periods. On day 5 the pressure and admittance signals clearly show that there is a bad connection.

5.2.6 Rat 8, Implant S8

Experiment 8 did not produce viable PV data because the measured susceptance (*ImY* component) was negative both before and after phase calibration. There may have been a physical defect in the circuit that caused the resistor/capacitor/saline calibration to become invalid.

5.2.7 Failure Analysis Summary

These 6 implant studies suggest that there is still room to improve the robustness of the implant in-vivo. The failure point for experiments 3 and 4 was short battery life and an inability to charge the battery. With an improved battery charging interface, experiments 5 and 7 failed to produce valid PV loops after a few days due to poor positioning of the catheter in the ventricle, despite correct functionality of the circuit. Degradation and eventual loss of signal was observed in experiments 5, 6, and 7, and is thought to be caused by kinking or breaking of wires within the catheter.

5.2.8 Animal Health

One of the primary design objectives of this project was to improve upon previous designs by making the implant circuitry smaller and lighter so as not to be a hindrance to the animal. Average implant weight was 8g and average volume was 5mL. Observation of these 6 rats suggests that the bulk of the implant between the shoulder blades does not cause apparent weakening of the animal. However, ultrasound data indicates a trend toward heart enlargement over time (Table 5).

Table 5: Heart Volume Over Time From 2D Echo

Group	n	LVEDV	LVESV	LV EF%
Pre implant	6.00	456.51±120.08	128.49±40.99	71.15±9.37
post implant	6.00	457.43±177.88	137.84±49.92	68.60±10.97
week 1	6.00	548±162.69	201.82±92.25	64.01±8.38
week 2	6.00	657.36±181.00	269.14±98.46	59.15±7.11
week 3	5.00	700.34±117.65	276.50±86.81	59.90±12.37

5.3 VOLUME OVER TIME

Experiment 4 provided valid admittance data for the longest period of time, 10 days. As previously mentioned, excess leakage current during sleep mode limited the lifetime of the implant to about 1 day per charge, so data was only collected on 4 of the 10 days (for each time the battery was recharged). The traces for G_b and G_m on these four days are given in Figure 36. Individual epochs are demarcated by shaded/un-shaded regions. Data was collected every 2 hours for this implant.

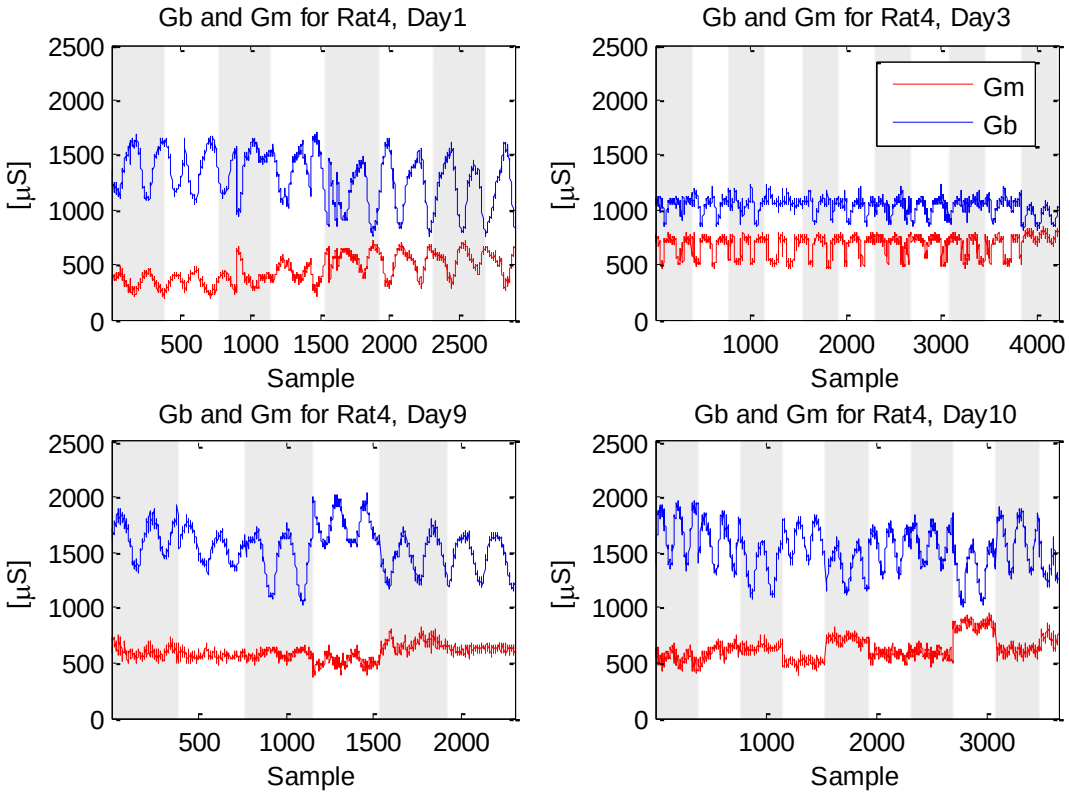

Figure 36: Blood (blue) and Muscle (red) Conductance Traces Over 10 Days

These plots show changes in average blood and muscle conductances (G_m and G_b) both on shorter (epoch to epoch, 2 hour) and longer (day to day) time scales. These deviations result in marked changes in calculated volume over time, as shown in Figure 37.

PV loops from implantation day were used to choose an appropriate sigma-epsilon for the remaining data set (Figure 38, left pane). Ultrasound verified that the catheter was in a centered position (Figure 38, right pane). Possible sources of error

include changes in blood conductivity over time (examined in Section 5.3.1) and changes in catheter position (examined in Section 5.3.2).

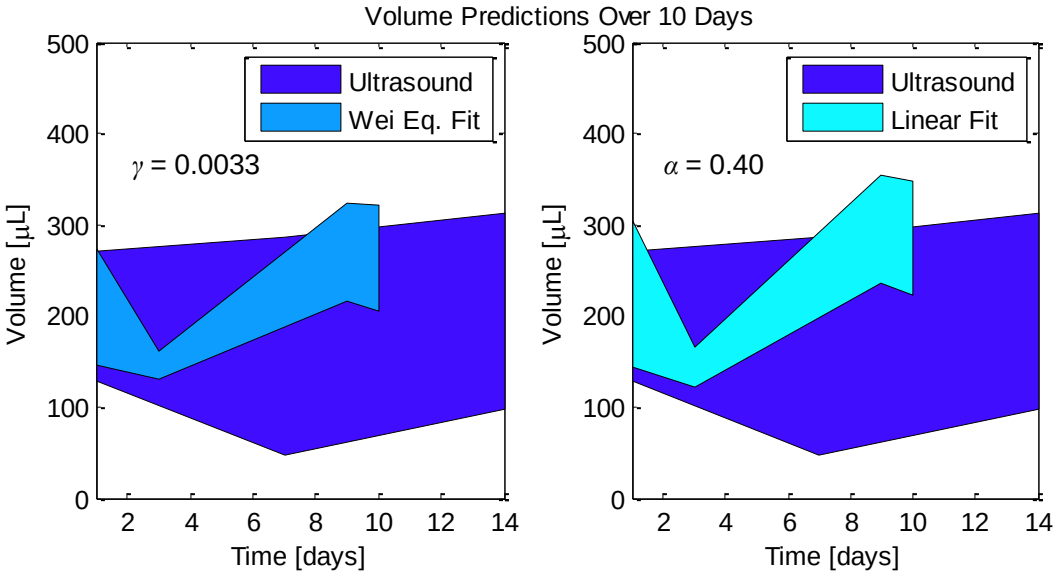

Figure 37: Volume Measured by Ultrasound and Experimental Implant

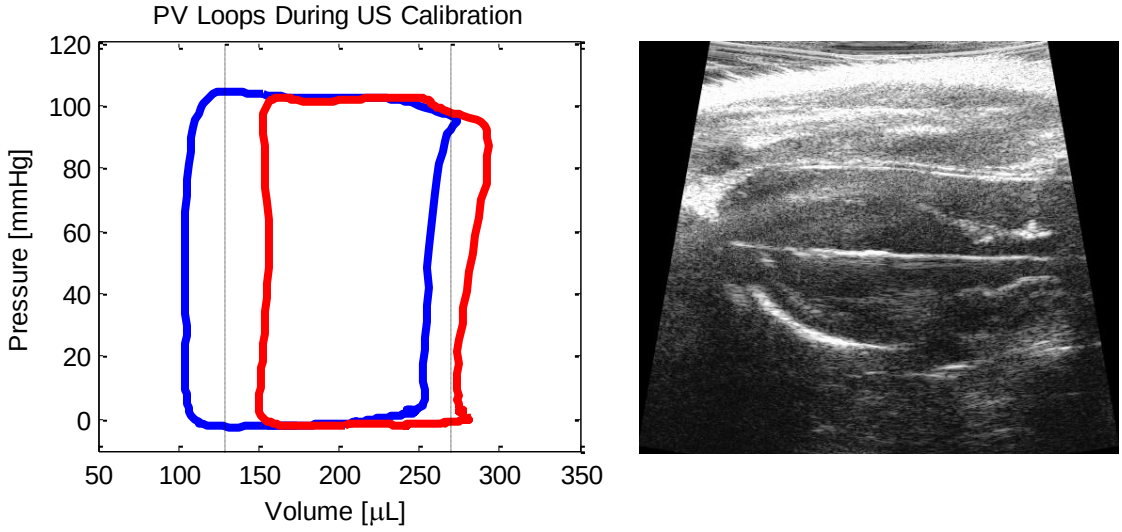

Figure 38: Catheter Position and PV Loops During Implantation for Rat 4

In Figure 37, calculated volume from days 1, 3, 9, and 10 is superimposed over the ultrasound measured volume. Two methods of G_b to volume conversion are shown. In the left pane, volume was calculated using Wei's equation (8). In the right pane, volume was calculated using Baan's linear conductance to volume equation (7). For both the linear (Baan) and non-linear (Wei) volume calculations, raw PY data from the implant was calibrated as explained in Chapter 4.

5.3.1 Changes in Blood Resistivity Over Time

Blood resistivity is assumed to be constant for the analysis described in this report. However, there is evidence to suggest that this may not be a valid assumption. Uemura's rat implant experiments in 2004 used a catheter that included a secondary tetrapolar electrode set to measure blood resistivity in the ambulatory rat. Over 6 days, ρ_{blood} was observed to span the range 175-275 Ω-cm [9]. A ρ_{blood} value of 167 Ω-cm measured in previous experiments was used for all analyses presented in this report. Changes in blood resistivity over time result in volume errors since calculated volume is nearly linearly proportional to ρ_{blood} (see equations (7) and (9)).

5.3.2 Catheter Positioning Error

An experiment was conducted to investigate the sensitivity of the admittance measurements to deviations in catheter position. Research has shown that the flesh of winter squash may be used as a reasonable analogy to human tissue, having a sigma-epsilon ratio around 0.31×10^6 [16]. A 1/2" hole was drilled in the flesh of an acorn squash to simulate the blood volume and filled with 2 mL of 3000 μS/cm saline solution.

To determine sensitivity to catheter position, a secured caliper was used to simultaneously displace the catheter from the centered position, and measure the displacement in mils (1/1000th inch). A schematic of the measurement is given in Figure 39.

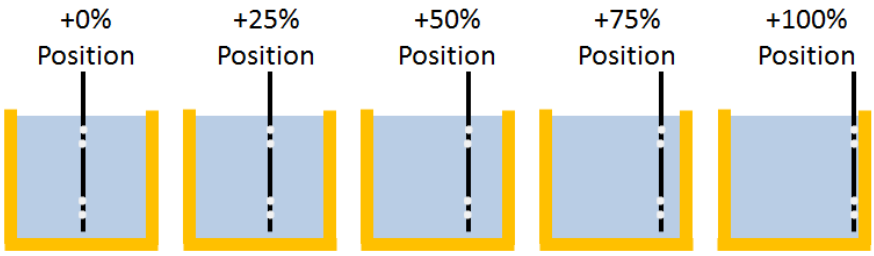

Figure 39: Squash Cuvette Catheter Position Experiment

Since a static cuvette has no stroke volume, the linear volume conversion equation (7 **)** was used to determine calculated volume. The result of the experiment (n=3 trials) is given in Figure 40. The volume measured at positions representing 50% displacement and greater from the center show marked error in measured volume. Note that the magnitudes of the real and imaginary components are comparable to those measured in the rat, and that *ReY* decreases and *ImY* increases as the catheter moves closer to the cuvette wall as expected.

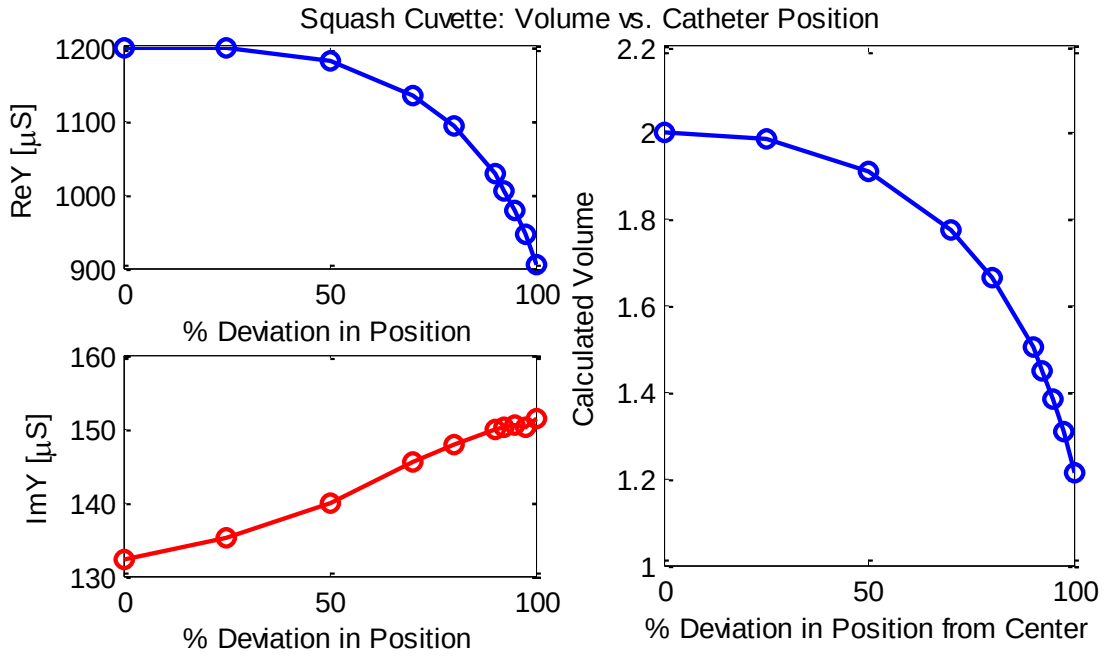

Figure 40: Volume vs. Catheter Position

With this, consider the volume traces measured on days 9 and 10 in Rat 4. These traces were chosen for analysis because they are the most representative data collected for admittance after "long term" implantation, when the physiological state and implant position are assumed to have stabilized. Figure 41 gives the *ReY*, *ImY*, and calculated volume traces on these days. In these traces, the average value of *ImY* is fairly dynamic across epochs. This could either indicate that catheter position is changing, or true volume is changing. Relative positive changes in *ImY* and negative changes in *ReY* as observed in the squash cuvette for catheter displacement towards the wall are also seen in Rat 4, especially in epochs like day 10, epoch 6. This effect causes the calculated total volume and SV to appear low. From a physiological perspective, it is unlikely that the

total volume of the heart or the blood conductivity has changed enough in 2 hours to cause calculated volume to change by 100% as suggested by paired epochs like day 10, epochs 4 and 5. Therefore, we may conclude that catheter displacement is causing significant volume error.

Note that for this analysis, ultrasound data from Rat 4, day 7 was used to recalibrate this data such that the epoch with the lowest average *ImY* and highest average *ReY* produced correct values for EDV and ESV. In this recalibration, sigma-epsilon ratio was adjusted from 1.04×10^6 to 1.35×10^6. As suggested by the squash cuvette experiment, this calibration epoch should represent measurements from a centered catheter.

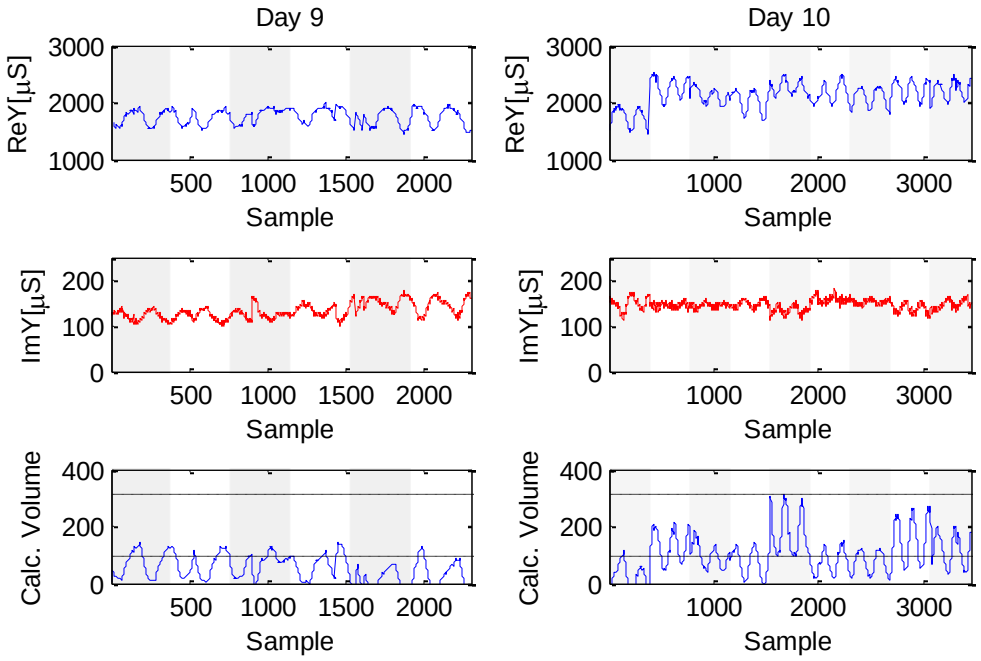

Figure 41: Volume on Days 9 and 10, Rat 4

5.3.3 Admittance Drift Due to Biological Wear

There has been some concern in the past about admittance drift over time due to tissue reaction to the catheter. It was hypothesized that fibrotic growth on the source/measurement electrodes of the catheter may increase the electrode impedance and reduce the current density in the blood pool, thereby changing the admittance to volume calibration. To investigate tissue effects on the catheter over time, an inactive catheter was left in the heart after the failure of Implant 0 (see Figure 34). The rat lived for 5 months with the inactive catheter. The heart was dissected *post-mortem* to examine the catheter. No fibrotic growth was observed on the catheter as shown in Figure 42. This one experiment does not comprise a representative set, but suggests that the Scisense catheter material may be appropriate for long term implantation. At the time of writing, two more rats with inactive catheters are under observation.

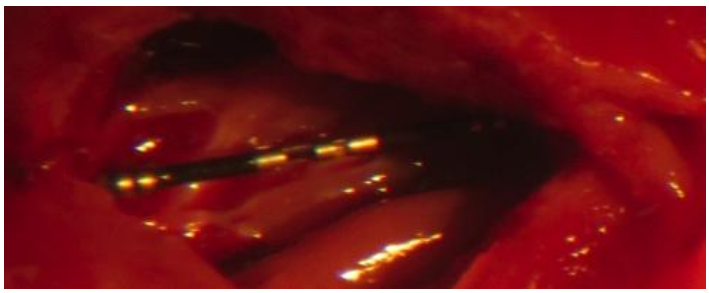

Figure 42: Catheter After 5 Months in the Heart

5.4 Pressure Over Time

Drift in absolute pressure is a concern for a PV monitoring device as changes in end diastolic pressure (EDV) may indicate pathology. In an optimal use case, the lumen

of the Scisense PV catheter should be vented to atmospheric pressure so that the measured pressure is atmosphere relative. However, venting to the atmosphere is not possible in a fully implanted system, and the lumen of the catheter is sealed during fabrication of the implant. Since LV pressure changes with atmospheric pressure and the catheter reference pressure (lumen pressure) does not, barometric pressure should be monitored during data collection.

Experiment 5 (implant S4) provided 11 continuous days of pressure measurements, collected at a 1 epoch/hour sampling rate. The minimums of this pressure trace (Figure 43) were recorded and assumed to represent LV pressure at end diastole. Figure 44 shows the EDP drift over 11 days. Two additional traces are superimposed for comparison. Deviation from the mean barometric pressure in San Antonio, TX (reported from [17]) over the 11 days of data collection is shown in red. Pressure drift from a sealed catheter submerged in an open container of saline over a different set of 11 consecutive days in Austin, TX is shown in green. The average EDP reported from the implant was 0±6 mmHg, the average deviation in barometric pressure in San Antonio over the same 11 days was 0.0±1.8 mmHg, and the standard deviation in pressure from the sealed catheter submerged in saline was 2.9 mmHg. The standard deviation in measured EDP is more than twice the standard deviation in barometric pressure or pressure drift in the sealed catheter. This excess deviation in EDP could be the result of physiological variation, or physical forces (bending) on the sealed catheter lumen.

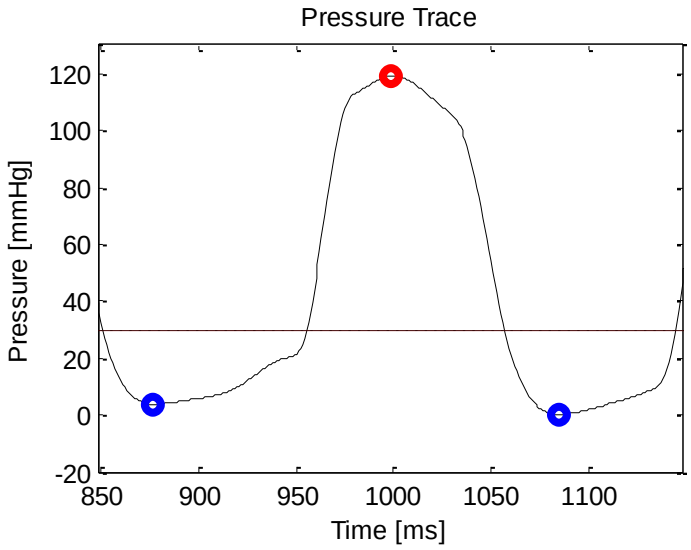

Figure 43: Location of End Diastolic Pressure Points (blue)

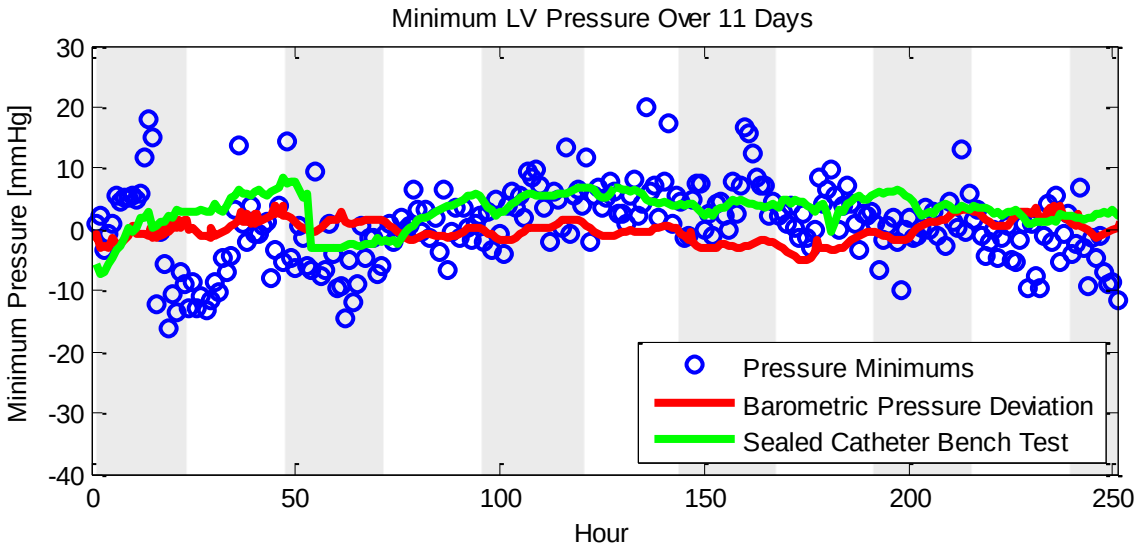

Figure 44: End Diastolic Pressure Drift

Chapter 6: Conclusion

6.1 Implant Performance

In accordance with the design objectives, an 8g, 5cm^3 device has been created that is capable of measuring PV data from the ambulatory rat heart for >2 months. Acute functionality of the experimental implant has been verified in six *in-vivo* rat studies. In five of the six studies, ambulatory PV loops were recorded on implantation day. In the sixth study (experiment 8), reasonable raw impedance data was available but could not be converted to volume due to inaccurate calibration data. The typical timeframe for which valid pressure and volume data was transmitted was 2-3 days. One implant (experiment 5) transmitted valid pressure data out to day 11, another implant (experiment 4) transmitted valid volume data out to day 10. Bench testing data indicate that the implant is able to transmit 43 times per day for 2 months. Later experiments (6, 7, and 8) indicate that the limiting factor for implant lifetime at present is the breakage of wires within the catheter. Beyond this, changes in catheter position and blood resistivity over time affect the accuracy of calculated volume. Long term health of the animal is also a concern for future experiments. Observation indicates that the bulk of the implant between the shoulder blades is not a hindrance to the animal, but the continual presence of the catheter in the aortic valve appears to cause thickening of the valve flaps, subsequent aortic insufficiency, and enlargement of the heart over time.

6.2 FUTURE DIRECTIONS

The implant circuit may find future uses with similar transducers. The interface used to connect the Scisense PV catheter to the circuit it readily adaptable to new probes, and different catheters/electrode configurations may prove more robust *in-vivo*. Changing a few components in the admittance measurement circuit would allow for volume measurements to be made in larger animals as well.

Some care should be given to the effects of catheter parasitic elements and electrode interface impedances in future work. Calibration of the system could be improved by the development of a better circuit model for the probe/instrument system that takes into account solution conductivity-dependent electrode impedance.

Appendix A: Implant Assembly Procedure

Tools:

- Tweezers
- Scalpel
- Small board mount
- Soldering iron and solder
- Bending mold

Materials

- Kapton tape
- Electrical tape
- General purpose superglue
- Potting compound: 3M DP-270 Epoxy Potting Compound
- Silicone: Dow Corning 734 Flowable Sealant

Procedure:

1. Cut a 20.5 cm length of catheter.
2. Tape the catheter around the bending mold using Kapton tape as shown in Figure 1. Leave 1 cm of catheter after the downward slope on the cut side. Some of this length will be stripped away to expose the catheter wires.
3. Set the heatgun temperature to 167 C and the airflow to 3.
4. Use a test piece of catheter (the extra cut from the original length) to get a feel for how close you need hold the heat gun to the catheter to cause it to bend. This distance should be about one inch.
5. Heat the catheter on the mold. Make swift passes about an inch away from the catheter. Avoid heating any area for too long.
6. Under the microscope, use a scalpel to strip about ¼ inch from the cut end of the catheter. About ¼ inch back from the cut end, slide the scalpel into the catheter and up to the cut end. See Figure 2. You may want to test the scalpel on the test catheter material used before. If it is not sharp enough, get a new blade!
7. There should be 7 wires inside the catheter. Once the wires are exposed, gently move them aside and cut off the excess empty catheter. At this point, the catheter should appear as shown in Figure 3.
8. Set the circuit in the small circuit holder with the analog side up (side without MCU). Using superglue, mount the catheter to the circuit as shown in Figure 4. Be careful not to get superglue too close to the catheter pads or on the catheter wires. Hold the catheter in place with tweezers until the glue sets.

9. Gently tape the sensor end of the catheter down to the table using Kapton tape so that you will be able to probe the electrodes with the voltmeter.
10. Find the red wire. Using tweezers, guide it into the R1 hole and solder it down.
11. For each other wire:
    a. Separate the wire from the others.
    b. Tin the end of the wire with solder (about 1-2 mm at the end).
    c. Use one voltmeter probe to pin the tinned wire to the circuit and the other probe to test for continuity.
    d. If the wire is continuous with an electrode, guide it into the appropriate hole.
    e. If the wire is not connected to any of the electrode rings, it may be a pressure wire. Measure the resistance against the soldered R1 wire. If it is 2 kΩ, then the wire is R2. If it is 1 kΩ, then the wire is GND. Guide the wire into the appropriate hole.
12. Some tips on soldering the wires:
    a. To tin the wire, get a blob of solder on the iron away from the circuit and slide the catheter wire into it. If you touch solder to the iron around the catheter wires, steam and resin can cause the wires to stick together, or worse yet, contact!
    b. I solder the pressure wires to the board from the admittance side and the electrode wires from the MCU side of the circuit. Again, this prevents steam and resin from sticking the wires together.
13. After soldering the wires down, the circuit should appear as shown in Figure 5.
14. Once all wires are soldered, quickly test the catheter and circuit for functionality in saline and in the pressure chamber. Be very careful not to touch the soldered wires. Mechanical stress on the wires can cause them to break.
15. Mix up a small amount of potting compound. Gently cover the catheter wires with potting compound to stabilize them. I let the potting compound drip onto the wires to avoid pressing on the wires.
16. Obtain a functional battery. Cut the battery wires to be as long as the top of the battery and solder them to the circuit as shown in Figure 6.
17. Cover the remainder of the admittance side of the circuit with potting compound.
18. Before the potting compound dries, fold the battery against the circuit as shown in Figure 7.
19. Once the potting compound is dry, attach 2 wires to the battery terminals from the MCU side of the circuit. These wires will be used to charge the battery after implantation.
20. Cover the MCU side of the circuit in potting compound.

21. Once the potting compound has cured, carefully cover the circuit in a thin layer of electrical tape (Figure 8). Be cautious not to kink the catheter.
22. Apply a thin layer of silicone to the circuit but not the catheter.
23. Once the silicon on the circuit has cured, lay a piece of wax paper between the circuit and the catheter.
24. Apply silicone along the bent portion of the catheter. Don't worry about getting it perfect, the silicone can be trimmed later.
25. After the silicone on the catheter has cured, gently peel off the wax paper.

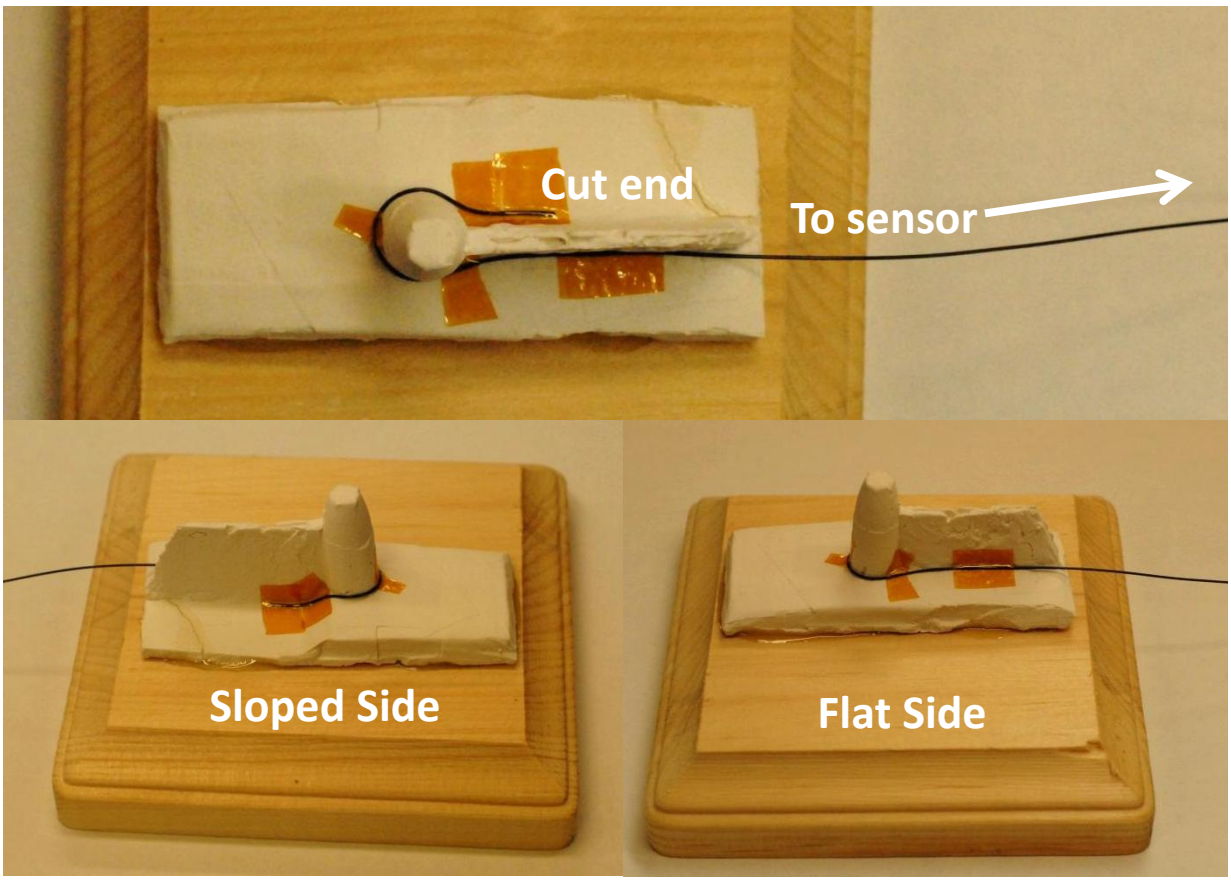

Figure 45: Catheter on Bending Mold

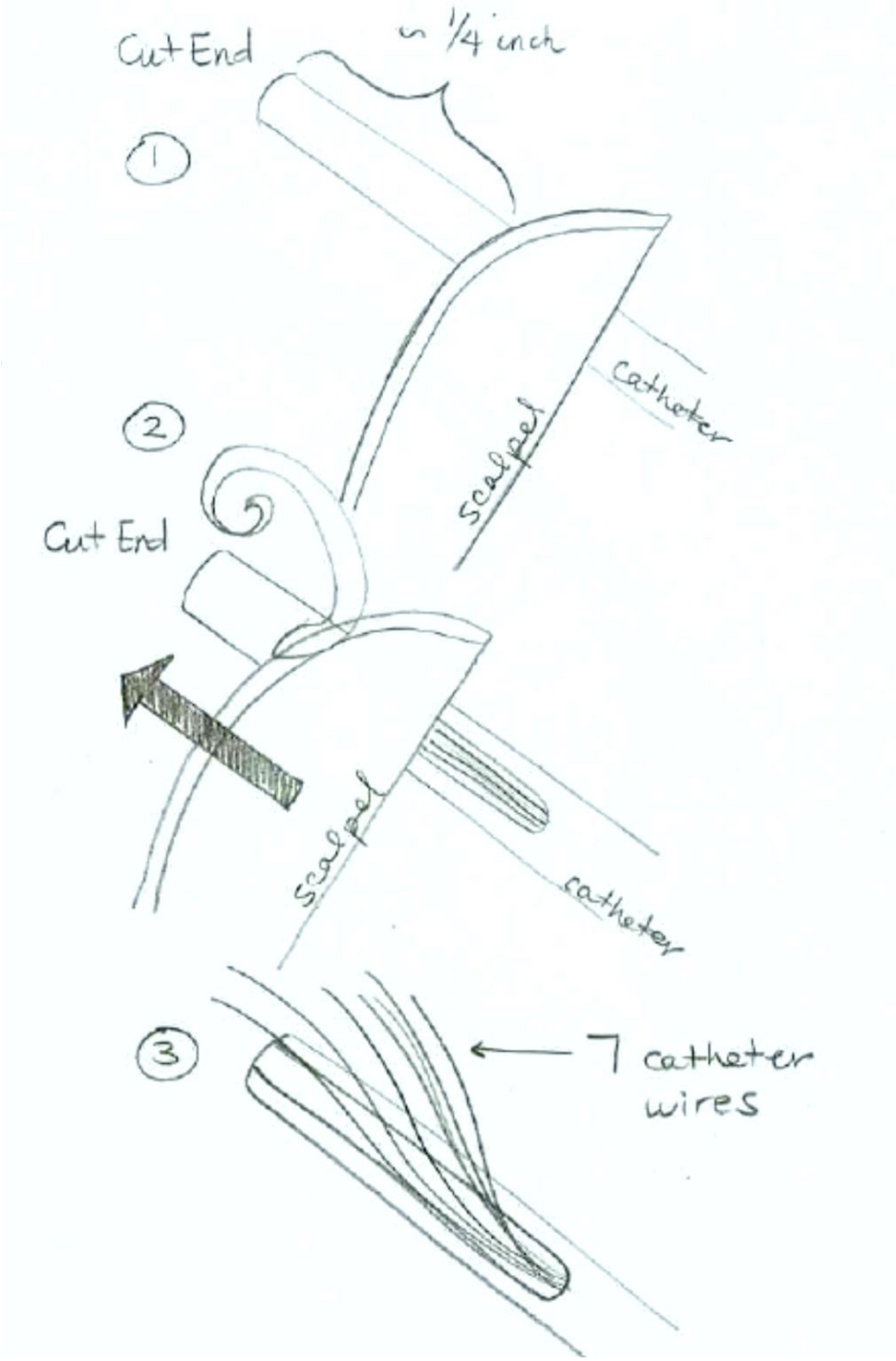

Figure 46: Exposing Catheter Wires

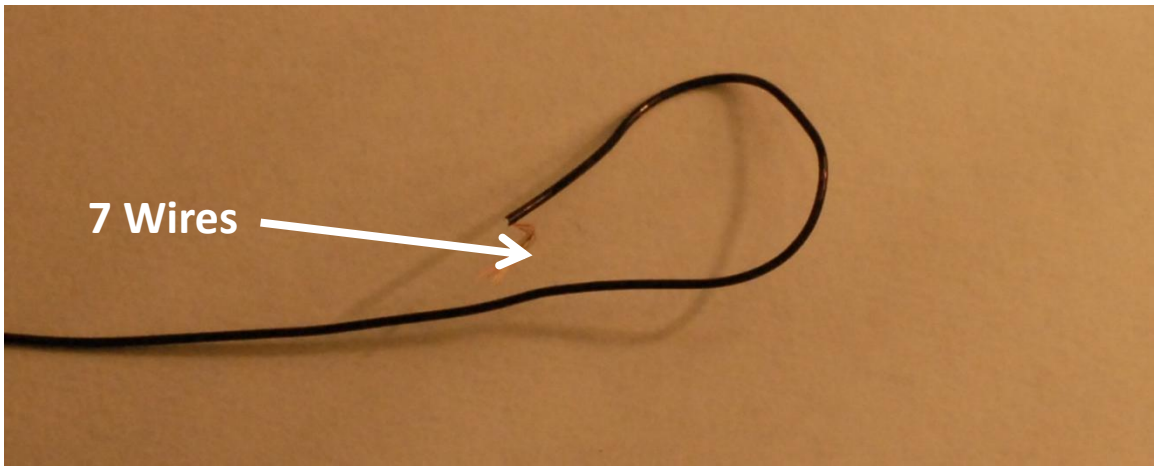

Figure 47: Formed Catheter With 7 Wires Exposed

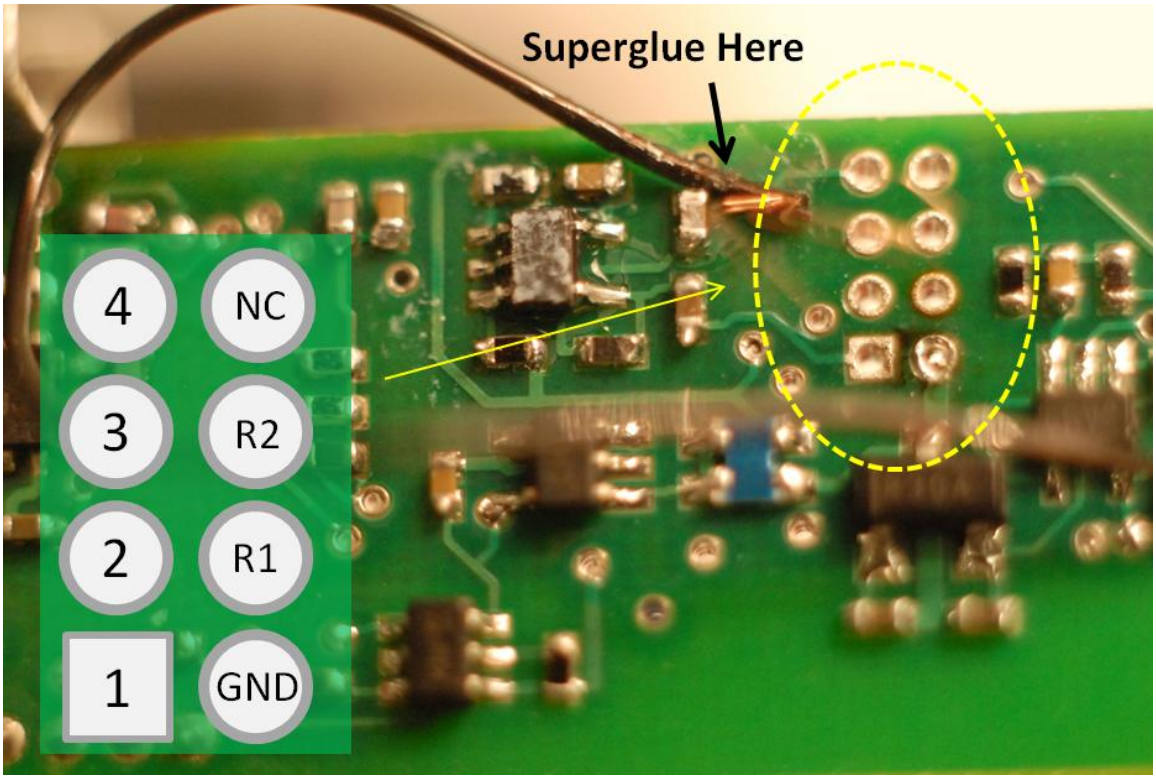

Figure 48: Mounting the Catheter to the Board

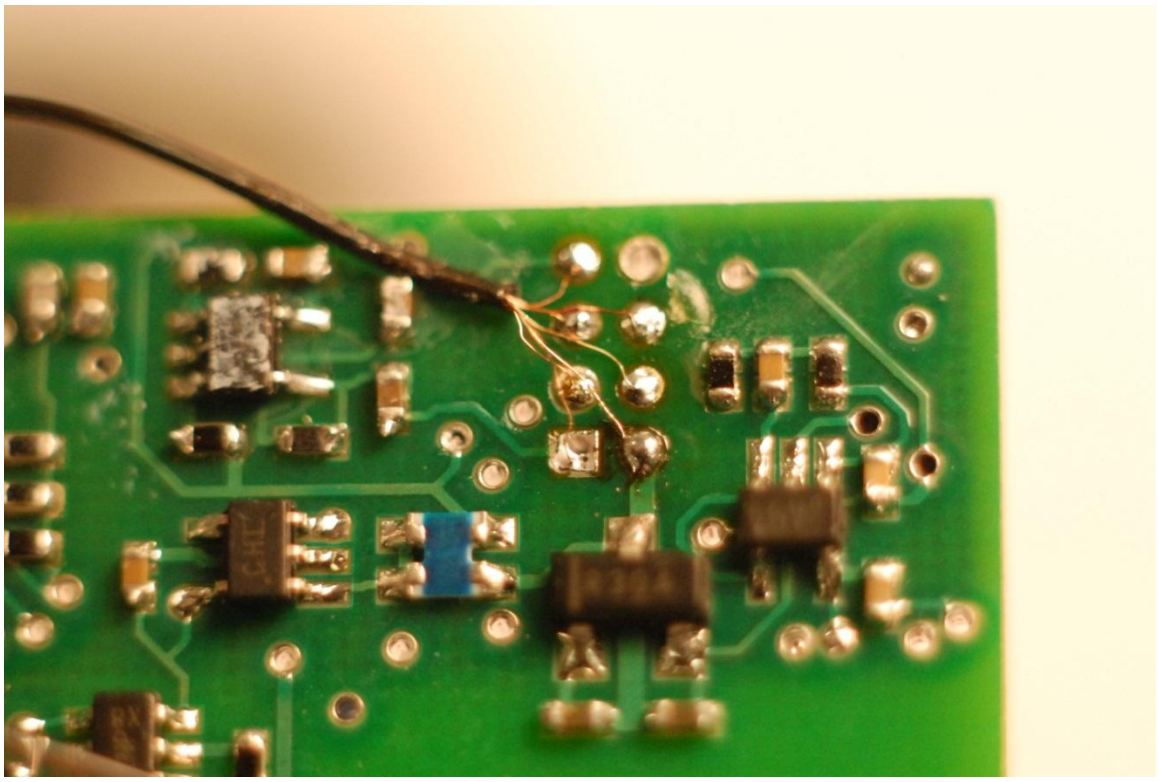

Figure 49: Catheter Wires Soldered to the Circuit

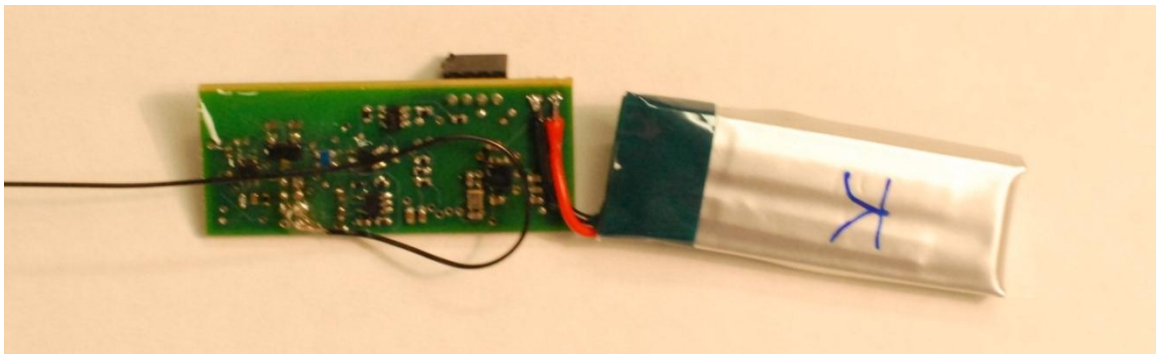

Figure 50: Potting Compound Applied and Battery Attached

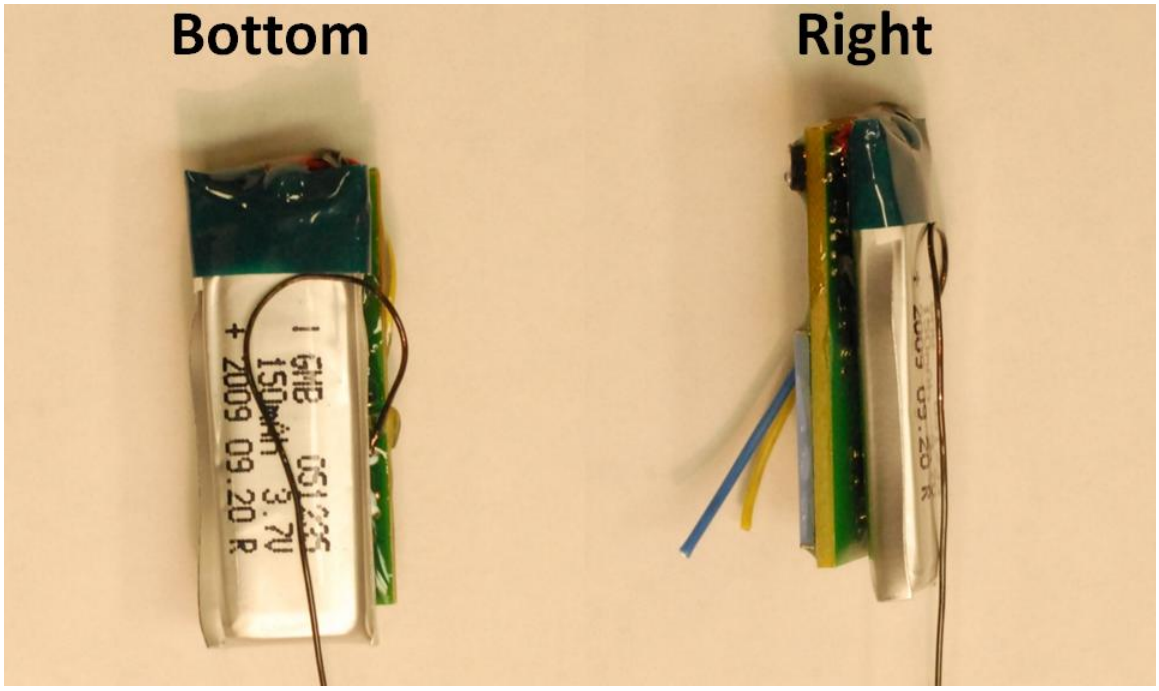

Figure 51: Battery Mounted Against the Circuit Using Potting Compound

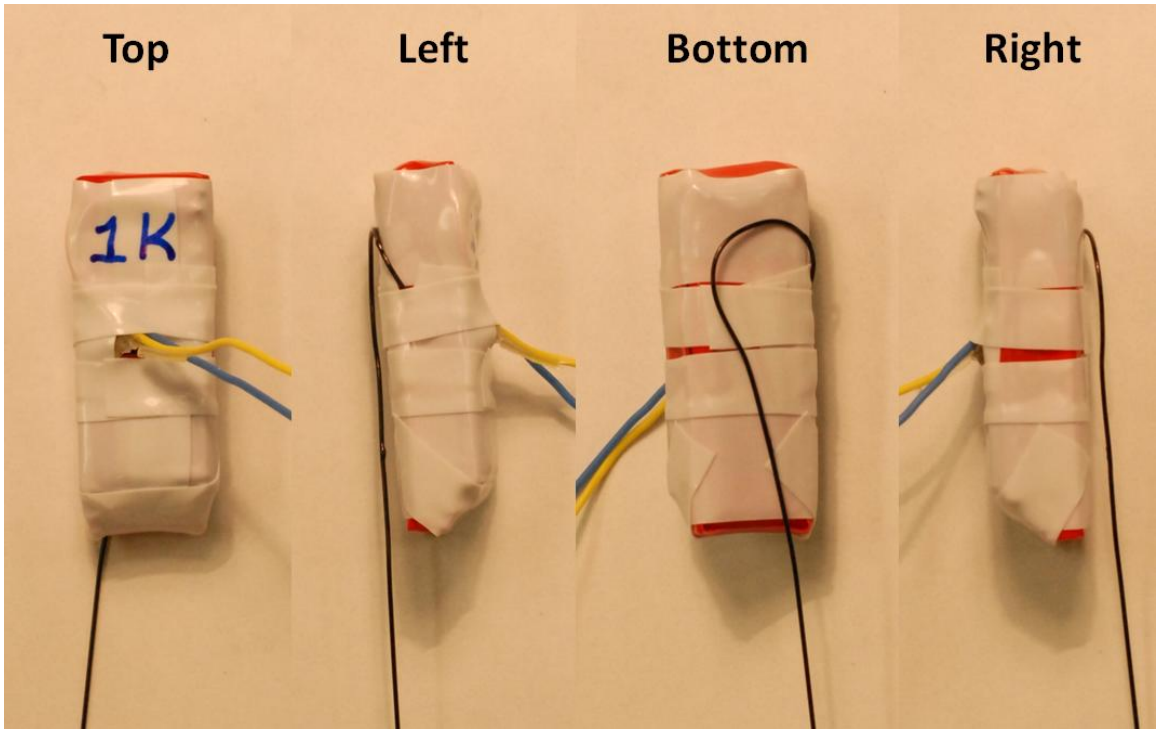

Figure 52: Circuit Covered in Electrical Tape

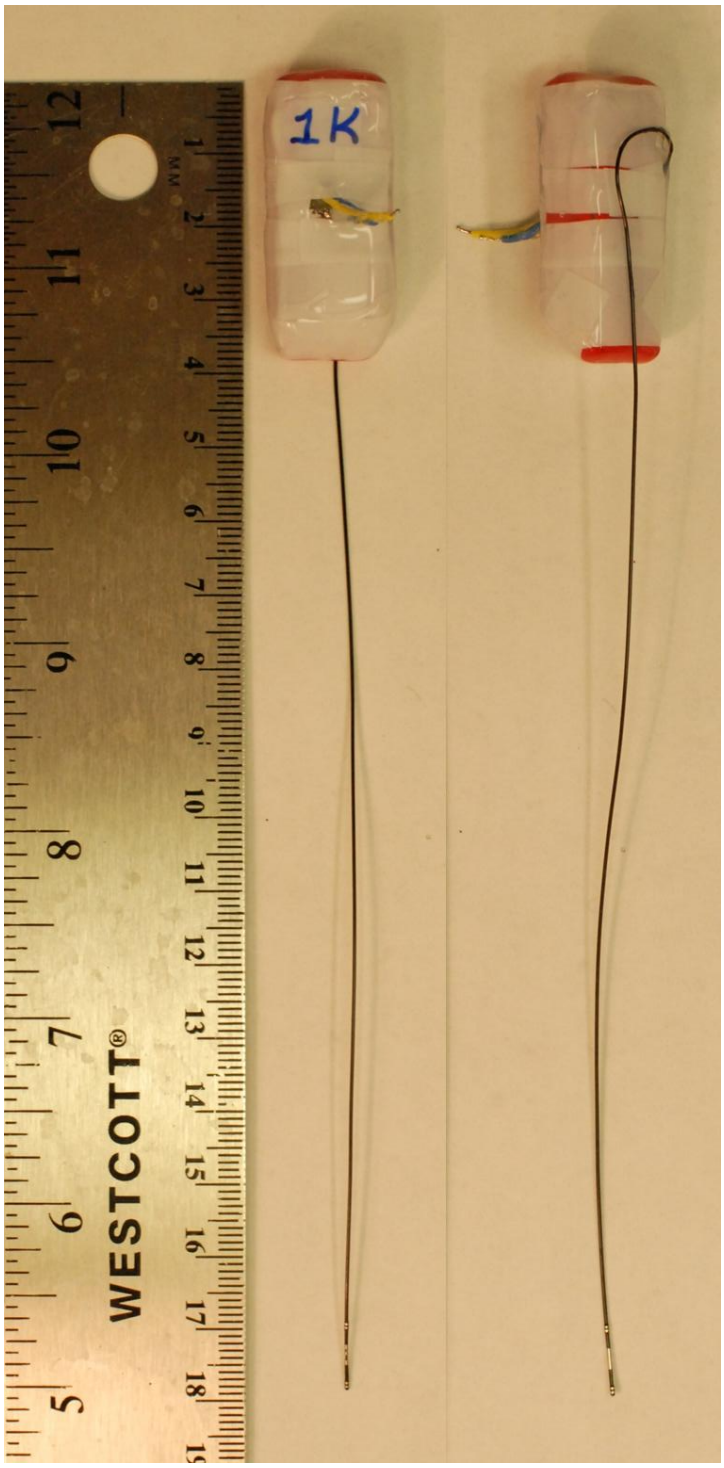

Figure 53: Completed Implant

Appendix B: Rat 3 Data Set Summary

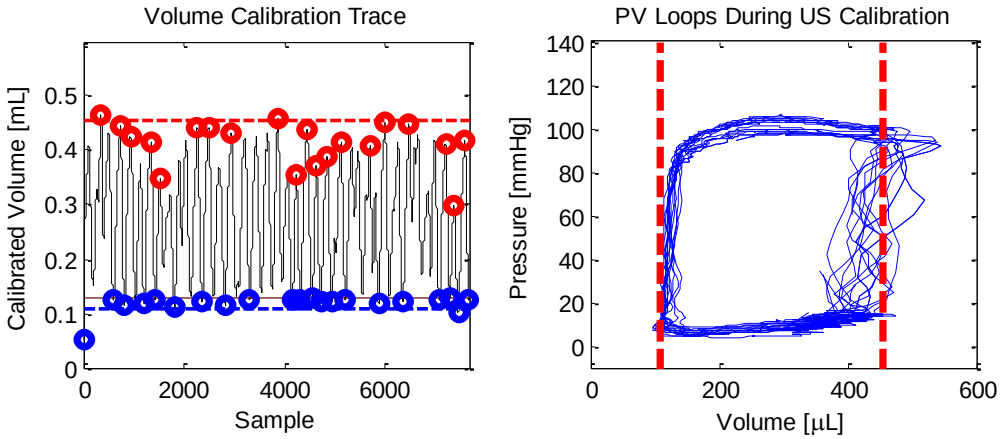

Figure 54: Volume Calibration, Rat 3

Table 6: Calibration Constants, Rat 3

Admittance Magnitude Gain	1.67
Pressure Gain	-0.40
Pressure Offset	-370

Appendix C: Rat 4 Data Set Summary

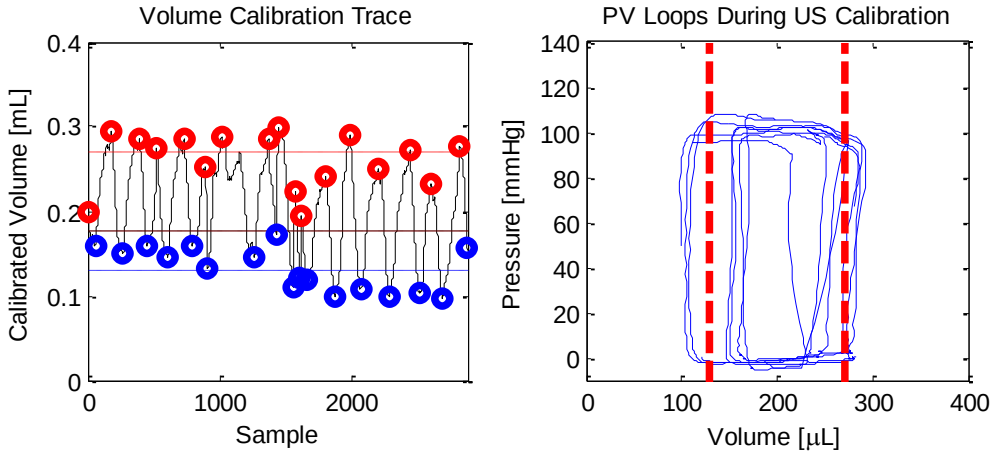

Figure 55: Volume Calibration, Rat 4

Table 7: Calibration Constants, Rat 4

Admittance Magnitude Gain	1.68
Pressure Gain	-0.43
Pressure Offset	-420

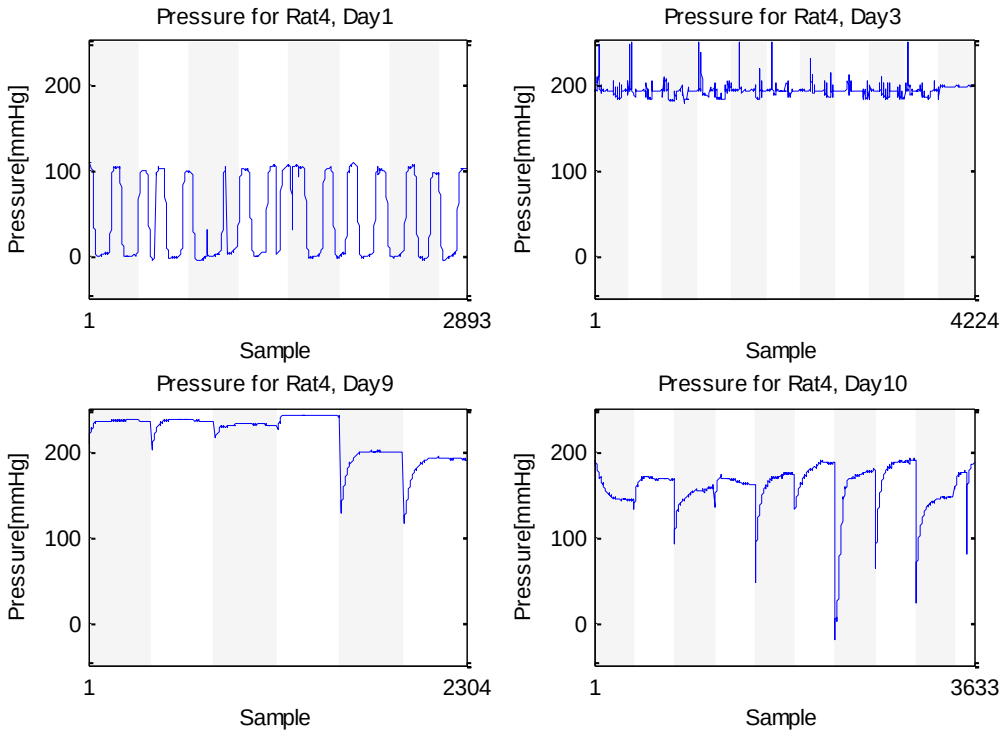

Figure 56: Pressure Data, Rat 4

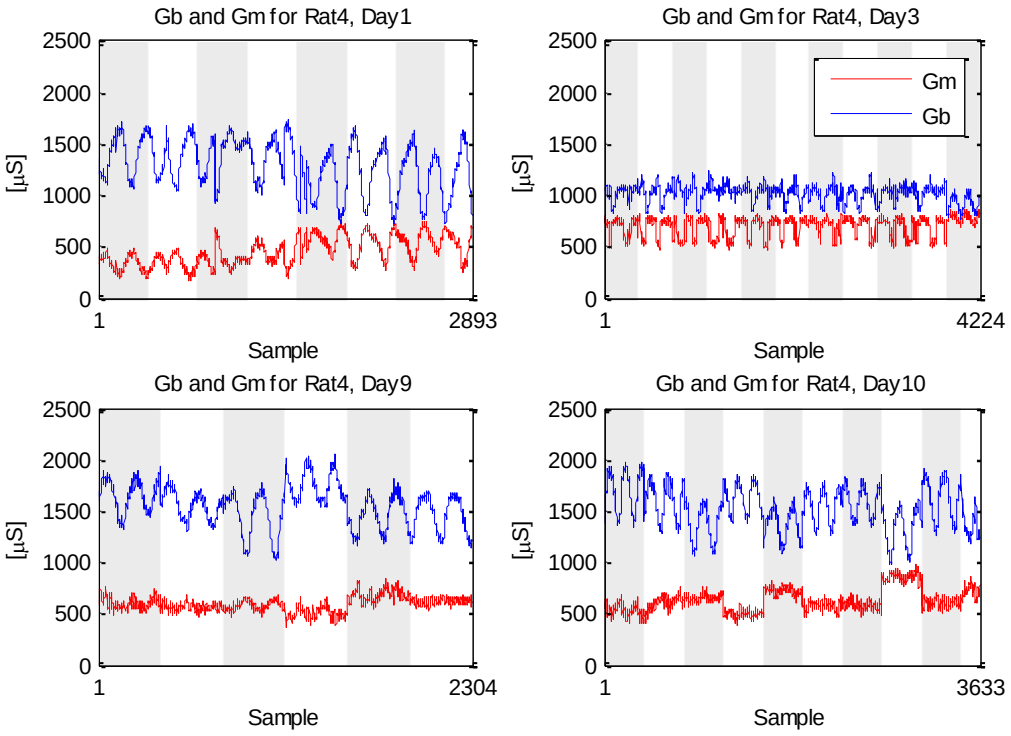

Figure 57: Admittance Data, Rat 3

Appendix D: Rat 5 Data Set Summary

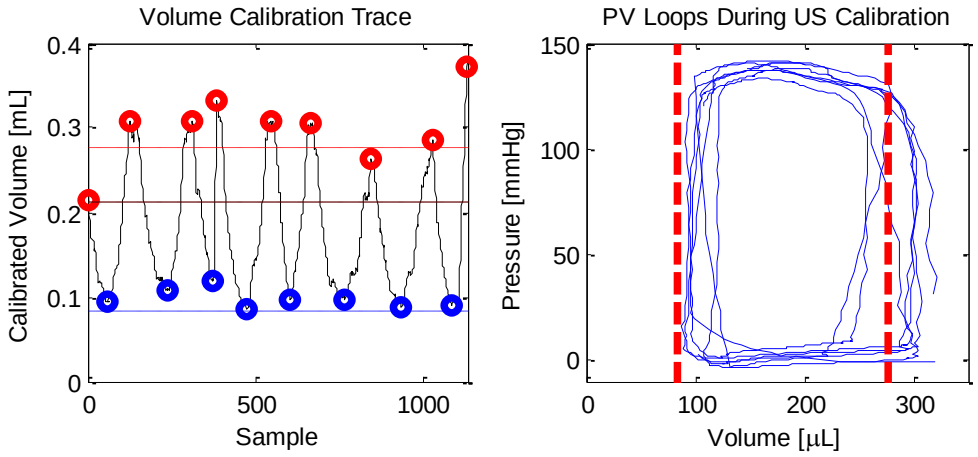

Figure 58: Volume Calibration, Rat 5

Table 8: Calibration Constants, Rat 5

Admittance Magnitude Gain	1.675
Pressure Gain	-0.43
Pressure Offset	-245

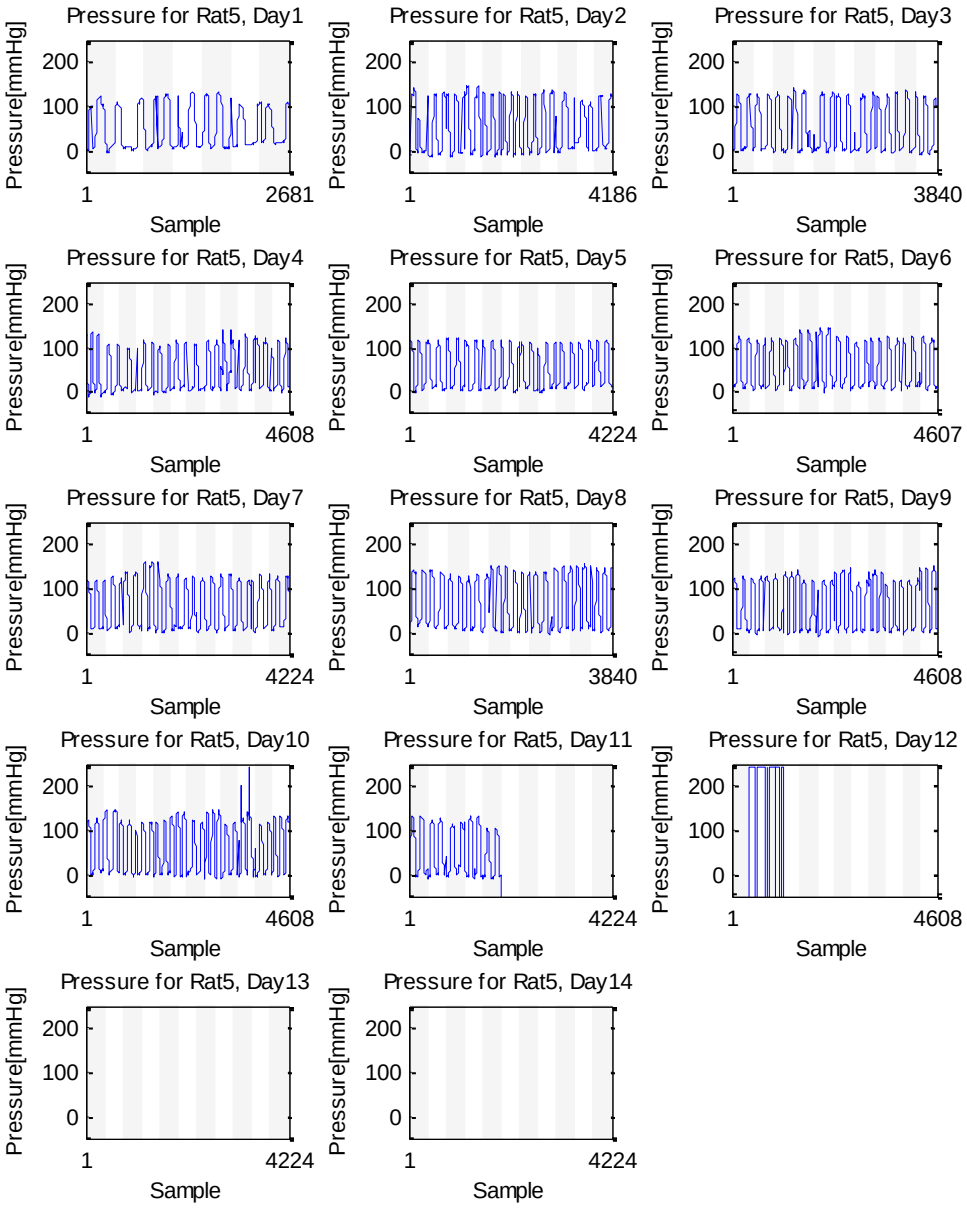

Figure 59: Pressure Data, Rat 5

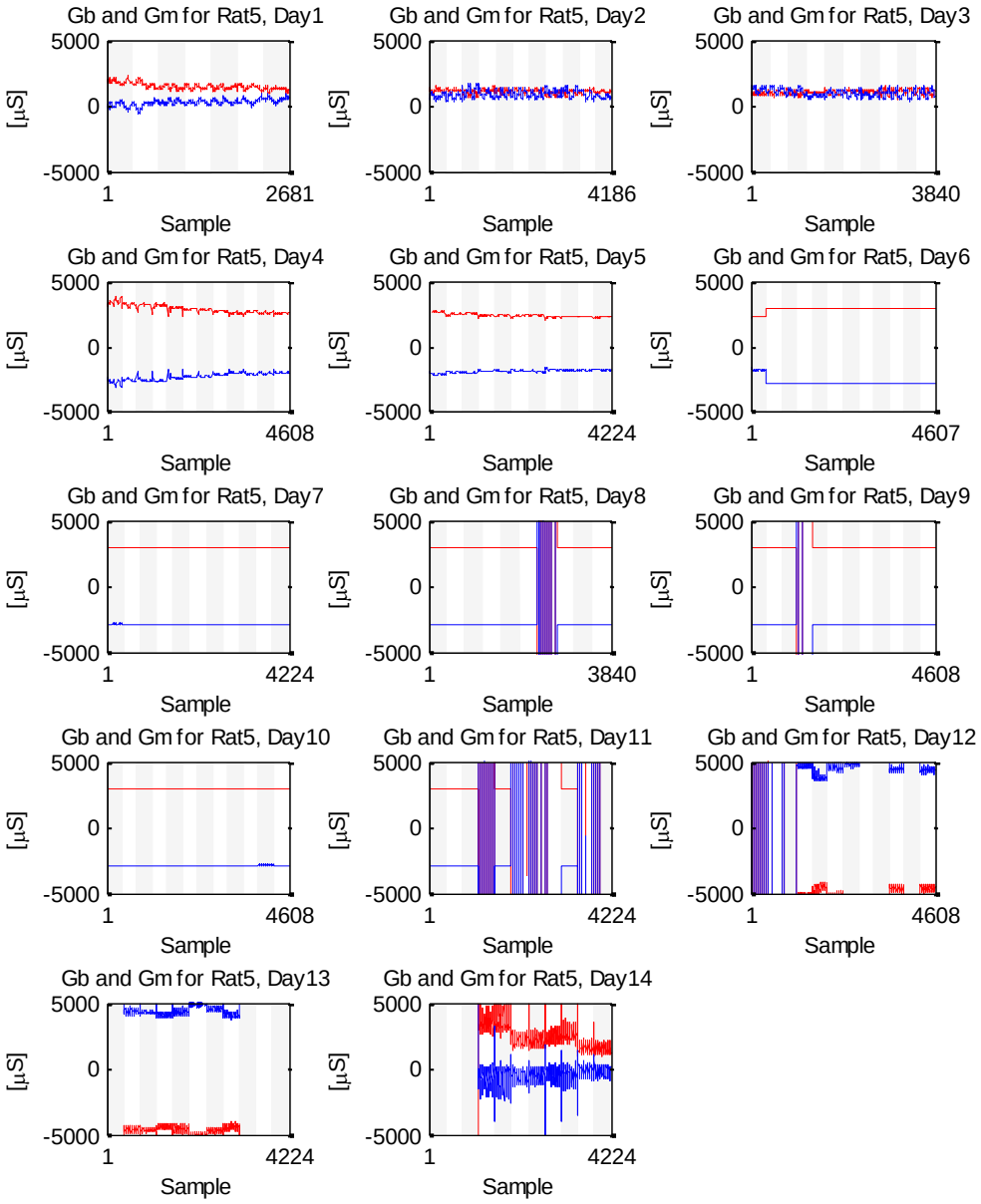

Figure 60: Volume Data, Rat 5

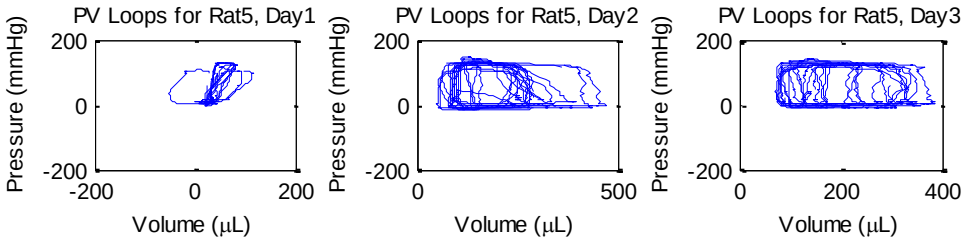

Figure 61: PV Data, Rat 5

Appendix E. Rat 6 Data Set Summary

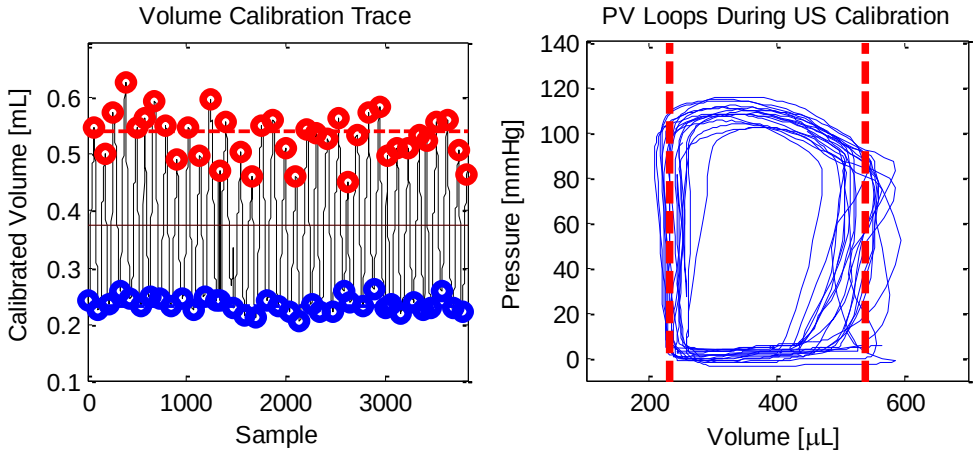

Figure 62: Volume Calibration, Rat 6

Table 9: Calibration Constants, Rat 6

Admittance Magnitude Gain	1.685
Pressure Gain	0.417
Pressure Offset	130

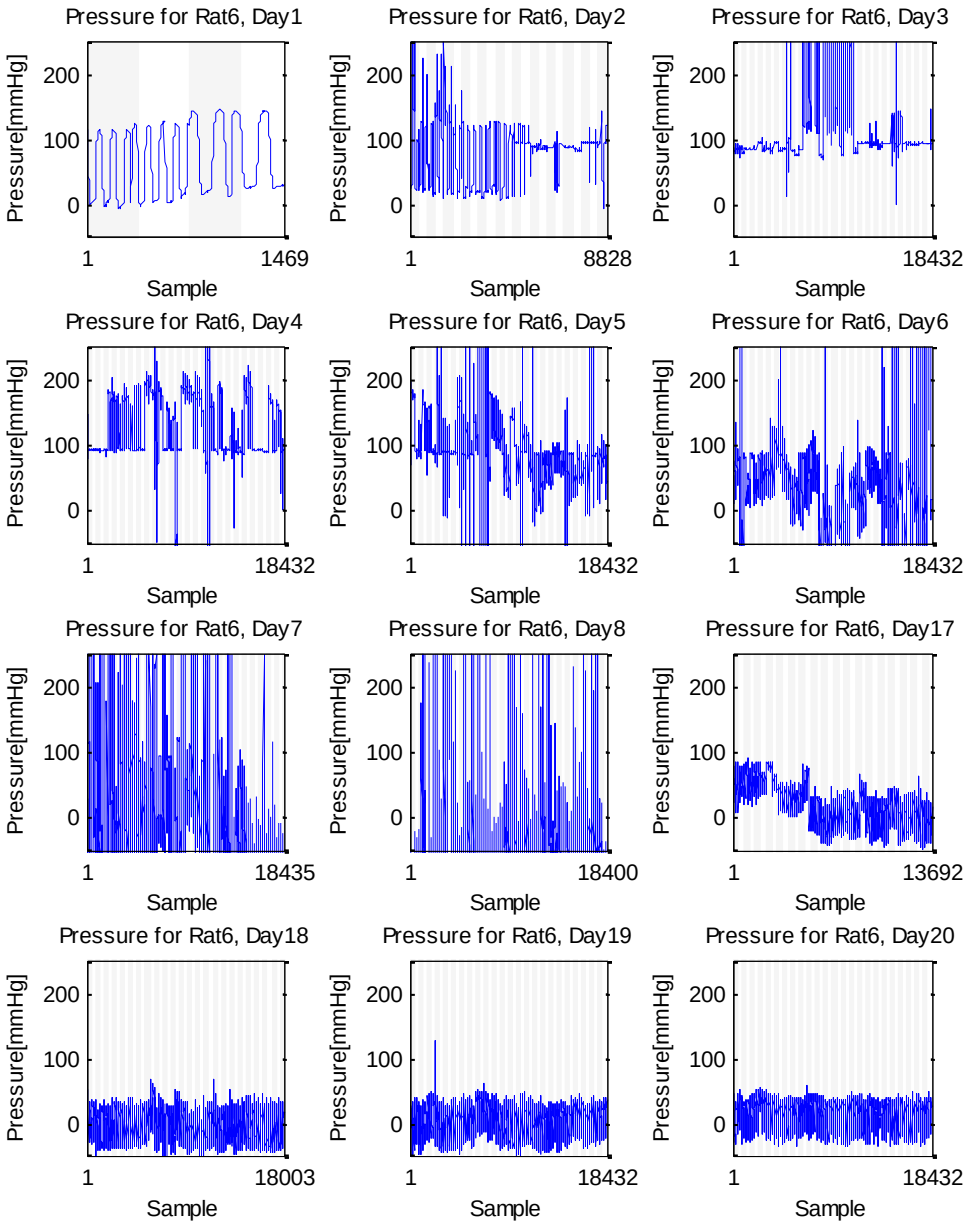

Figure 63: Pressure Data, Rat 6

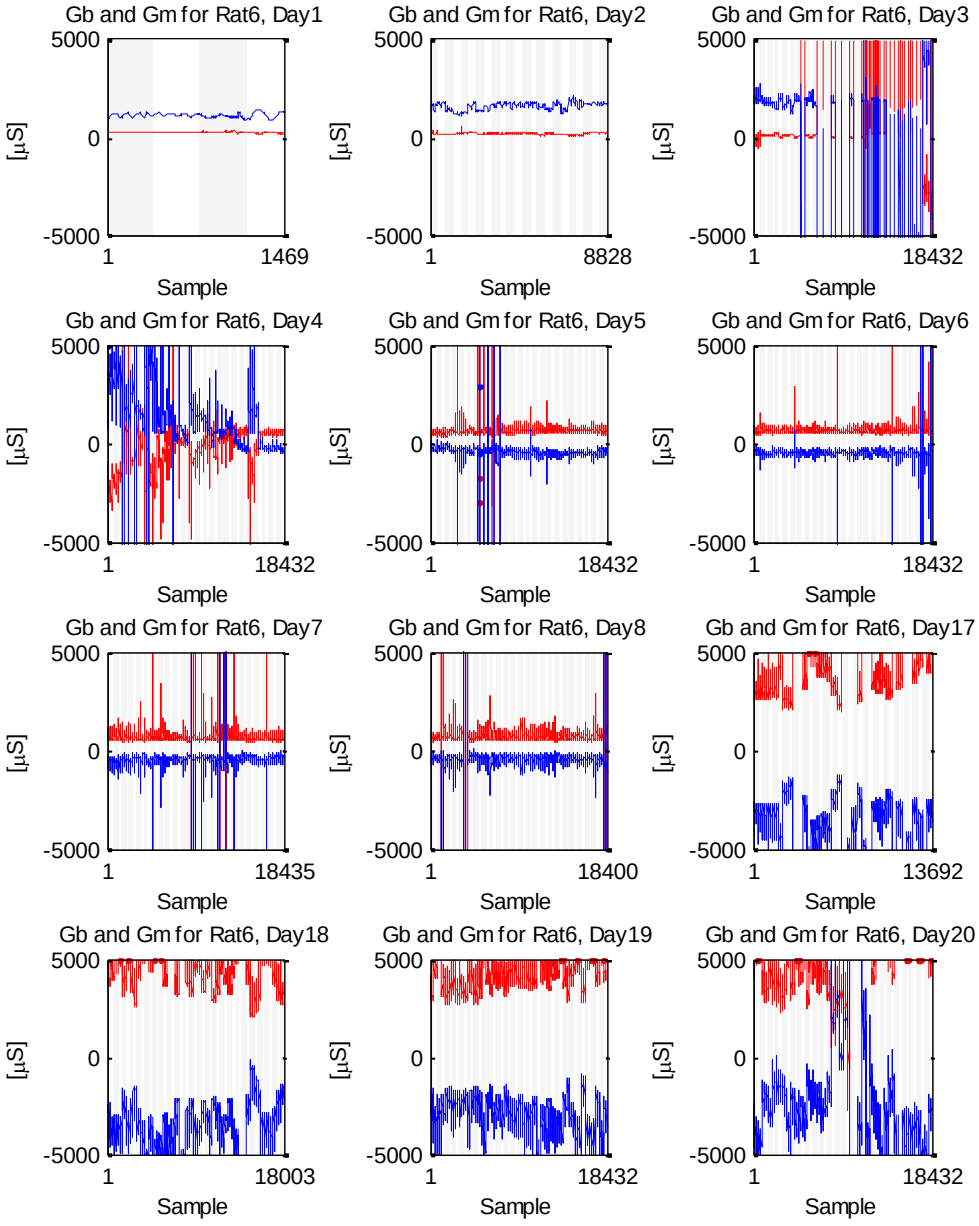

Figure 64: Volume Data, Rat 6

Appendix F. Rat 7 Data Set Summary

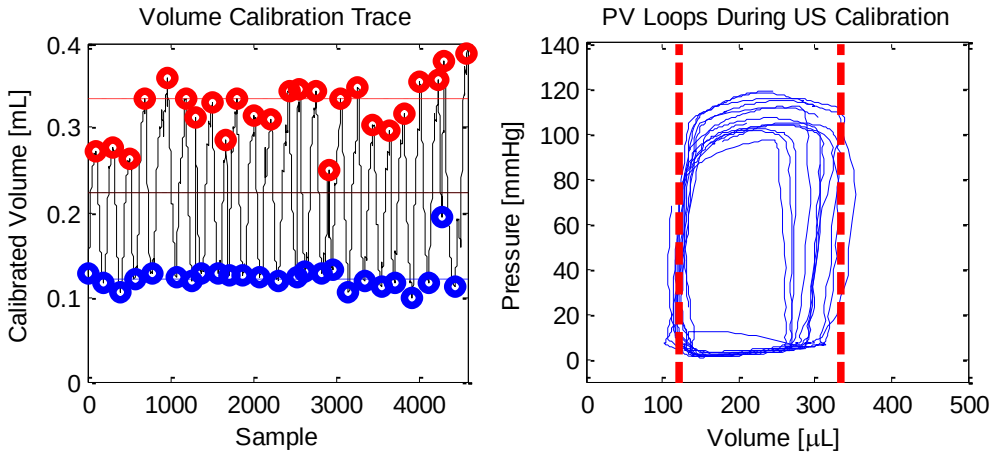

Figure 65: Volume Calibration, Rat 7

Table 10: Calibration Constants, Rat 7

Admittance Magnitude Gain	1.685
Pressure Gain	0.417
Pressure Offset	260

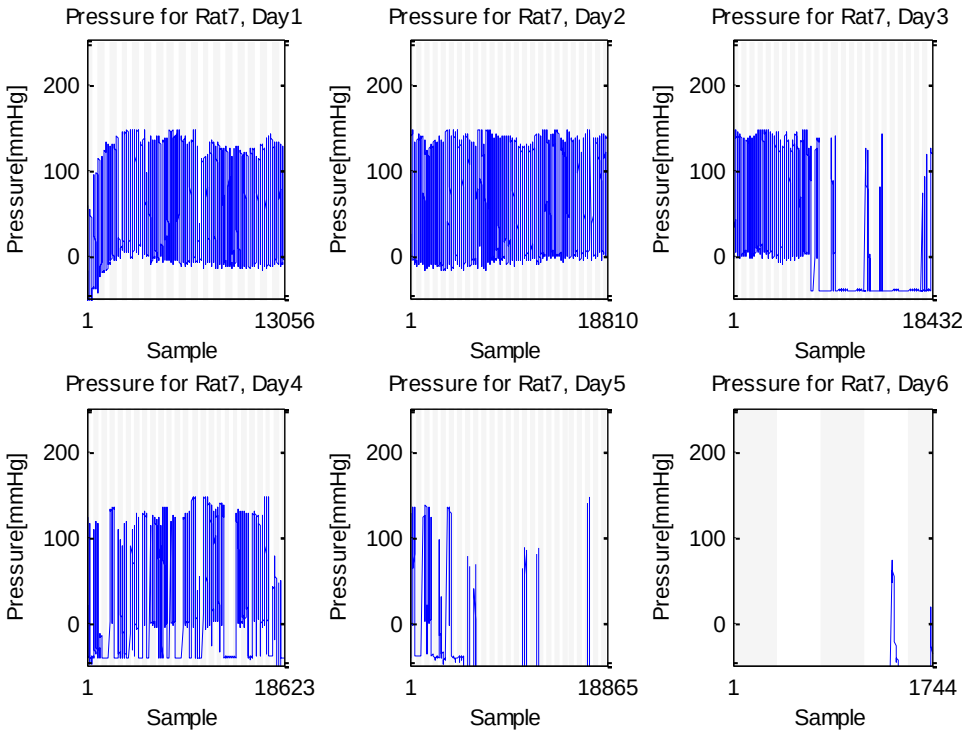

Figure 66: Pressure Data, Rat 7

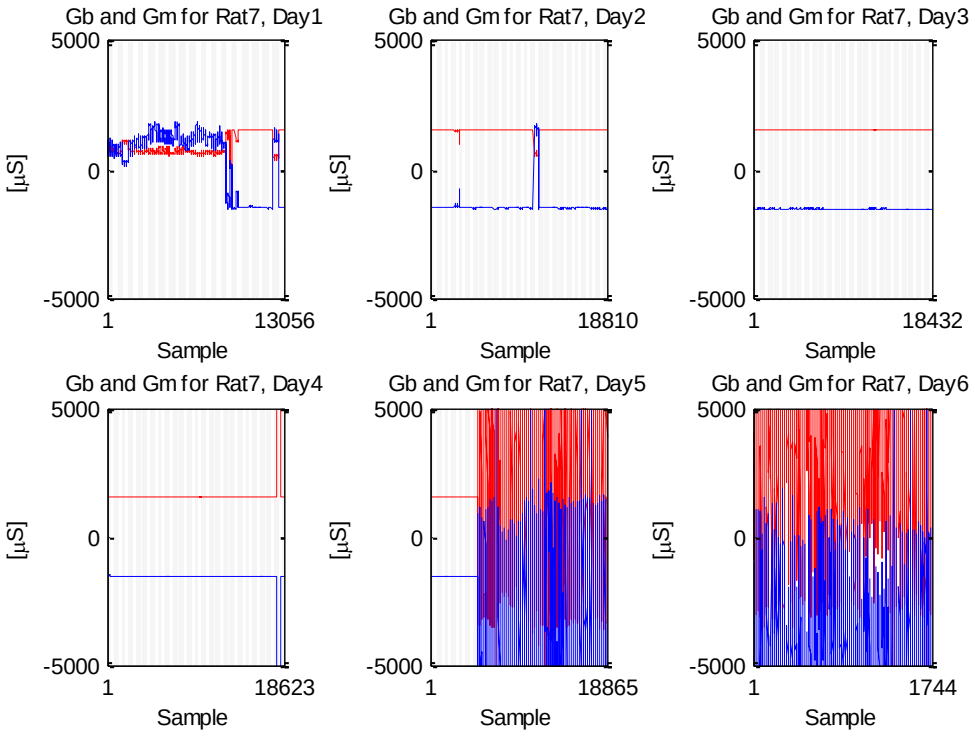

Figure 67: Volume Data, Rat 7

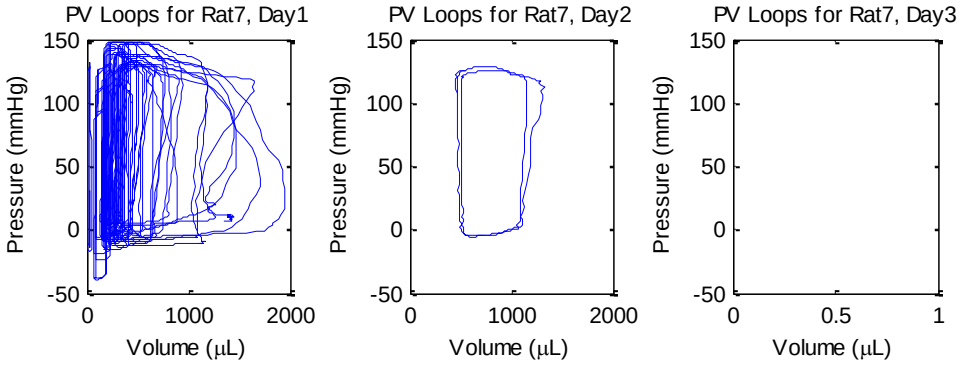

Figure 68: PV Data, Rat 7

References

[1] K. R. Chien, "Molecular advances in cardiovascular biology," *Science ,* vol. 260, pp. 916-917, 1993.

[2] M. Krenz, "Conductance, admittance, and hypertonic saline: should we take ventricular volume measurements with a grain of salt?," *Journal of Applied Physiology,* vol. 107, pp. 1683-1684, 2009.

[3] J. J. Baan, T. T. Jong and P. L. Kerkhof, "Continuous stroke volume and cardiac output from intraventricular dimensions obtained with impedance catheter," *Cardiovasc. Res.,* vol. 15, pp. 328-334, 1981.

[4] D. Burkhoff, E. Van Der Velde, D. Kass, J. Baan, W. L. Maughan and K. Sagawa, "Accuracy of volume measurement by conductance catheter in isolated, ejecting canine hearts," *Circulation,* vol. 72, no. 2, pp. 440-447, 1985.

[5] D. Georgakopoulos and D. Kass, "Estimation of parallel conductance by dual-frequency conductance catheter in mice," *Am J Physiol Heart Circ Physiol,* vol. 279, pp. 443-450, 2000.

[6] C.-L. Wei, J. W. Valvano, M. D. Feldman and J. A. Pearce, "Nonlinear conductance volume relationship for murine conductance catheter measurement system," *IEEE Trans. on Biomedical Engineering,* vol. 52, no. 10, pp. 1654-1661, 2005.

[7] A. T. Kottam, J. Porterfield, K. Raghavan, D. Fernandez, M. D. Feldman, J. W. Valvano and J. A. Pearce, "Real time pressure-volume loops in mice using complex admittance: measurement and implications," *Proceedings of the 28th IEEE EMBS Annual International Conference,* pp. 4336-4339, 2006.

[8] J. E. Porterfield, A. T. Kottam, K. Raghavan, D. Escobedo, J. T. Jenkins, E. R. Larson, R. J. Trevino, J. W. Valvano, J. A. Pearce and M. D. Feldman, "Dynamic correction for parallel conductance, Gp, and gain factor, alpha, in invasive murine left ventricular volume measurements," *J. Appl. Physiol.,* vol. 107, pp. 1693-1703, 2009.

[9] K. Uemura, T. Kawada, M. Sugimachi, C. Zheng, K. Kashihara, T. Sato and K. Sunagawa, "A self-calibrating telemetry system for measurement of ventricular pressure-volume relations in conscious, freely-moving rats," *Am. J. Physiol. Heart Circ. Physiol.,* vol. 287, pp. H2906-H2913, 2004.

[10] K. Raghavan, M. D. Feldman, J. E. Porterfield, E. R. Larson, J. T. Jenkins, D. Escobedo, J. A. Pearce and J. W. Valvano, "A bio-telemetric device for measurement of left ventricular pressure-volume loops using the admittance technique in conscious, ambulatory rats," *Physiol. Meas.,* vol. 32, pp. 701-715, 2011.

[11] L. Shuhatovitch, "Design and implementation of a low-power implantable cardiac monitoring device," University of Texas, Austin, 2010.

[12] J. Webster, Medical Instrumentation: Application and Design, 4th ed., Hoboken, NJ: Wiley, 2010.

[13] A. Kottam, "Determiniation of Parasitic Circuit Elements in Cardiac Conducatance Catheters," University of Texas, Austin, 2003.

[14] E. Larson, "Admittance Measurement for the Assesment of Cardiac Hemodynamics in Clinical and Research Applications," University of Texas, Austin, 2012.

[15] W. Franks, I. Schenker, P. Schmutz and A. Hierlemann, "Impedance Characterization and Modeling of Electrodes for Biomedical Applications," *IEEE Transactions on Biomedical Engineering,* vol. 52, no. 7, pp. 1295-1302, 2005.

[16] T.-J. Kao, G. J. Saulnier, D. Isaacson, T. L. Szabo and J. C. Newell, "A versatile high permittivity phantom for EIT," *IEEE Transactions on Biomedical Engineering,* vol. 55, no. 11, pp. 2601-2607, 2008.

[17] "Weather Underground," [Online]. Available: http://www.wunderground.[16]com/history/airport/KSAT/2012/7/1/DailyHistory.html. [Accessed 1 November 2012].